2014-07-01

Development of a Complex Synthetic Larynx Model and Characterization of the Supraglottal Jet

Jayrin Ella Seegmiller
Brigham Young University - Provo

Development of a Complex Synthetic Larynx Model and Characterization of the Supraglottal Jet

Jayrin Seegmiller

A thesis submitted to the faculty of
Brigham Young University
in partial fulfillment of the requirements for the degree of

Master of Science

Scott L. Thomson, Chair
R. Daniel Maynes
Tadd T. Truscott

Department of Mechanical Engineering

Brigham Young University

June 2014

ABSTRACT

Development of a Complex Synthetic Larynx Model and
Characterization of the Supraglottal Jet

Jayrin Seegmiller
Department of Mechanical Engineering, BYU
Master of Science

Voice is an important tool for communication. Consequently, voice disorders tend to severely diminish quality of life. Voice research seeks to understand the physics that govern voice production to improve treatment of voice disorders. This thesis develops a method for creating complex synthetic laryngeal models and obtaining flow data within these complex models. The method uses Computed Tomography (CT) scan data to create silicone models of the larynx. Index of refraction matching allows flow field data to be collected within a synthetic complex larynx, which had previously been impossible. A short proof-of-concept of the method is set forth. Details on the development of a mechanically-driven synthetic model are presented. Particle image velocimetry was used to collect flow field data in a complex and a simplified supraglottal model to study the effect of complex geometry on the supraglottal jet. Axis switching and starting and closing vortices were observed. The thesis results are anticipated to aid in better understanding flow structures present during voice production.

Keywords: voice production, larynx, mechanically-driven vocal folds, supraglottal jet

ACKNOWLEDGEMENTS

First and Foremost, I would like to express gratitude to my Heavenly Father for His guidance and support throughout my life. I know that He has been very mindful of me and has provided me with both the challenges and blessings that I have needed. I particularly want to express gratitude for the guidance I received to pursue a masters degree at BYU with Dr. Thomson. This program has probably meant more to me than to most other students because of the opportunities I have had to grow intellectually, for the friendships that I have made, and most of all for allowing me the chance to meet and fall in love with my wonderful husband.

I would like to thank my advisor, Dr. Thomson. He has been an immense help along the way. His experience and expertise have been invaluable to my research and to my growth as a person. Most of all I am grateful for his patience and his kindness when I needed it most, and for his continued encouragement when research wasn't going very smoothly.

To my committee members, Dr. Tadd Truscott and Dr. Daniel Maynes, I express appreciation for their support and for reading through this thesis and providing valuable suggestions for improvement.

Special thanks go to Kevin Cole for his help with LabVIEW programming, and for his expertise in almost every other piece of equipment in the department. His patience and help have been greatly appreciated. I also want to thank Ken Forester for his machining expertise.

I express gratitude to Simeon Smith for his work on developing a LabVIEW motor control program, as well as on other parts of my project. I would also like to recognize the other members of the Voice Research Group for their friendship and support.

I give my sincere gratitude to the BYU Mechanical Engineering Department and the National Institute on Deafness and Other Communication Disorders (NIDCD) for funding support via grant R01 DC009616.

Finally I wish to express thanks to my family for their love and support. I am especially grateful to my wonderful husband, Dan, and to my son, Gabriel, for their encouragement and patience. They have provided me with the strength to continue and with joy along the way.

TABLE OF CONTENTS

LIST OF TABLES ……..……..…..… ix

LIST OF FIGURES ……..……..……..……....x

1. Introduction ……..…….. 1

1.1. Overview of Voice Production ……. 1

1.2. Voice Production Research ……... 4

1.3. Motivation ……. 6

1.4. Thesis Overview ……... 6

1.5. Thesis Outline ……... 7

1.5.1. Acquisition of Detailed Glottal Flow Measurements in Geometrically Realistic Models (Chapter 2) …… 7

1.5.2. Driven Vocal Fold Model Design (Chapter 3) …….. 7

1.5.3. Characterization of the Supraglottal Jet in a Complex Larynx Model (Chapter 4) ……. 8

2. Acquisition of Detailed Glottal Flow Measurements in Geometrically Realistic Models ……..……..…….. 9

2.1. Abstract …… 9

2.2. Introduction …… 10

2.3. Methods …….. 11

2.3.1. Silicone Model ……. 11

2.3.2. Index Matching …… 12

2.3.3. Experimental Setup …….. 12

2.4. Results and Discussion ……... 14

2.5. Conclusions …… 15

3. Driven Vocal Folds Model Design ……..…… 18

3.1. Overview of Experimental Setup …… 18

3.2. Subglottal and Supraglottal Silicone Sections …… 19

3.2.1. Conversion of Larynx Geometry into CAD Model ……. 19

3.2.2. Subglottal Geometry …… 22

3.2.3. Supraglottal Geometry ……. 23

3.2.4. Casting of Silicone Models …….. 25

3.3. Mechanically Driven Vocal Folds …….. 27

3.3.1. Cam Design …….. 28

3.3.2. Three-dimensional Glottal Membrane ……. 30

3.4. Flow Conditioning …….. 34

3.5. Index Matching ……... 36

4. Characterization of the Supraglottal Jet in a Complex Larynx Model …….. 38

4.1. Overview …… 38

4.2. Introduction …… 38

4.3. Methods …….. 42

4.3.1. Silicone Models ……... 42

4.3.2. Experimental Setup …….. 43

4.4. Results and Discussion ……... 48

4.4.1. Pressure Comparisons …….. 48

4.4.2. PIV Data ……... 49

4.4.2.1. Cylindrical Supraglottal Data …….. 49

4.4.2.2. Realistic Supraglottal Data (matched flow rate) …….. 55

4.4.2.3. Realistic Supraglottal Data (matched pressure) ……... 56

4.4.2.4. Comparisons for All Three Cases …… 57

4.4.2.5. Vorticity ……... 61

4.4.2.6. Axis Switching ……. 69

4.5. Uncertainty Analysis of PIV Measurements …….. 71

4.6. Conclusions ……. 73

5. Conclusions ……..…….. 76

5.1. Acquisition of Detailed Glottal Flow Measurements in Geometrically Realistic Models……. 76

5.1.1. Conclusions …….. 76

5.1.2. Future Work ……. 77

5.2. Driven Vocal Fold Model Design ……... 77

5.2.1. Conclusions …….. 77

5.2.2. Future Work ……. 77

5.3. Characterization of the Supraglottal Jet in a Complex Larynx Model ……... 78

5.3.1. Conclusions …….. 78

5.3.2. Future Work ……. 78

REFERENCES ……..…….…… 80

Appendix A. PIV Uncertainty – Matlab Code ……..…….…… 84

A.1 EquipmentUncertainty.m ……... 84

A.2 InertialUncertainty.m ……. 85

A.3 ProcessUncertainty.m …… 86

A.4 TotalUncertainty.m …… 87

Appendix B. PIV Uncertainty Analysis ……..…… 89

B.1 Equipment Uncertainty …..……... 89

B.2 Inertial Uncertainty ...……. 90

B.3 Process Uncertainty ….…...…… 91

B.4 Total Uncertainty ……...……. 92

Appendix C. Pressure Uncertainty ……..…… 94

LIST OF TABLES

Table 4-1. Flow rate and pressure for each experimental case 44

Table 4-2. Comparison of parameters for the model used in this study, the corresponding values for a life-sized model in air, and the average parameters of human phonation … 46

Table 4-3. Maximum total uncertainty (w_{total}) and percent uncertainty of local velocity values for each case 73

Table B-1. Summary of equipment uncertainty parameters 90

Table B-2. Length of calibration scale parameters 90

Table B-3. Maximum total uncertainty ($w_{total)}$ and percent uncertainty of local velocity values for each case 92

Table C-1. Pressure transducer calibration data 95

LIST OF FIGURES

Figure 1-1. Geometry of the human larynx in sagittal (left) and coronal (right) planes (from Gray's *Anatomy of the Human Larynx*, images public domain, www.bartleby.com). Adapted from Smith (2011)…… 2

Figure 1-2. Illustration of the glottal profile during phonation. The glottal shape is convergent during the opening phase (top), and divergent during the beginning of the closing phase (bottom). Vocal fold profiles were generated using excised human larynx profile data from Döllinger and Berry (2006)..…….……..……..…….…… 3

Figure 2-1. Photographs depicting the effects of index of refraction matching between the fluid and the model. The silicone model with a larynx airway-shaped cavity is placed in front of a grid. Shown are views of the cavity filled with (a) air, (b) water, and (c) 55/45 glycerol-water mixture……..... 13

Figure 2-2. (a) Schematic of the experimental setup. (b) (Left) and (Middle): Arrows denoting approximate locations of sagittal and coronal image planes, respectively. Distance between adjacent planes was approximately 5 mm. (Right): Raw PIV image……. 14

Figure 2-3. Average velocity distributions in (a) five coronal planes, and (b) five sagittal planes. (c) and (d) Velocity vectors in laryngeal ventricles in two coronal planes (the plane on the right was located approximately 5 mm dorsally to the plane on the left). Counter-clockwise (CCW) and clockwise (CW) vortices are seen in the left and right ventricles, respectively, in both planes. An additional counter-rotating vortex is present in the lateral extent of the right ventricle in (d)……..... 16

Figure 3-1. Schematic of the closed-loop experimental setup. Fluid was driven by a pump, through a flow meter, a flow conditioning tank, and up through the synthetic larynx…. 19

Figure 3-2. STL to solid geometry conversion process. The process is shown here for one laryngeal section in order to be seen in greater detail. Reference planes were made in the sagittal, coronal, and transverse planes (left image). Splines were created at the intersections of the planes and the STL surface (middle). The splines were lofted into solid sections, and the sections were sewn together into a solid geometry (right)… 20

Figure 3-3. (a) Geometry of the human larynx in sagittal (left image) and coronal (right image) planes (adapted from Gray's *Anatomy of the Human Larynx*, images public domain, www.bartleby.com). (b) Airway geometry of original STL file. Views are from the sagittal (left image) and coronal (right image) planes. The dimensions are for the 4x model……..... 21

Figure 3-4. (a) Original airway geometry, coronal view. (b) Original airway geometry, sagittal view. (c) Modified geometry, coronal view. (d) Modified geometry, sagittal view……...……... 22

Figure 3-5. Coronal and sagittal views of (a) normal, and (b) 90% stenosis models……... 23

Figure 3-6. Geometry of the human larynx, pharynx, and oral cavity in the sagittal plane (adapted from Gray's *Anatomy of the Human Larynx*, images public domain, www.bartleby.com) ……..……..... 24

Figure 3-7. Original geometry (left) including the pharynx and oral cavity. Pharynx geometry (right) used for this study…….. 24

Figure 3-8. Coronal and sagittal views of the supraglottal section, consisting of the supraglottis, loft connection, and pharynx……..... 25

Figure 3-9. Images of the silicone model casting process, as shown for the supraglottis. (Left) The rapid prototype was positioned in an acrylic box, and a metal rod was inserted 1 cm above the inferior surface for later pressure tap insertion. (Middle) Silicone was poured around the prototype and allowed to cure. The acrylic box was then removed. (Right) The prototype was washed out, leaving a silicone model of the airway……..……..... 26

Figure 3-10. Subglottal 0% stenosis, supraglottal, and subglottal 90% stenosis silicone models……... 27

Figure 3-11. Cylindrical supraglottis before (left) and after (right) silicone casting…… 28

Figure 3-12. Image stills of the mechanically-driven vocal folds during vibration. Flow is out of the page. (a)-(e) the glottis is opening. (f)-(i) the glottis is closing. In (a) and (i) the glottis is fully closed. In (e) the glottis is fully open. Note the white section seen in the open glottis is the entrance to the subglottal opening. Two open phases and nine closed phases are not shown in this image……. 29

Figure 3-13. Cam geometry and dimensions. The central cross section of the glottal opening was semi-elliptical in the middle and circular on the ends. The glottal opening was offset from center…….. 31

Figure 3-14. Coronal and sagittal views of the (a) original glottal geometry, and (b) modified glottal geometry…… 32

Figure 3-15. (a) Molds for creating glottal membrane. (b) Fully assembled mold. (c) View of the superior surface of the membrane. (d) Coronal view of the membrane. (e) Superior view of fully assembled glottal section, including glass support plates, acrylic box, and gears. In this image the membranes were coated with several layers of a stiffer silicone seen in blue, not included in the final model……. 33

Figure 3-16. Final assembly of the glottal section, including glass support plates, acrylic box, cams, and gears. Note that the sides of the acrylic box were removed for these images for internal viewing. Also note in this model the membranes were coated with several layers of a stiffer silicone (Smooth-Sil® 935, Smooth-On, Inc.), seen in blue, that were not included in the final model……. 33

Figure 3-17. Internal view of the flow conditioning tank. Flow enters through dispersion tubes, rises through the plate-gravel-mesh system, and enters the subglottis through the flow conditioning contraction……. 35

Figure 3-18. Image of flow dispersion pipes and acrylic support plate……... 35

Figure 3-19. Flow conditioning contraction upstream of the subglottis……... 36

Figure 3-20. Grid placed behind the 90% stenotic section with the section filled with (a) air, (b) water, and (c) 52%-48% glycerol-water solution. Note the absence of optical distortions in (c)……..... 36

Figure 3-21. Comparison of glycerol-water mixtures. The dotted line highlights the shape of the airway. The cavity is to the right of the dotted line. The optimal fluid mixture that matches the index of refraction of the silicone is 52% glycerol, 48% water. Distortions of the grid between the silicone (left of the dotted line) and the fluid filled cavity (right) can be detected for all other mixtures……...……. 37

Figure 4-1. Geometry of the human larynx in sagittal (left) and coronal (right) planes (same as Figure 1-1, from Gray's *Anatomy of the Human Larynx*, images public domain, www.bartleby.com). Adapted from Smith (2011)……... 39

Figure 4-2. Subglottal (left), realistic supraglottal (center), and cylindrical supraglottal (right) silicone models…….. 43

Figure 4-3. Schematic of the closed-loop experimental setup. Fluid was driven by a pump, through a flow meter, a flow conditioning tank, and up through the synthetic larynx (same as Figure 3-1)…….. 43

Figure 4-4. (Left) and (Middle): Arrows denoting approximate locations of sagittal and coronal image planes, respectively (not to scale). Distance between adjacent planes was approximately 6 mm in the coronal direction, and 3 mm in the sagittal direction. (Right): Raw PIV image, corresponding to plane 3 in the coronal direction……... 47

Figure 4-5. Glottal area (top) and average transglottal pressure (bottom) waveforms vs. phase……. 50

Figure 4-6. PIV data for cylindrical geometry in the (left) coronal planes, and (right) sagittal planes. Only certain phases are shown…… 51

Figure 4-7. PIV data for realistic geometry - matched flow rate case in the (left) coronal and (right) sagittal planes……. 52

Figure 4-8. PIV data for realistic geometry - matched pressure case in the (left) coronal and (right) sagittal planes……. 53

Figure 4-9. Comparison of PIV data for the midplane of each case in the coronal (left three PIV images) and sagittal (right three PIV images) planes…… 54

Figure 4-10. Comparison of the right and left profiles of the supraglottis in the three sagittal planes…… 56

Figure 4-11. Matched flow rate case, coronal view, plane 1. (a) Fluid motion was seen at 36°, before the supraglottal jet emerged in this plane (54°). (b) 18° and 36° shown with a smaller velocity threshold to highlight the change in velocity between the two phases…….…….... 57

Figure 4-12. Comparison of the velocity vector fields for 90° of the midplane jet for all three experimental cases…… 60

Figure 4-13. Coronal view (plane 2) of vortical structures that developed during the opening phases of the glottis. The velocity contours are shown here. Velocity contour scale corresponds to the color scale given in Figure 4-12 ……... 63

Figure 4-14. Coronal view (plane 2) of vorticity plots during the late opening phases of the glottis…….……... 64

Figure 4-15. Sagittal view (plane 2) of vortical structures that developed during the opening phases of the glottis. Velocity contour scale corresponds to the color scale given in Figure 4-12 ……... 65

Figure 4-16. Coronal view (plane 2) of vorticity plots during the late opening phases of the glottis…… 65

Figure 4-17. (Left) Coronal view of vortices formed during the closing phases of the glottis for the matched flow rate case. (Right) Enlargement of the boxed region in the images on the left. Velocity contour scale corresponds to the color scale given in Figure 4-12……..... 66

Figure 4-18. (Left) Sagittal view of vortices formed during the closing phases of the glottis for the matched flow rate case. (Right) Enlargement of the boxed region in the images on the left. Velocity contour scale corresponds to the color scale given in Figure 4-12…… 67

Figure 4-19. Coronal view of Kelvin-Helmholtz vortices formed during the closing phases of the glottis for the matched flow rate and cylindrical cases……... 68

Figure 4-20. Coronal view of vortices convected downstream during the closing phases of the glottis for the matched flow rate and cylindrical cases……... 69

Figure 4-21. Comparison of midplane jet width for cylindrical, matched flow rate, and matched pressure cases for 90°. An outline of the sagittal view is shown in grey; the coronal view is shown in white. a and b denote locations of jet width comparison, with the measurements given below outlines for each case. Velocity contour scale corresponds to the color scale given in Figure 4-12 ……..…….. 70

Figure B-1. Velocity and uncertainty data for 54° of the mid-sagittal plane for all three cases…….. 93

Figure C-1. Percent error of the pressure calibration data…… 95

Figure C-2. Total instrument uncertainty for the pressure calibration range……..... 97

Figure C-3. Comparison of original and calibrated pressure data for the cylindrical case…….... 98

Figure C-4. Comparison of original and calibrated pressure data for the matched flow rate case……..... 99

Figure C-5. Comparison of original and calibrated pressure data for the matched pressure case…….. 100

1 INTRODUCTION

The human voice is an important tool for communication and is often the foundation for both professional and personal interactions. Because the voice is such an important part of human communication, voice disorders severely diminish quality of life. The National Institute on Deafness and Other Communication Disorders (NIDCD) reports that approximately 7.5 million people are affected by voice disorders in the United States alone (NIDCD, 2010).

Voice research seeks to understand the physics that govern both normal and pathological voice production. Through the application of principles of physics, engineering, and medicine, an improved understanding of voice production can lead to advances in prevention, diagnosis, and treatment of voice disorders. The purpose of this thesis research is to contribute to an enhanced understanding of the voice by (1) developing synthetic models of the larynx, and (2) using the models to explore flow field structures within the larynx. A brief overview of voice production, voice production research, and the motivation for the research described in this thesis are given in this chapter. Additional background and literature reviews are given in each respective chapter.

1.1 Overview of Voice Production

The larynx is the area of the body where sound for audible voice is produced (see Figure 1-1). The three main regions of the larynx are the subglottis, the glottis, and the supraglottis.

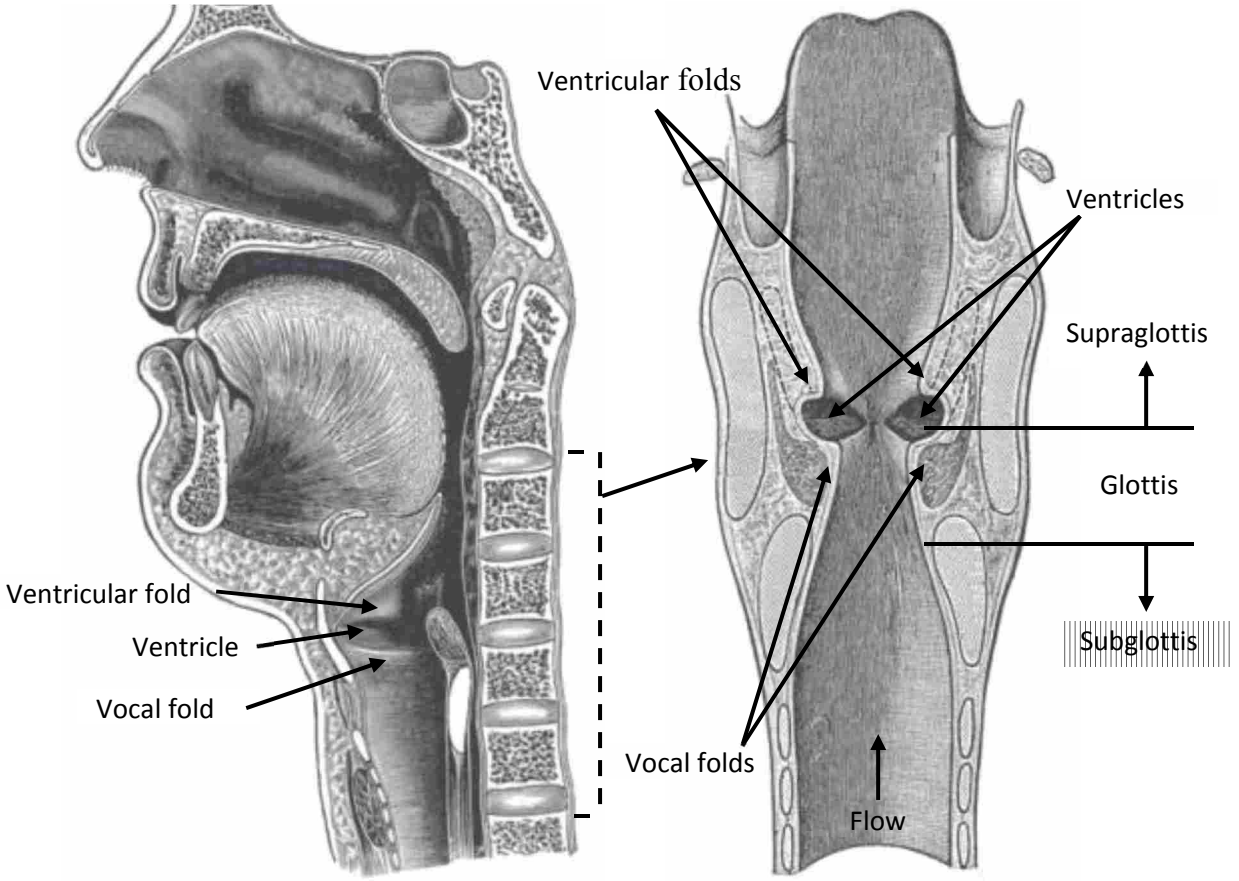

Figure 1-1. Geometry of the human larynx in sagittal (left) and coronal (right) planes (from Gray's *Anatomy of the Human Larynx*, images public domain, www.bartleby.com). Adapted from Smith (2011).

The subglottis extends from the tracheal region to the bottom of the vocal folds. The vocal folds are a pair of pliable tissue folds within the larynx that vibrate to produce audible sound. The glottis is the space between the vocal folds. The supraglottis extends from the top of the vocal folds to the epiglottis. The supraglottis includes the ventricular folds (also known as the false folds) and the ventricles (the lateral spaces between the vocal folds and the ventricular folds).

Voicing is produced by flow-induced vibration of the vocal folds. Muscles in the larynx bring the vocal folds together medially. Air flow from the lungs is forced through the nearly

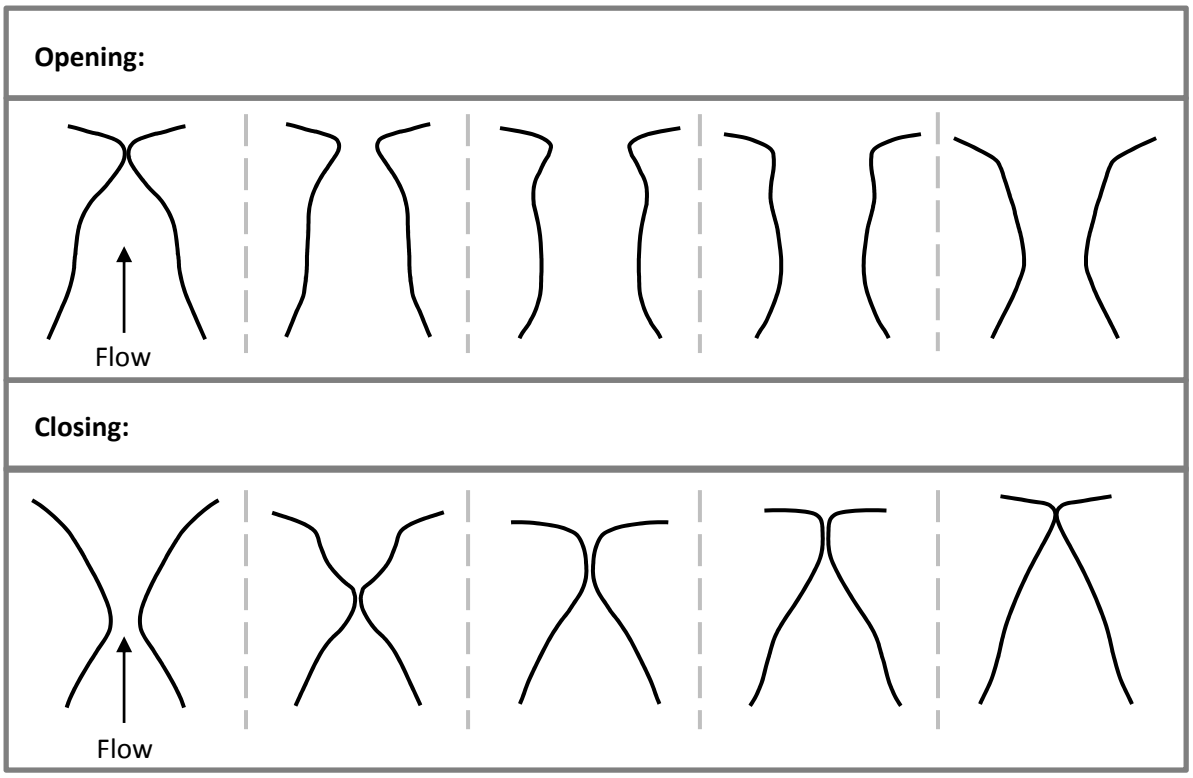

Figure 1-2. Illustration of the glottal profile during phonation. The glottal shape is convergent during the opening phase (top), and divergent during the beginning of the closing phase (bottom). Vocal fold profiles were generated using excised human larynx profile data from Döllinger and Berry (2006).

closed glottis and initiates vocal fold self-oscillation. The vibrations cause pressure fluctuations in the supraglottal jet. The pressure fluctuation is a sound source that is filtered by the vocal tract for audible voicing. As the vocal folds vibrate they create a convergent-divergent waveform (see Figure 1-2). As the vocal folds are forced open they create a convergent glottal shape. As they close the glottal shape is divergent.

1.2 Voice Production Research

Research performed within the past few decades has significantly enhanced our understanding of vocal fold dynamics and airway flow dynamics during voice production. Of particular relevance to this study are the various types of models that have been used to characterize laryngeal airflow. These models include excised larynges, synthetic models, and computational models, examples of which are provided here.

Excised larynges have realistic geometries and provide realistic vocal fold motion, and thus yield reliable airflow information. However, since they are typically used without a vocal tract, excised larynx studies do not yield complete information about supraglottal flow structures. Khosla et al. (2007) used excised canine larynges with no supraglottal geometry (free jet) to study glottal and supraglottal vortices produced during different phases of voice production. They suggested that these vortical structures significantly contribute to voice quality. Oren et al. (2009) later used excised canine larynges with a free jet to study the effect of subglottal shape on the reduction of turbulence intensity in the supraglottis.

Synthetic models offer the potential for acquiring glottal and subglottal flow data because of improved reliability, control, and optical access. They are also much easier to work with than excised larynges and offer more potential for parametric studies. Vocal folds in these models are either static (Hofmans et al., 2003; Alipour et al., 2006; Grisel et al., 2010), self-oscillating (Drechsel and Thomson, 2008; Becker, 2009), or mechanically-driven (Triep et al., 2005; Erath and Plesniak, 2010; Kirmse et al., 2010; Triep and Brücker, 2010). These studies have used synthetic models to investigate supraglottal and glottal velocity profiles using particle image velocimetry (PIV) and other flow visualization methods. Some of these studies (Alipour et al.,

2006; Triep et al., 2005; Kirmse et al., 2010) also investigated subglottal velocity profiles, but using highly simplified subglottal and supraglottal geometry.

Computational models have also been used to deepen our understanding of voice production. Computational models are very useful for studying laryngeal flow structures because they are not limited by optical access. However, accurate simulations are complex, computationally expensive, and require thorough validation using experimental data. Mihaescu et al. (2010) simulated flow through a static vocal fold model to study intraglottal velocity and pressure fields. Scherer et al. (2001) used numerical methods to measure intraglottal pressure profiles in a static glottis. Suh and Frankel (2008) created a static computational model to compare turbulence models for predicting flow through a rigid glottis.

In a recent study by Xue et al. (2014) a computational model of a subject-specific human larynx was created from computed tomography (CT) scan data to study the effects of realistic geometry on vocal fold vibration and glottal flow. The investigation observed anterior-posterior asymmetries in vocal fold vibration and glottal flow, and a lack of strong jet deflection that had been observed in previous studies. This study was the first detailed study to investigate glottal flow in a realistic supraglottis. The investigation observed anterior-posterior asymmetries in vocal fold vibration and glottal flow, and a lack of strong jet deflection that had been observed in previous studies. Results of this computational study need to be validated on a physical model, and further exploration is needed.

The above mentioned studies have aided our understanding of laryngeal flow and of the physics of voice production. However, most were performed in vocal fold models either containing no supraglottis (free jet) or with uniform vocal tracts. The study conducted by Xue et al. (2014) was the first detailed study to investigate glottal flow in a realistic supraglottis. It is

important to determine if laryngeal flow structures such as axis switching, vortex shedding, and jet skewing, that have been observed in models with simplified supraglottal geometries are also observed in realistic geometries, and to validate the results of Xue et al. (2014) on a physical model.

1.3 Motivation

Through voice research, many flow structures have been identified that occur in simplified or uniform supraglottal geometries; however, there is a need for detailed information on flow structures in realistic subglottal and supraglottal geometries. Lack of optical and/or physical access has limited studies to less complex supraglottal, and often subglottal, geometries. It is hypothesized that flow structures observed in uniform vocal tracts may also be present during actual human voice production. Investigations in more physiologically realistic models are needed in order to verify this hypothesis. The purpose of this thesis is to provide insight towards verifying this hypothesis by studying three-dimensional laryngeal flow within a realistic vocal tract.

1.4 Thesis Overview

A geometrically realistic laryngeal model, derived from medical imaging scans, was used to build synthetic models that incorporated realistic subglottal and supraglottal geometries. A realistic pharynx geometry (the portion of the airway downstream of the supraglottis) was included to approximate human pharyngeal anatomy and flow resistance. A simplified, circular cross-section supraglottis and pharynx were also used to study the influence on geometry and geometric assumptions on the nature of supraglottic flow structure dynamics in simplified vs.

realistic airway geometries. In one of the studies, dynamic (motor-driven) vocal fold models were used to simulate vocal fold motion. Reynolds and Strouhal numbers were matched between the model and the life-sized condition, but not the Mach number; thus this study did not mimic physiological acoustic coupling.

1.5 Thesis Outline

The main body of this thesis is composed of three chapters, as follows:

1) Acquisition of detailed glottal flow measurements in geometrically realistic models
2) Driven vocal fold model design
3) Characterization of the supraglottal jet in a complex larynx model

1.5.1 Acquisition of Detailed Glottal Flow Measurements in Geometrically Realistic Models (Chapter 2)

A method for acquiring PIV data using models with realistic geometries is presented. A realistic laryngeal model with static vocal folds was created from CT scan data and used to study laryngeal flow structures. PIV data spanning subglottal, intraglottal, and supraglottal regions are shown in five coronal and five sagittal planes.

1.5.2 Driven Vocal Fold Model Design (Chapter 3)

A synthetic laryngeal model with realistic geometry was created. The geometry was extracted from CT scan data. The sub- and supraglottis sections were made of clear silicone, allowing optical access to the interior flow field. The vocal folds were mechanically-driven, with the vocal folds being represented by two counter-rotating plastic cams covered by a thin,

pliable silicone membrane. A simplified silicone supraglottis, consisting of a straight circular cross-section, was also created. The design of this setup is described in this chapter.

1.5.3 Characterization of the Supraglottal Jet in a Complex Larynx Model (Chapter 4)

PIV and transglottal pressure measurements of the supraglottal jet were conducted in the mechanically-driven setup described in Chapter 3. Comparisons were made between flow structures in uniform (cylindrical) and realistic vocal tract geometries. PIV data along three sagittal and three coronal planes are presented. Axis switching, jet deflection, starting and closing vortices, and other flow structures were observed. Comparisons are made to data collected in other uniform vocal tract models.

2 ACQUISITION OF DETAILED GLOTTAL FLOW MEASUREMENTS IN GEOMETRICALLY REALISTIC MODELS

This chapter was published in the Journal of the Acoustical Society of America and has been modified here to be consistent with the stylistic requirements of this thesis. It is reproduced with permission from Farley, J. and Thomson, S. L., 2011, "Acquisition of detailed laryngeal flow measurements in geometrically realistic models," *Journal of the Acoustical Society of America*, 103, EL82-EL86. Copyright 2011, AIP Publishing LLC. Some minor context changes have been made. It represents a short proof-of-concept study that provides the conceptual basis for the methods and scientific investigation described in Chapters 3 and 4 of this thesis. More details on the model fabrication process and index of refraction matching are given in Chapter 3.

2.1 Abstract

Characterization of laryngeal flow velocity fields is important to understanding vocal fold vibration and voice production. One particularly useful method for acquiring flow field data is particle image velocimetry (PIV). However, because using PIV with models that have curved surfaces is problematic due to optical distortion, experimental investigations of laryngeal airflow are typically performed using models with simplified geometries. In this paper a method for acquiring PIV data using models with realistic geometries is presented. Sample subglottal,

intraglottal, and supraglottal PIV data are shown. Capabilities and limitations are discussed, and suggestions for future implementation are provided.

2.2 Introduction

Because airflow through the larynx affects vocal fold vibration and speech quality, it is important to be able to accurately characterize laryngeal flow structures. Many experimental studies have focused on supraglottal aerodynamics; however, optical access has limited the investigation of intraglottal and subglottal aerodynamics. Further, most studies on supraglottal aerodynamics have used simplified supraglottal geometries (Triep and Brücker, 2008) or have focused on a free jet without supraglottal structures (Khosla et al., 2007). Subglottal, glottal, and supraglottal airflow data obtained using models with realistic geometries is necessary to accurately characterize laryngeal airflow and ascertain its effects on voice production.

Several types of models have been used to study laryngeal airflow. These include static (Alipour and Scherer, 2002), driven (Triep and Brücker, 2008), and self-oscillating (Drechsel and Thomson, 2008) vocal fold models. In such studies, subglottal and supraglottal geometries are typically approximated using simplified, constant area cross-sections. Excised larynx models (Khosla et al., 2007; Alipour and Scherer, 2006; Oren et al., 2009) incorporate realistic subglottal and glottal geometries, but are limited in terms of parameterization, can only be used for a short period of time, and supraglottal geometry, if included, is typically simplified. Finally, computational models provide another method for studying laryngeal flow (Mihaescu et al., 2010; Zheng et al., 2009). Because computational models are not limited by optical access, they can yield detailed flow data throughout the larynx. However, accurate simulations are complex, computationally expensive, and require thorough validation using experimental data.

Particle image velocimetry (PIV) is a common method of choice for acquiring spatially-resolved flow field data. However, using PIV with models that have curved surfaces is problematic due to optical distortion caused by light refraction at the model-fluid interface. In this paper a method for acquiring detailed flow field data using PIV with synthetic models that have realistic geometries is presented. The refraction difficulty is overcome by creating a model with flat, smooth outer surfaces, and by matching the index of refraction of the working fluid with that of the surrounding material. This method, based on that reported by Hopkins et al. (2000) and used elsewhere (Kim et al., 2004, 2006; Doory et al., 2008) for nasal cavity airflow measurements, incorporates the use of a clear silicone model with a cavity the shape of the laryngeal airway and a glycerol-water mixture for the working fluid. Sample subglottal, intraglottal, and supraglottal PIV data sets are shown. Capabilities and limitations of the method are discussed, and suggestions for future implementation are provided.

2.3 Methods

2.3.1 Silicone Model

A model consisting of a transparent silicone rectangular prism with a larynx airway-shaped cavity was created as follows. A 3D computer model of the airway was first created via MRI image extraction. A corresponding prototype was then built on a three-dimensional printer (Z Corporation) using soluble plastic powder. The prototype was coated with several thin layers of polyvinyl acetate, and suspended in a rectangular acrylic box. Clear silicone (Sylgard 184, Dow Corning) was used to create the model. After the silicone was mixed and vacuumed to remove air bubbles it was carefully poured around the prototype, filling the acrylic box, and allowed to cure. The acrylic box was then removed and inlet and outlet holes were cut into the

silicone to allow for fluid flow. The prototype was dissolved in cold running water, leaving a silicone model with a cavity of the shape of the laryngeal airway. This process is described in more detail in Chapter 3.

2.3.2 Index Matching

A mixture of glycerol and water (55% glycerol, 45% water by volume; kinematic viscosity = 6.55×10^{-6} m^2/s) was used as the working fluid to match the index of refraction of the silicone. To find the optimal glycerol-water mixture, the silicone model was connected to a flow loop with a grid placed behind the model. An initial glycerol-water mixture with high glycerol concentration was pumped through the model and then slowly diluted until gridline distortions were minimized. Figure 2-1 shows the effect of refractive index matching when the model is filled with air, water, and the optimal glycerol-water mixture. When the model is filled with air the grid is obscured and there is no optical access to the cavity interior. With water the grid is visible, but distorted, so that PIV measurements are not possible. When filled with the 55/45 glycerol-water mixture, the index of refraction of the silicone is matched, the grid is visible with minimal distortion, and PIV can be performed on the flow in the cavity interior.

2.3.3 Experimental Setup

Figure 2-2a illustrates the experimental setup. The silicone model was connected to a flow loop. A constant pressure reservoir tank placed 0.67 m above the model supplied steady flow. Because this model was intended for demonstration purposes, the larynx inlet and outlet regions did not include flow conditioning features (e.g., smooth transitions for reduction of turbulence and secondary flow patterns). After exiting the model the fluid flowed into a lower

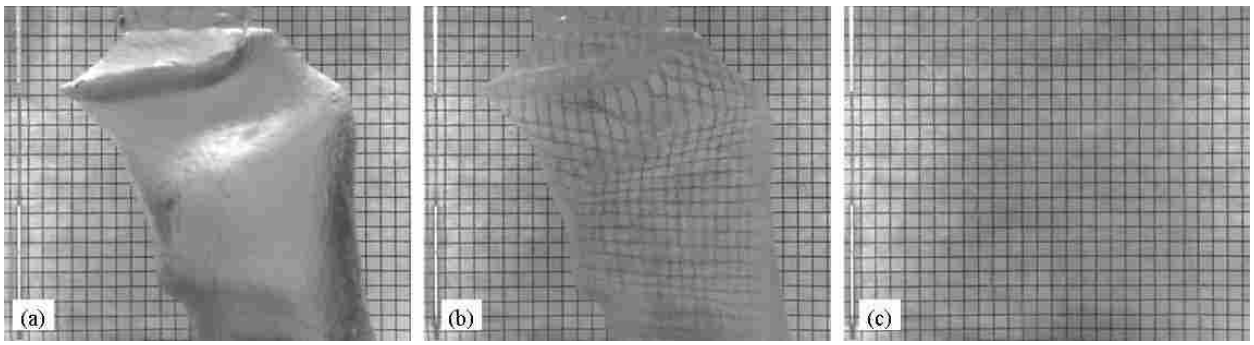

Figure 2-1. Photographs depicting the effects of index of refraction matching between the fluid and the model. The silicone model with a larynx airway-shaped cavity is placed in front of a grid. Shown are views of the cavity filled with (a) air, (b) water, and (c) 55/45 glycerol-water mixture.

reservoir where a pump (Teel®, 1P579F) returned it to the constant pressure reservoir tank. The flow was seeded with hollow glass spheres (approximately 50-70 μm diameter). PIV measurements were acquired along five sagittal and five coronal cross-sections, as shown in Figure 2-2b, using a double-pulsed laser (New Wave Laser, Solo II-15 Nd:YAG, Fremont, CA) and a synchronized camera (LaVision Imager Intense, Goettingen, Germany). At each cross-section 500 image pairs were recorded at 4.95 frames/second with a resolution of 1376×1024 pixels and a 300 μs inter-frame delay.

The velocity fields for each cross section were analyzed using an FFT-based cross-correlation algorithm to determine particle displacement and velocity vectors. Multiple passes with successively smaller interrogation regions were used, beginning with 64×64 pixel windows and a 50% overlap, and ending with 16×16 windows (also with a 50% overlap). Velocity fields at each cross section were then averaged.

(a)

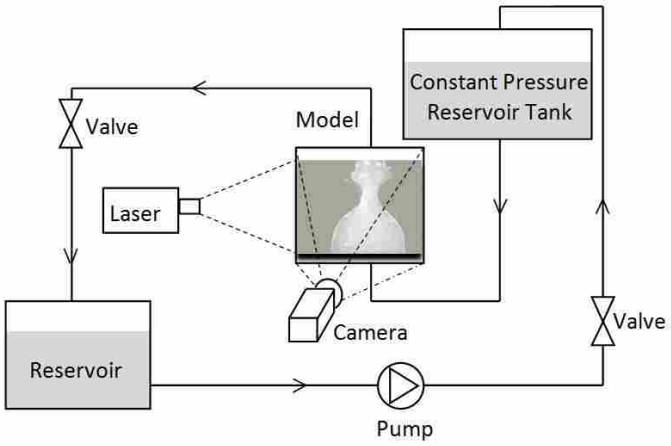

(b)

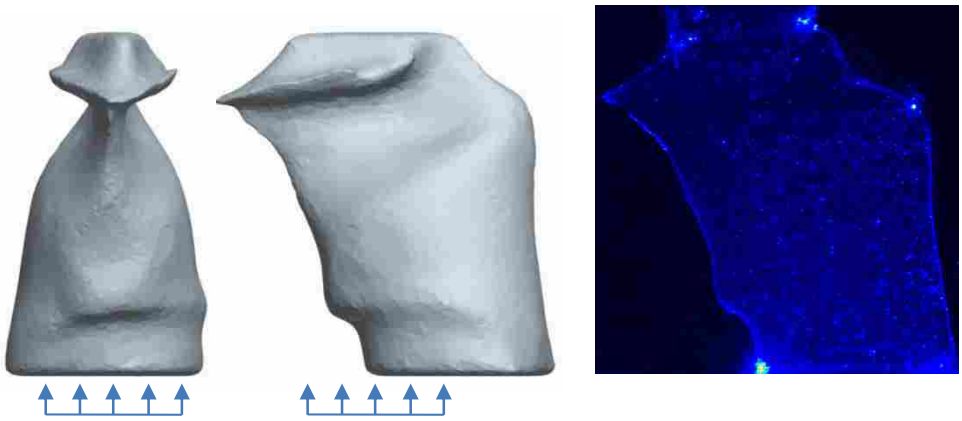

Figure 2-2. (a) Schematic of the experimental setup. (b) (Left) and (Middle): Arrows denoting approximate locations of sagittal and coronal image planes, respectively. Distance between adjacent planes was approximately 5 mm. (Right): Raw PIV image.

2.4 Results and Discussion

Figure 2-3 shows time-averaged coronal and sagittal velocity distributions. The Reynolds number based on the average inlet velocity was approximately 1570. The velocity magnitude was fairly uniform over large regions of the subglottis. Velocities quickly accelerated from around 0.4 m/s in the subglottis to around 1.2 m/s in the glottis, corresponding to approximately 0.97 m/s and 2.91 m/s, respectively, in air (the vocal folds were abducted in the MRI data set, resulting in lower glottal velocities than what is typical during phonation).

Velocity magnitudes decreased close to the subglottal walls due to wall friction and the flow inlet condition. Some vortical structures can be seen in the subglottis, inferior to the vocal folds, although again, these may be related to the inlet flow properties, and further investigation is necessary with a well-conditioned inlet to determine whether they may be present in the human case. In the present case it appears that these subglottal vortices were likely formed when the incoming jet collided with the static vocal folds, causing recirculation to occur along the subglottal walls. Exploration of velocity patterns within the laryngeal ventricles, viewed in the coronal planes, reveals recirculation zones consisting of single vortices (Figure 2-3c) and dual counter-rotating vortices (Figure 2-3d). Visual inspection of the velocity vector fields obtained from individual image pairs (before time-averaging) suggested that the vortices in this flow field were relatively stationary.

2.5 Conclusions

A method for acquiring detailed glottal flow measurements using PIV in a geometrically realistic model of the laryngeal airway has been presented and demonstrated. The method is based on the work of Hopkins et al. (2000) for nasal cavity airflow studies. This method allows for the acquisition of whole-field velocity data, even in complex model geometries. Velocity fields in sagittal and coronal planes are shown here, but PIV data acquisition in the transverse plane is also possible. This method is anticipated to find use in subsequent studies characterizing the three-dimensional velocity field, including vortical patterns and turbulence levels, found in the human larynx.

A few observations regarding limitations and future work are worth noting. First, while Reynolds number similarity is maintained, because a liquid is used as the working fluid, Mach number similarity is not. This is an inherent limitation of all liquid-based larynx model

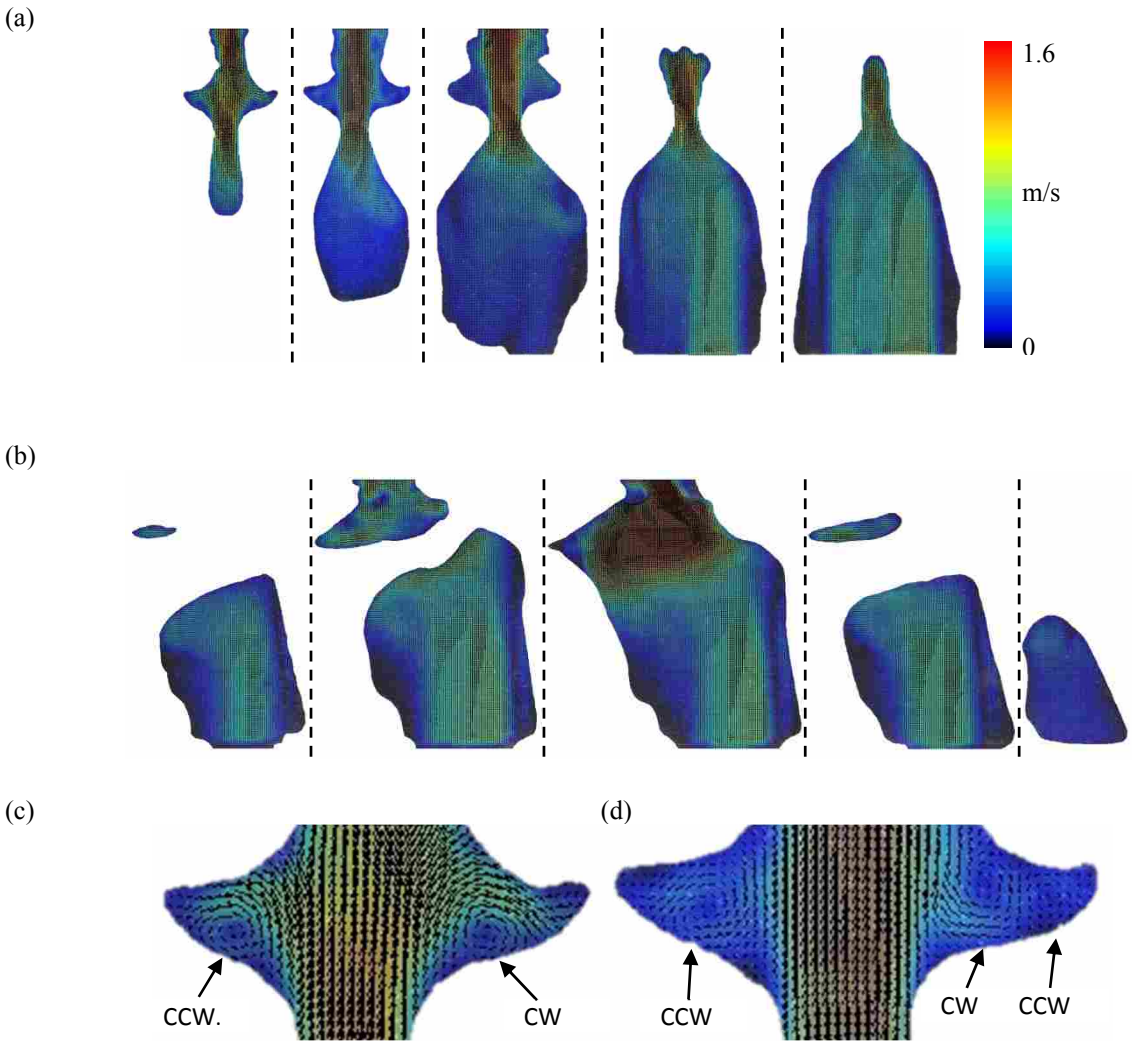

Figure 2-3. Average velocity distributions in (a) five coronal planes, and (b) five sagittal planes. (c) and (d) Velocity vectors in laryngeal ventricles in two coronal planes (the plane on the right was located approximately 5 mm dorsally to the plane on the left). Counter-clockwise (CCW) and clockwise (CW) vortices are seen in the left and right ventricles, respectively, in both planes. An additional counter-rotating vortex is present in the lateral extent of the right ventricle in (d).

experiments. The same model could possibly be used for limited acoustic analysis with air as the working fluid. Second, use of a static model does not yield information about the effect of vibrating vocal folds on the flow field. However, the development and use of a similar model with dynamically-driven vocal folds is conceivable and is the subject of Chapters 3 and 4. Third, the preliminary PIV data presented in this study are two-dimensional, but the results show that

the flow is clearly three-dimensional. This experimental technique is not restricted to two-dimensional PIV, and future studies with three-dimensional PIV using this method are possible. Fourth, future studies of this type should include conditioned inlet and outlet sections to reduce turbulence and other potential flow-loop-produced flow artifacts, ideally including the upper portion of the trachea, the pharynx, and the oral and nasal cavities to more closely model the physiological inlet and outlets. Fifth, since steady flow conditions were used in this experiment, the use of a low-speed PIV system without triggering was adequate. However, in future studies involving unsteady flow conditions or vibrating vocal folds, high-speed imaging or a combination of phase-locking and ensemble averaging would be required for temporal resolution of the flow field. Finally, the use of pressure taps (also with a matched index of refraction working fluid) in conjunction with velocity field data could be implemented.

3 DRIVEN VOCAL FOLD MODEL DESIGN

A realistic synthetic model of the vocal tract was constructed to study three-dimensional laryngeal airflow. The model was primarily made of clear silicone and scaled to four times human size. To provide optical access to the internal flow, the working fluid consisted of a glycerol-water mixture whose index of refraction matched the index of refraction of the silicone, allowing PIV data collection. The vocal folds were mechanically-driven. The design of the laryngeal model and driven vocal folds are described in this chapter.

3.1 Overview of Experimental Setup

Figure 3-1 illustrates the experimental setup developed to study three-dimensional flow features in a realistic model of the human larynx. The subglottal and supraglottal geometries were derived from computed tomography (CT) scans and the sections were made of clear silicone. The glottal section consisted of two counter-rotating, mechanically-driven cams covered by a thin silicone membrane. The rotating cams approximated the convergent-divergent motion of vibrating human vocal folds. A stepper motor (PK546PMA-R28, Oriental Motor Co. LTD) was connected to each cam through a set of gears. A pump (1P579F, Teel®) was used to drive the fluid through the closed system. Downstream of the pump the flow passed through a flow meter (FL 4604, Omega Engineering, Inc.), into a flow conditioning tank, and through the laryngeal (subglottal, glottal, and supraglottal) test sections.

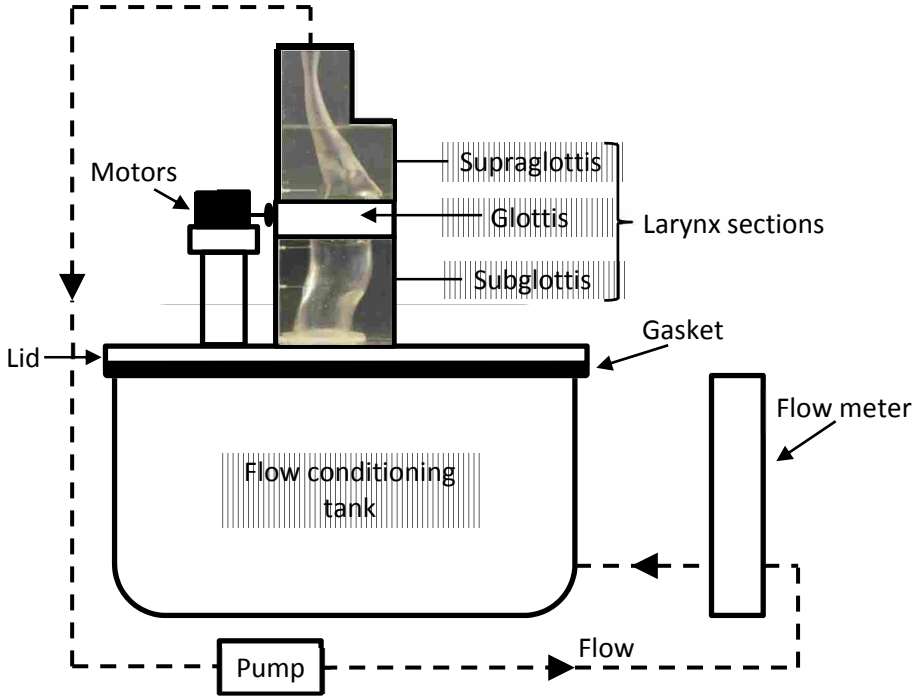

Figure 3-1. Schematic of the closed-loop experimental setup. Fluid was driven by a pump, through a flow meter, a flow conditioning tank, and upwards through the synthetic larynx.

3.2 Subglottal and Supraglottal Silicone Sections

3.2.1 Conversion of Larynx Geometry into CAD Model

The airway geometry was obtained from Dr. Hani Bakhshaee (Bakhshaee et al., 2013) at McGill University. The geometry was constructed from CT scan data, received in STL file format, and converted to a solid model in NX 8.0 (Siemens). Figure 3-2 shows the conversion process. Reference planes were created at regular intervals in the sagittal, coronal, and transverse planes. Splines were made along the interface between the reference planes and STL surfaces. The splines from each cross section were lofted into a solid section, and the sections were sewn together to make a solid geometry. The geometry was scaled to four times human size. Figure 3-3 is a comparison of the geometry of an illustrated human larynx to the original STL geometry in the sagittal and coronal planes.

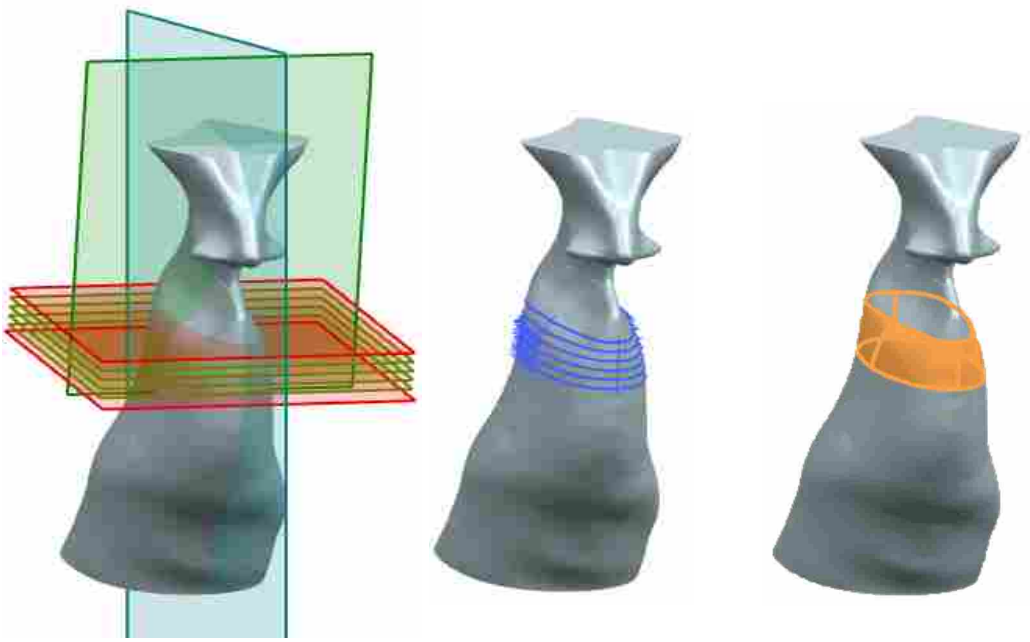

Figure 3-2. STL to solid geometry conversion process. The process is shown here for one laryngeal section in order to be seen in greater detail. Reference planes were made in the sagittal, coronal, and transverse planes (left image). Splines were created at the intersections of the planes and the STL surface (middle). The splines were lofted into solid sections, and the sections were sewn together into a solid geometry (right).

The original geometry was modified slightly so that the entrance to the subglottis conformed to a uniform circular cross section. This allowed for a smooth connection between the flow conditioning tank and the subglottis. The original and revised geometries are shown in Figure 3-4. In the original model there was a sharp bend in the trachea, as seen in Figure 3-4b, likely due to patient neck extension during imaging (see Figure 3-4c and 3-4d). As seen in Figure 3-4a the left ventricle was somewhat missing compared to the right. In the modified geometry the left ventricle was expanded to produce a greater degree of symmetry between the right and left ventricles (Figure 3-4c).

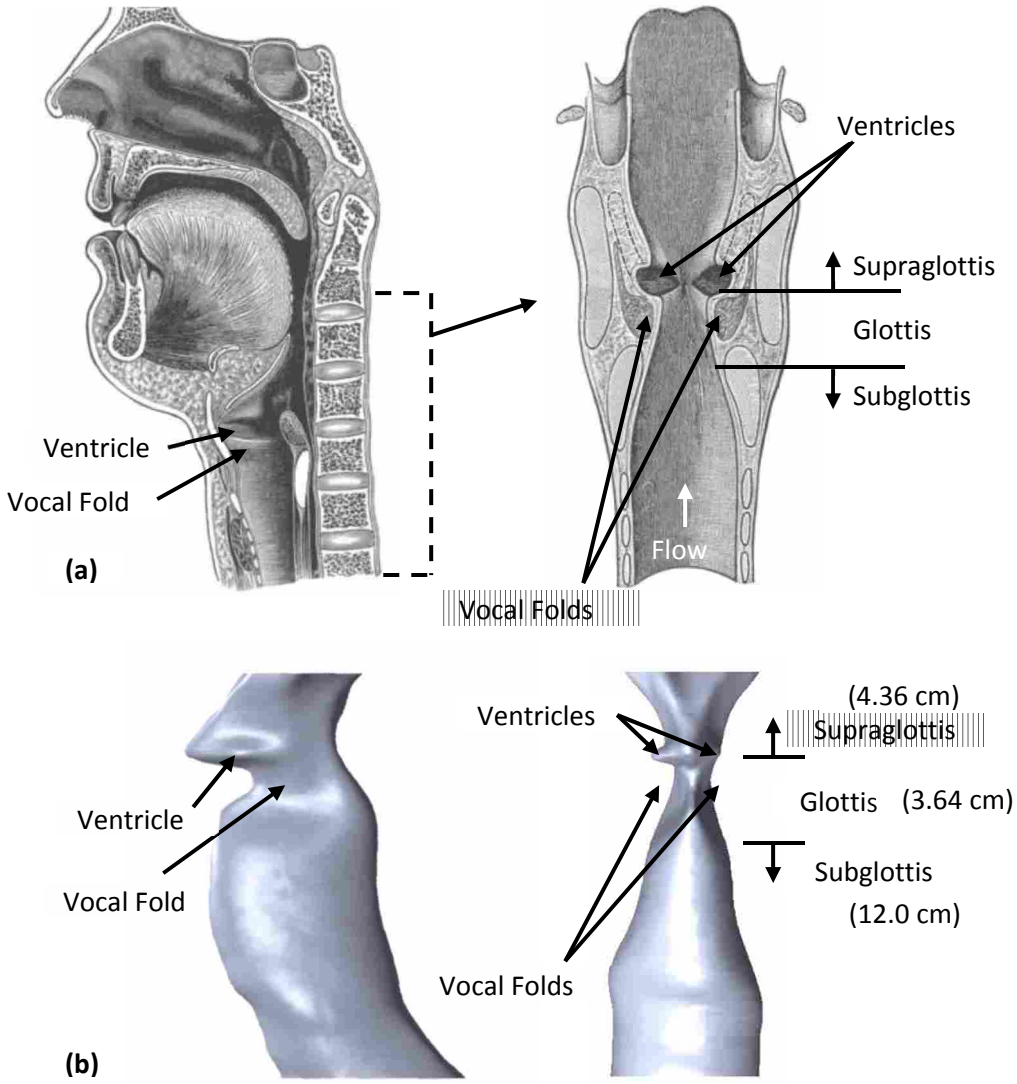

Figure 3-3. (a) Geometry of the human larynx in sagittal (left image) and coronal (right image) planes (adapted from Gray's *Anatomy of the Human Larynx*, images public domain, www.bartleby.com). (b) Airway geometry of original STL file. Views are from the sagittal (left image) and coronal (right image) planes. The dimensions are for the 4x model.

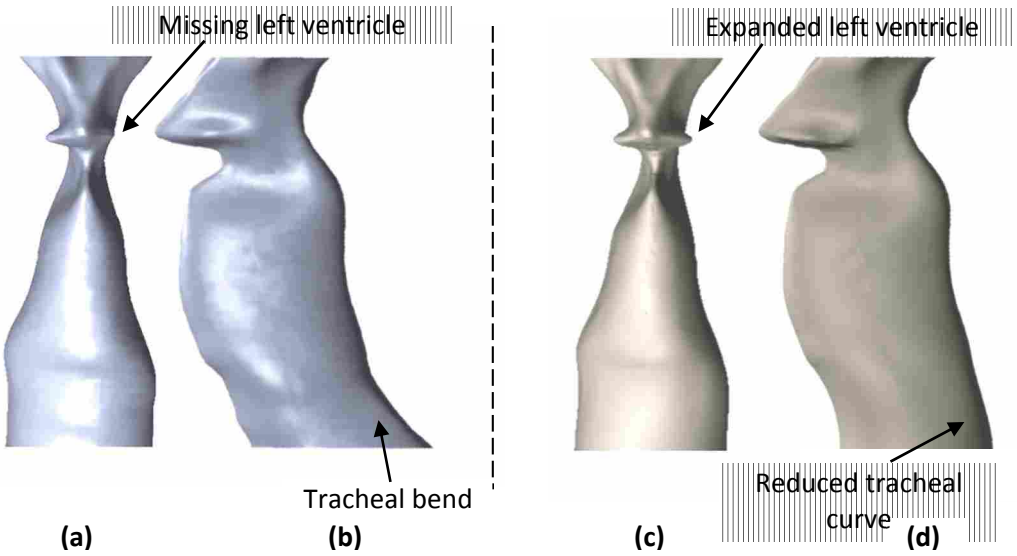

Figure 3-4. (a) Original airway geometry, coronal view. (b) Original airway geometry, sagittal view. (c) Modified geometry, coronal view. (d) Modified geometry, sagittal view.

3.2.2 Subglottal Geometry

A subglottal section containing a simplified subglottic stenosis (narrowing) was designed and built. This section was not used in this study, but since its use is anticipated in future research its construction is mentioned here. The stenosis was a three-dimensional adaption of the two-dimensional stenosis defined by Smith and Thomson (2013). The stenosis was parameterized to allow for different degrees of narrowing to be studied. Silicone models of the normal, non-stenotic (0% obstruction) and the 90% obstruction stenosis were created. Only the normal model was used in this study. Figure 3-5 shows the two subglottal geometries. The subglottal sections were created such that they could be interchanged in the experimental setup.

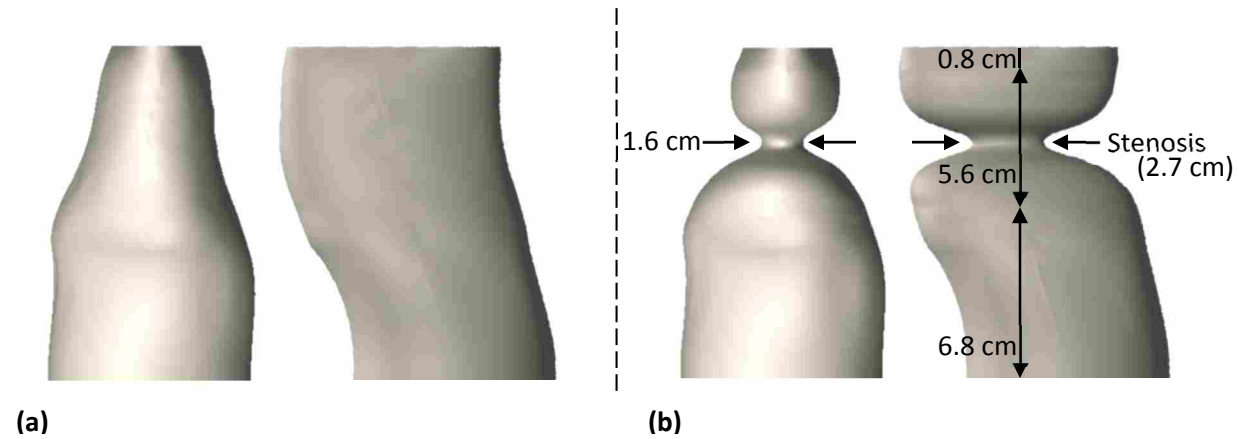

Figure 3-5. Coronal and sagittal views of (a) normal, and (b) 90% stenosis models.

3.2.3 Supraglottal Geometry

The supraglottal section began at the anterior surface of the ventricles and extended through the pharynx (see Figure 3-6). The pharynx geometry was included to model realistic flow resistance during phonation. The geometry was based on vocal tract area function data obtained by Dr. Brad Story at the University of Arizona for the vowel ɑ (Story, 2008). The original geometry was received in a MATLAB file format and included 44 sections that extended from the supraglottal entrance to the oral cavity exit. For this study only sections 1 through 18 (the sections that comprised the supraglottis to the pharynx) were used, and the MATLAB file was converted to an STL file. In SolidWorks the STL file was converted to a solid object by using sectioned splines and surfaces sewn into a solid model, similar to the conversion described in Section 3.2.1. Figure 3-7 compares the truncated pharynx geometry used in this study to the original geometry. The pharynx solid model was attached to the supraglottis through a lofted transition. Coronal and sagittal views of the complete supraglottal model are shown in Figure 3-8.

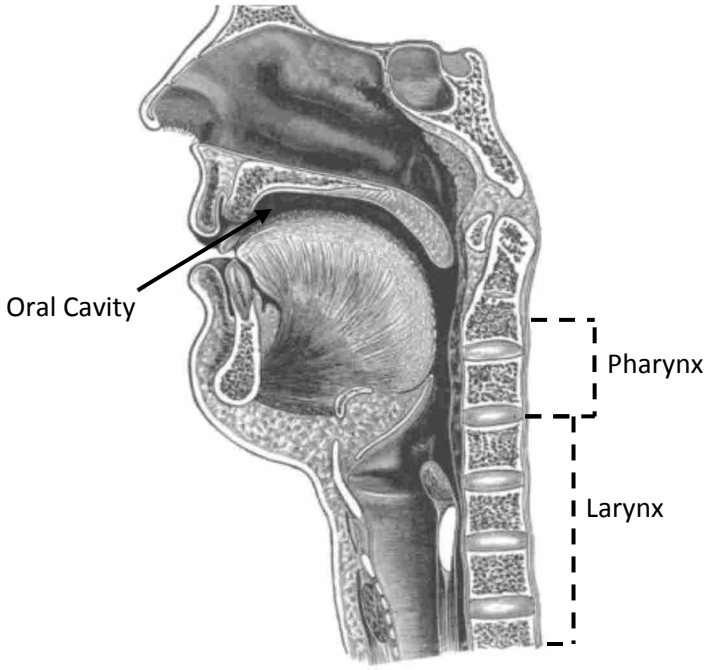

Figure 3-6. Geometry of the human larynx, pharynx, and oral cavity in the sagittal plane (adapted from Gray's *Anatomy of the Human Larynx*, images public domain, www.bartleby.com).

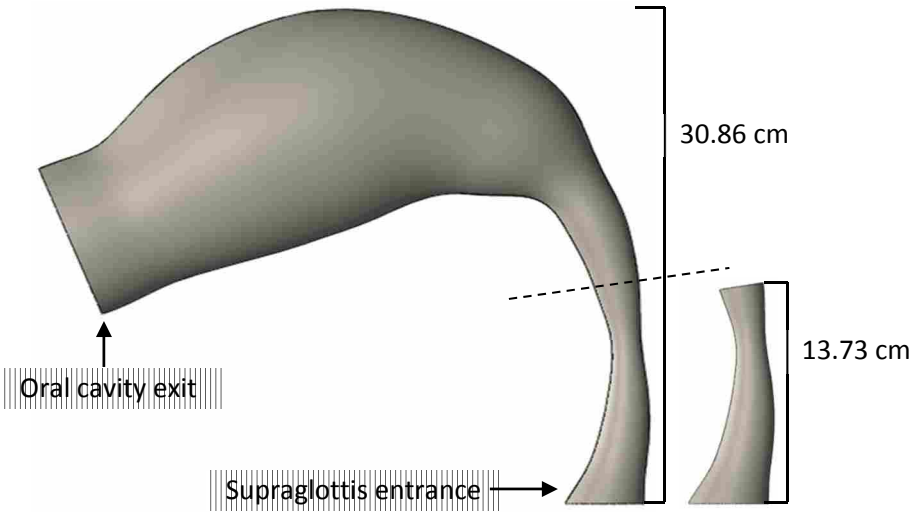

Figure 3-7. Original geometry (left) including the pharynx and oral cavity. Pharynx geometry (right) used for this study.

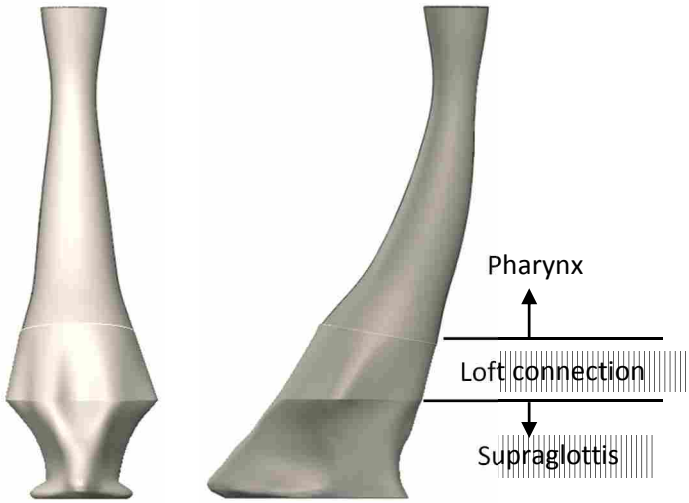

Figure 3-8. Coronal and sagittal views of the supraglottal section, consisting of the supraglottis, loft connection, and pharynx.

3.2.4 Casting of Silicone Models

The silicone models were produced using a method similar to that used by Farley and Thomson (2011) (see Chapter 2). The subglottal 0% and 90% stenosis models and the supraglottal model were prototyped on a three-dimensional printer (ZPrinter® 310, Z Corporation) using soluble plastic powder (zp®131, Z Corporation). The prototypes were coated with several thin layers of polyvinyl acetate to prevent silicone from seeping into the powder and to add surface strength to the prototype. The layers were thin enough to leave the surface geometry essentially unaltered. The prototypes were positioned in rectangular acrylic boxes so that when cured, the anterior and superior openings of each piece aligned with those of the other pieces in the flow circuit. Metal rods extending from the prototype to the exterior of the box left space in the silicone for pressure taps to be inserted once cured (see Figure 3-9). In the subglottal models the tap rods were located 1 cm and 6 cm below the superior surface. In the supraglottal model the rod was positioned 1 cm above the supraglottal entrance. A PVC tube

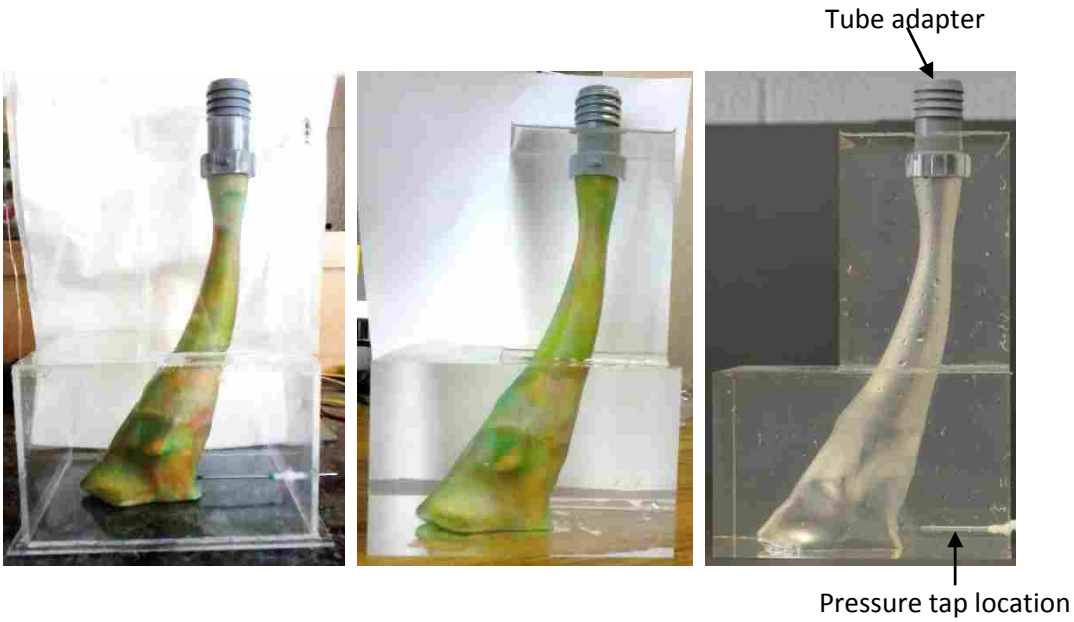

Figure 3-9. Images of the silicone model casting process, as shown for the supraglottis. (Left) The rapid prototype was positioned in an acrylic box, and a metal rod was inserted 1 cm above the inferior surface for later pressure tap insertion. (Middle) Silicone was poured around the prototype and allowed to cure. The acrylic box was then removed. (Right) The prototype was washed out, leaving a silicone model of the airway.

adapter was included at the top of the supraglottal section to connect the test section to the flow system.

Clear silicone (QSil 216, Quantum Silicones) was carefully poured around each prototype, filling the acrylic box. After pouring, a vacuum of 64.14 kPa was pulled on the silicone for 30 minutes to remove all air bubbles and ensure optical clarity. The silicone models were allowed to cure in air at room temperature for 24 hours. The acrylic box and metal rods were then removed. The prototype was dissolved in cold running water, leaving a silicone model with an internal shape of a realistic laryngeal airway, as shown in Figure 3-10.

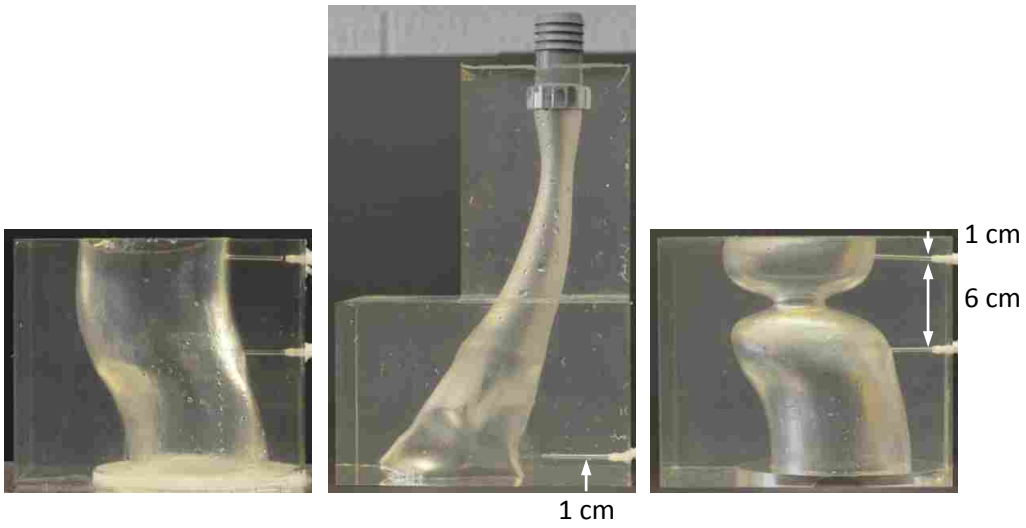

Figure 3-10. Subglottal 0% stenosis, supraglottal, and subglottal 90% stenosis silicone models.

A simplified, cylindrical supraglottis was also constructed for this study (see Figure 3-11). The circular cross section was 7.06 cm in diameter. A piece of PVC pipe was used as the mold for the interior shape. A metal tap rod was inserted 1 cm above the supraglottal entrance for future pressure tap insertion. The cylindrical supraglottis was machined to the same height as the realistic supraglottal piece, and a PVC tube adapter was likewise included at the top of the section. The silicone model was poured, vacuumed, and cured in the same manner as the realistic supraglottal and subglottal sections. Once cured, the acrylic box, metal rod, and PVC pipe were removed, and the silicone section was complete.

3.3 Mechanically-Driven Vocal Folds

The mechanically-driven vocal folds consisted of two counter-rotating, three-dimensional cams, as shown in Figure 3-12. Each cam was covered by a stretched silicone membrane (Dragon Skin® 10, Smooth-On, Inc.) The membrane throughout the glottal opening had a

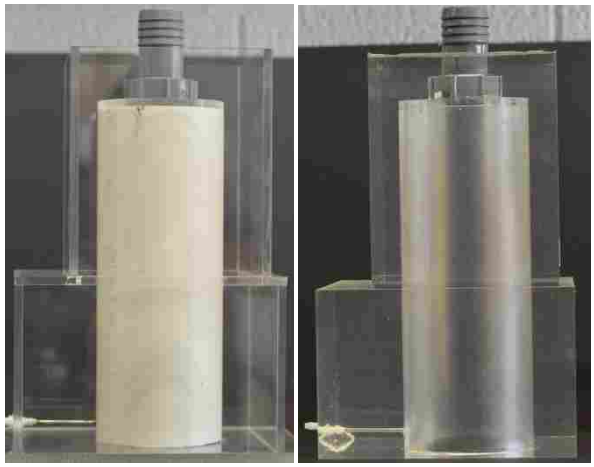

Figure 3-11. Cylindrical supraglottis before (left) and after (right) silicone casting.

uniform thickness of 3 mm prior to stretching and was composed of a 1:1:0.1 (part A, part B, thinner) mixture. Each cam was driven by a 5-phase stepper motor (PK546PMA-R28, Oriental Motor Co. LTD) with a basic step angle of 0.36°. The included encoder encoded at 1000 pulses per revolution. Each motor had a pulse input driver (CRD51-P, Oriental Motor Co. LTD), and was controlled by LabVIEW (National Instruments) by means of a National Instruments digital input module (NI 9411) and bidirectional digital input/output module (NI 9401). Each motor was connected to a cam through a 20 mm diameter gear. Both cams could be driven independently at frequencies between 0 and 10 Hz, and could rotate in or out of phase, depending on user input. The following sections describe this glottal section in detail.

3.3.1 Cam Design

Cam design was based on the mechanically-driven vocal fold model developed at the Institute of Mechanics and Fluid Dynamics at Technische Universität Bergakademie in Freiberg, Germany (Brücker et al., 2004; Kob et al., 2005; Triep and Brücker, 2010). The cams were prototyped on

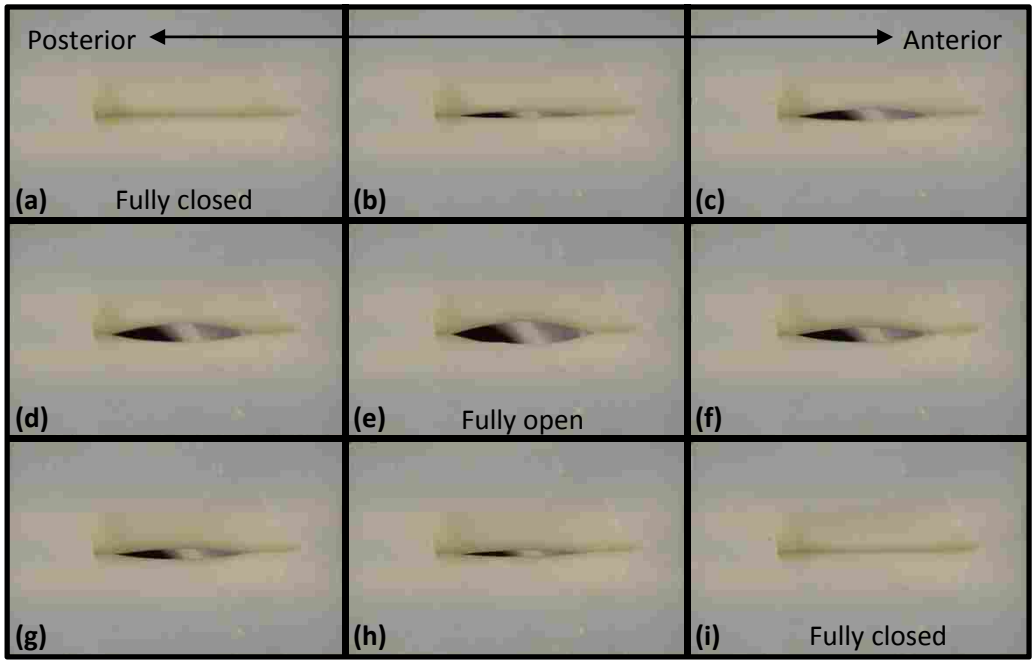

Figure 3-12. Image stills of the mechanically-driven vocal folds during vibration. Flow is out of the page. (a)-(e) The glottis is opening. (f)-(i) The glottis is closing. In (a) and (i) the glottis is fully closed. In (e) the glottis is fully open. Note the white section seen in the open glottis is the entrance to the subglottal opening. Two open phases and nine closed phases are not shown in this image.

a Stratasys® Dimension® 3D printer out of Fused Deposition Modeling™ ABSPlus™ thermoplastic. Figure 3-13 shows the cam shape and dimensions. The cross sections of the ends of the cams were circular, measuring 16 mm in diameter. The central cross section was semi-elliptic. The top part of the cross section was an ellipse with major and minor axes measuring 15.804 mm and 9.274 mm, respectively. The bottom part of the cross section followed a 16 mm diameter circular profile, matching the circular cross sections at the ends of the cam. The semi-elliptic cross-sectional design provided an open quotient of 55% and an alternating periodic convergent-divergent intraglottal profile that was similar to human vocal folds. An open quotient of 55% signifies that the glottis was open or partially open for 55% of each cycle. The circular part of the semi-elliptic shape allowed the glottal opening to completely close for 45% of each cycle.

The glottal length for this model was determined by analyzing videos of vibrating vocal folds during phonation. In the original glottal geometry received from Dr. Hani Bakhshaee the glottis was postured for breathing, not phonation. During breathing the glottis is longer and wider than during phonation, making the glottal length of the original geometry too long for this study. In order to determine the appropriate glottal length four videos of the vibrating vocal folds were analyzed. For each video the glottal length was measured during breathing and during phonation. An average ratio of phonating vs. breathing glottal lengths was found to be 0.67. The glottal length of the original model was 76.1 mm, making the phonating glottal length 51 cm (see Figure 3-13) and the maximum glottal width 9.228 mm.

3.3.2 Three-dimensional Glottal Membrane

A three-dimensional glottal membrane was constructed to cover the cams and to align the entrance and exit of the glottis with the subglottal and supraglottal sections. The original glottal geometry was modified slightly in SolidWorks. The posterior end of the glottis was thinned to make the coronal cross sections more uniform in the anterior-posterior direction. This ensured more uniform stretching across the membrane in the anterior-posterior direction. In the original geometry part of the anterior portion of the glottis was missing. In the modified geometry this portion was filled in. Figure 3-14 shows a comparison of the original and modified solid models of the glottis.

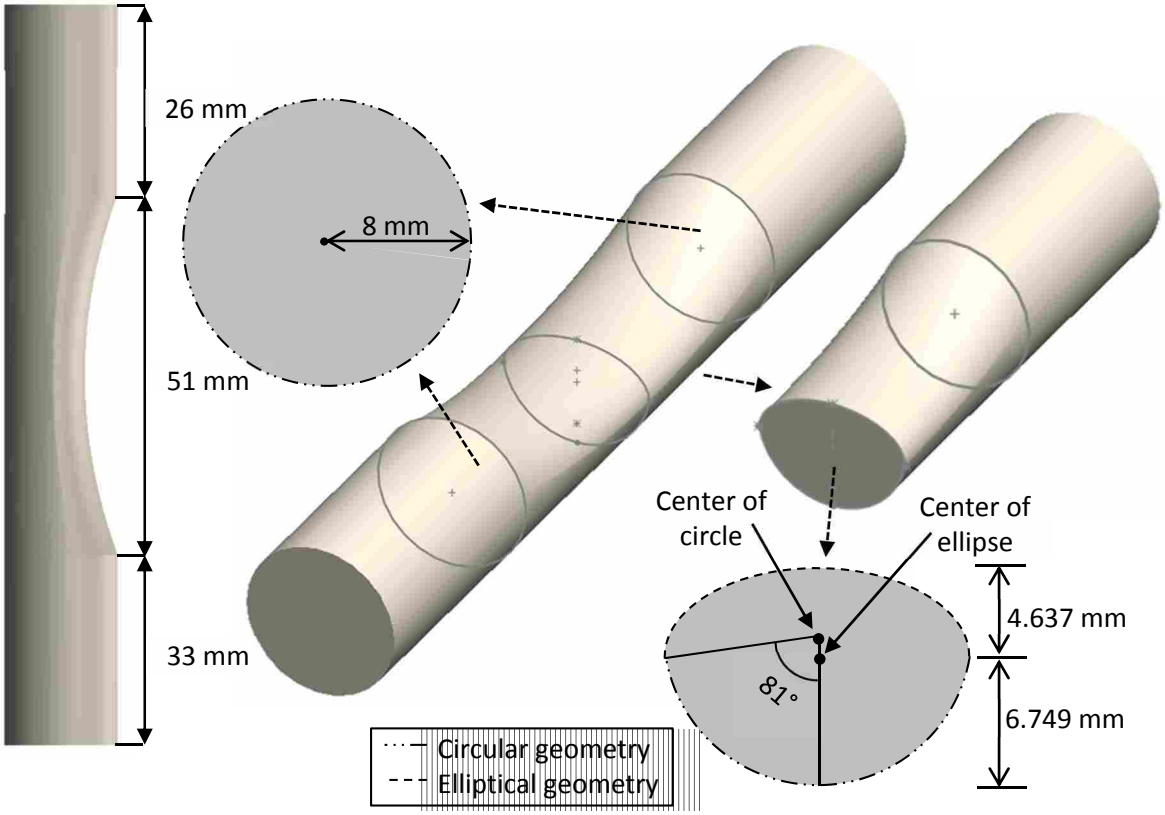

Figure 3-13. Cam geometry and dimensions. The central cross section of the glottal opening was semi-elliptical in the middle and circular on the ends. The glottal opening was offset from center.

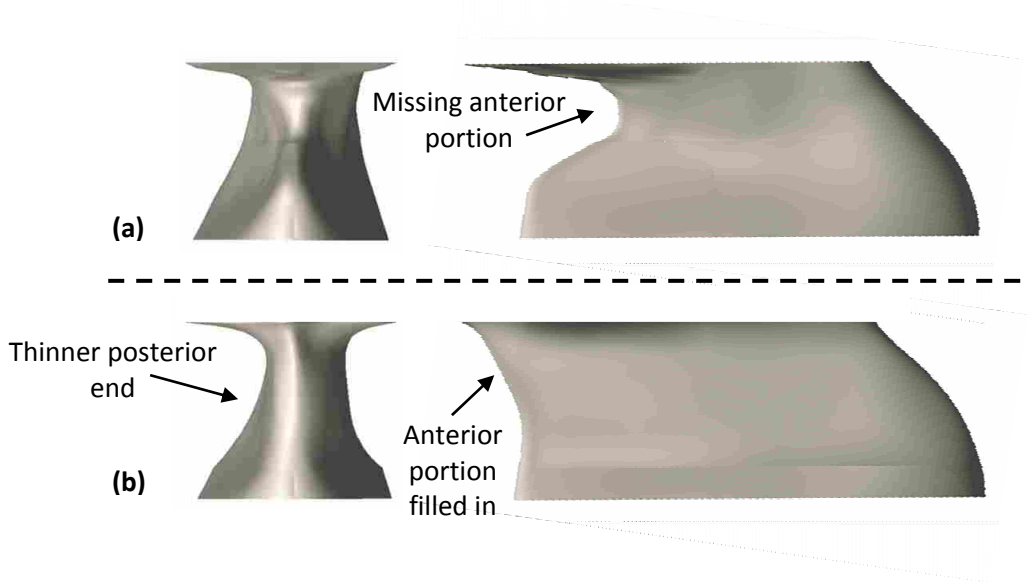

Figure 3-14. Coronal and sagittal views of the (a) original glottal geometry, and (b) modified glottal geometry.

A 3 mm-thick shell of the modified glottal geometry was created in SolidWorks, and the shell and modified glottal geometry were rapid prototyped on a three-dimensional printer (ZPrinter® 310, Z Corporation) using the same soluble plastic powder used in the subglottal and supraglottal models. Both were coated with several thin layers of polyvinyl acetate to prevent silicone seeping into the powder and to add surface strength to the prototype. The shell was used to create a rigid plastic mold (Smooth-Cast® 310, Smooth-On, Inc.) The modified prototype and the plastic mold were combined to create a 3 mm-thick opening surrounding the glottis. A 1:1:0.1 ratio of pliable silicone (Dragon Skin® 10 Fast, Smooth-On, Inc.) and thinner (Silicone Thinner®, Smooth-On, Inc.) was poured into the opening and allowed to cure. Figure 3-15 shows the development of the glottal membrane during the molding and curing process and the final glottal section. Glass support plates, 2.5 mm thick, were cut out to match the entrance and exit geometry of the membrane. A 6.35 mm-thick opening was left at the top and bottom of the

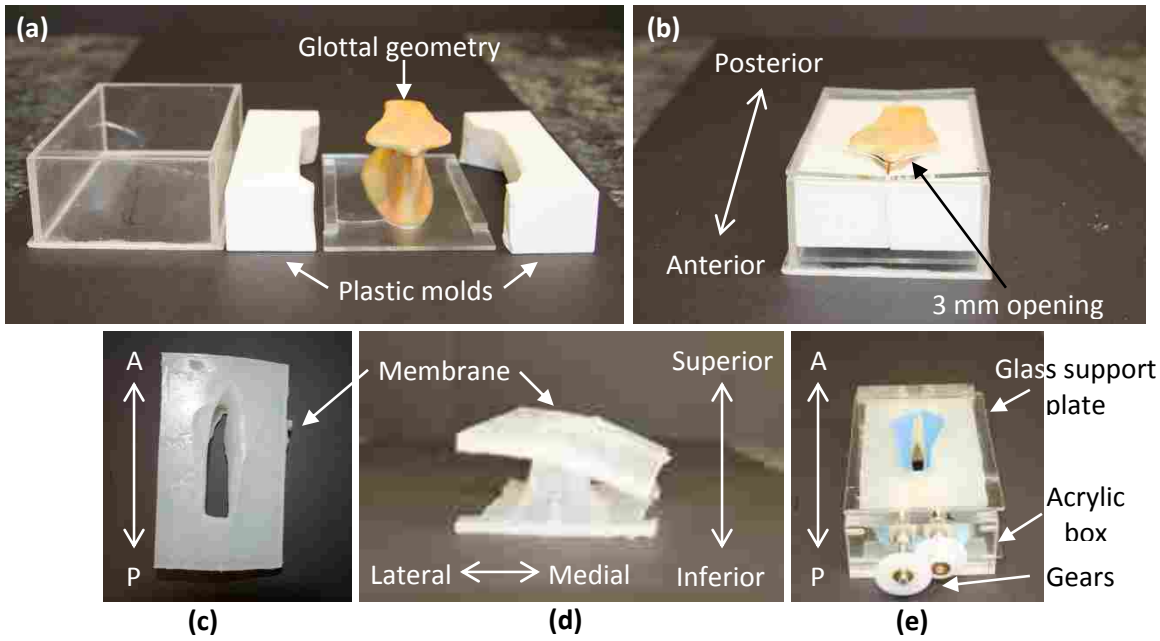

Figure 3-15. (a) Molds for creating glottal membrane. (b) Fully assembled mold. (c) View of the superior surface of the membrane. (d) Coronal view of the membrane. (e) Superior view of fully assembled glottal section, including glass support plates, acrylic box, and gears. In this image the membranes were coated with several layers of a stiffer silicone seen in blue, not included in the final model.

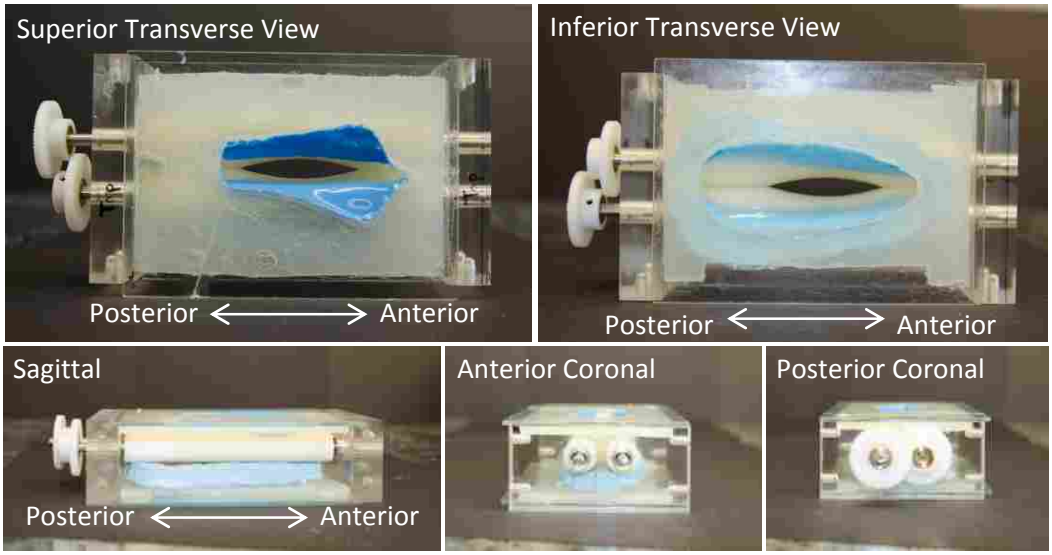

Figure 3-16. Final assembly of the glottal section, including glass support plates, acrylic box, cams, and gears. Note that the sides of the acrylic box were removed for these images for internal viewing. Also note in this model the membranes were coated with several layers of a stiffer silicone (Smooth-Sil® 935, Smooth-On, Inc.), seen in blue, that were not included in the final model.

mold to provide a larger silicone surface to attach to the glass support plates. Figure 3-16 details the final glottal membrane construction, including the cams, the glass support plates, and an acrylic support box for structural stability. The attached gears meshed with the stepper motors.

3.4 Flow Conditioning

A flow conditioning tank, shown in Figure 3-17, was used to facilitate laminar flow entering the subglottis. The tank was constructed of a 30.3 L plastic bucket, approximately 46 cm diameter. The flow entered at the base of the tank and was distributed throughout the base of the tank by passing through an intersection of 2.54 cm PVC dispersion pipes and exiting through a series of holes in the undersides of the pipes (see Figure 3-17 and 3-18). The fluid then rose through a 1.27 cm acrylic support plate with a grid of 1.27 cm square cutouts, three layers of plastic mesh screening, and 7.6 cm of aquarium grade gravel. Another layer of plastic mesh screening was placed above the gravel to prevent gravel displacement.

The flow passed through a three-dimensional ultra-high-molecular-weight polyethylene contraction that directed laminar flow to the subglottis. The contraction had an axially-varying circular cross section with dimensions as shown in Figure 3-19 and was machined on a CNC lathe. The geometry of the contraction was based on the findings of Blair and Cahoon (2006). The contraction hung into the tank 8.26 cm, and during use the tank was completely filled with fluid. The exit of the contraction was 7.62 cm in diameter to provide a smooth connection with the subglottal silicone sections.

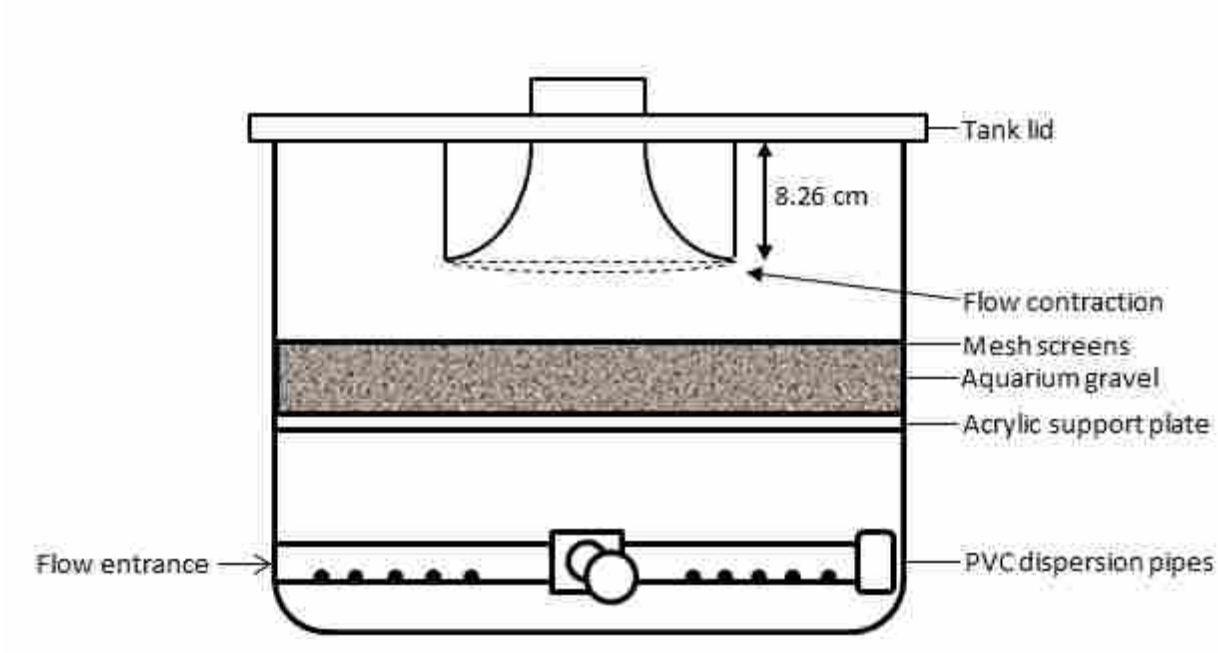

Figure 3-17. Internal view of the flow conditioning tank. Flow entered through dispersion tubes, rose through the plate-gravel-mesh system, and entered the subglottis through the flow conditioning contraction.

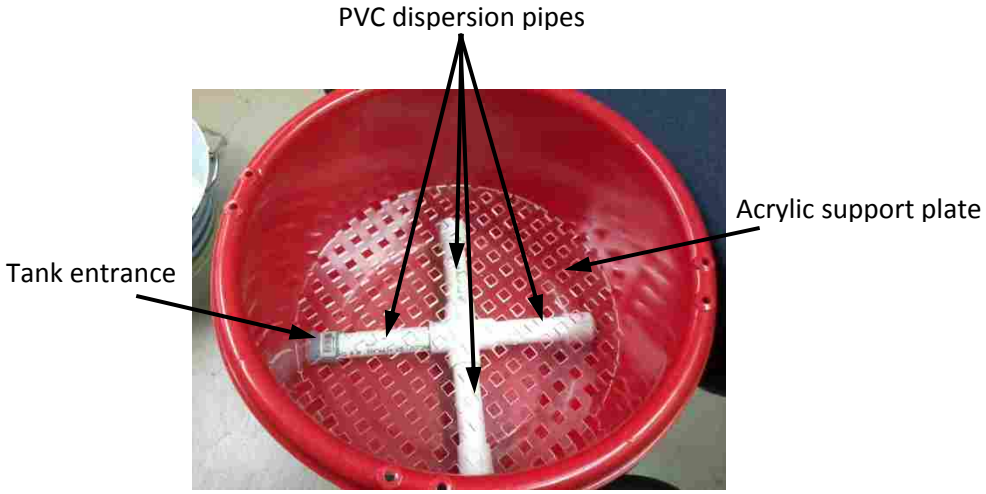

Figure 3-18. Image of flow dispersion pipes and acrylic support plate.

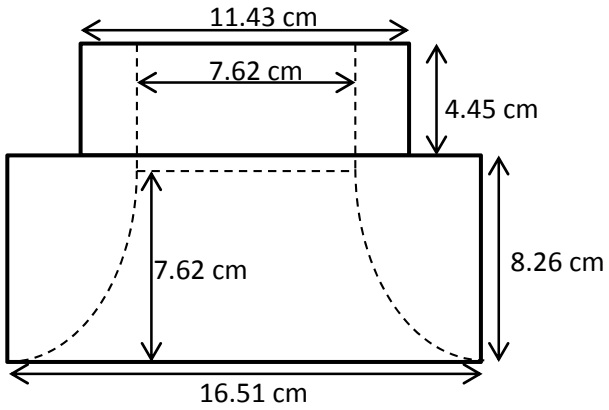

Figure 3-19. Flow conditioning contraction upstream of the subglottis.

3.5 Index Matching

Index matching was performed similar to the process described in Section 2.2.2. A mixture (52% glycerol, 48% water by volume) was used as the working fluid to match the index of refraction of the silicone ($n \approx 1.406$; Quantum Silicones, 2012). The kinematic viscosity and density of the fluid were calculated according to Cheng (2008), and found to be $\nu = 7.3355 \times 10^{-6}$ m^2/s, and $\rho = 1150.4$ kg/m^3, respectively. Figure 3-20 shows the effect of refractive index matching when the model was filled with air, water, and the optimal glycerol-water mixture.

To find the correct glycerol-water mixture for the silicone models, the 90% subglottic stenosis silicone model was partially filled with a starting mixture of 50% glycerol, 50% water.

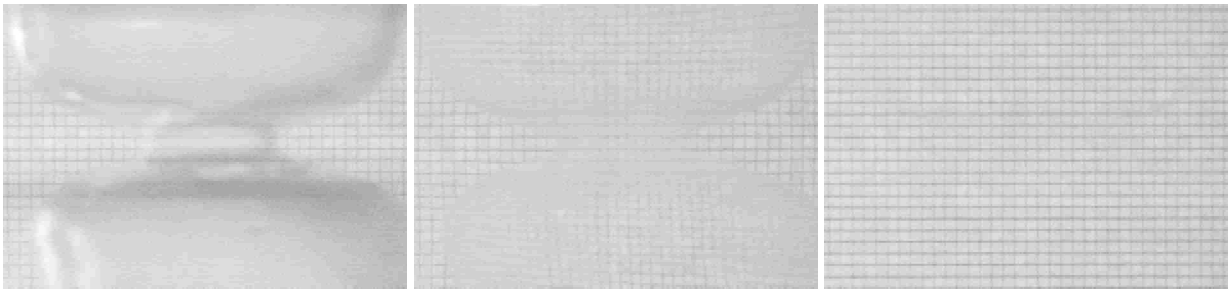

Figure 3-20. Grid placed behind the 90% stenotic section with the section filled with (a) air, (b) water, and (c) 52%-48% glycerol-water solution. Note the absence of optical distortions in (c).

A paper with a grid pattern (10 squares per inch) was placed behind the model and an image was taken (Figure 3-21). Glycerol was then added to the mixture to raise the glycerol content by one percent (51% glycerol, 49% water), and another image was taken. This process was repeated up to 55% glycerol, 45% water. The images were inspected for minimum grid distortion to determine the correct glycerol-water mixture.

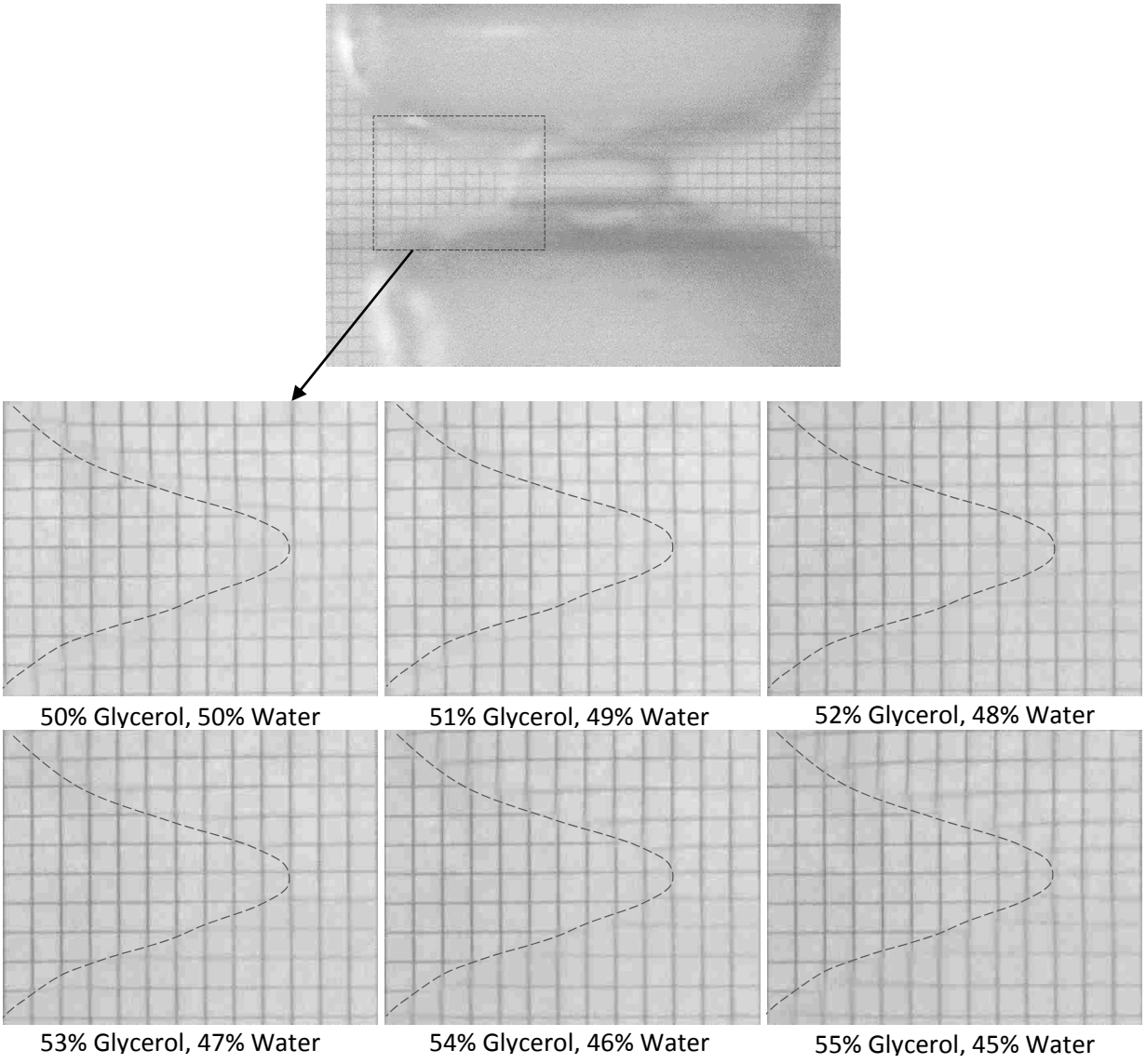

Figure 3-21. Comparison of glycerol-water mixtures. The dotted line highlights the shape of the airway. The cavity is to the right of the dotted line. The optimal fluid mixture that matches the index of refraction of the silicone is 52% glycerol, 48% water. Distortions of the grid between the silicone (left of the dotted line) and the fluid filled cavity (right) can be detected for all other mixtures.

4 CHARACTERIZATION OF THE SUPRAGLOTTAL JET IN A COMPLEX LARYNX MODEL

4.1 Overview

Characterization of the laryngeal jet is important for understanding the physics of voice production. Research in recent decades has contributed much to the understanding of voice production and laryngeal flow structures, but most studies have been conducted in models with either no vocal tract (e.g. a free jet), or a uniform vocal tract. In this study PIV measurements of the supraglottal jet were conducted in a realistic vocal tract model downstream of mechanically-driven vocal folds. Axis switching and starting and closing vortices were observed, and comparisons of PIV data in a realistic and uniform vocal tract are made.

4.2 Introduction

Human voice is an important tool for communication in both professional and personal interactions. Figure 4-1 illustrates laryngeal anatomy and flow direction. Voicing is produced as air from the lungs is pushed upwards through the larynx, producing flow-induced vibration of the vocal folds. Laryngeal airflow affects vocal fold vibration and speech quality. The National Institute on Deafness and Other Communication Disorders (NIDCD) reports that approximately 7.5 million people are affected by voice disorders in the United States alone (NIDCD, 2010).

The widespread impact of voice disorders makes a thorough understanding of the physics of voice production, including that of laryngeal flow structures, of significant potential benefit.

Many experimental studies and computational studies have been conducted to further our understanding of the field. Experimental studies have been conducted using vocal fold models, including static, driven, self-oscillating, and excised larynx models, and have often focused on supraglottal aerodynamics. However, optical access has limited these investigations to simplified supraglottal geometries (e.g. a straight tube representing the vocal tract) or to a free jet without supraglottal structures. Computational models have also been used to study laryngeal flow, but these models are computationally expensive and still need to be validated using physical models.

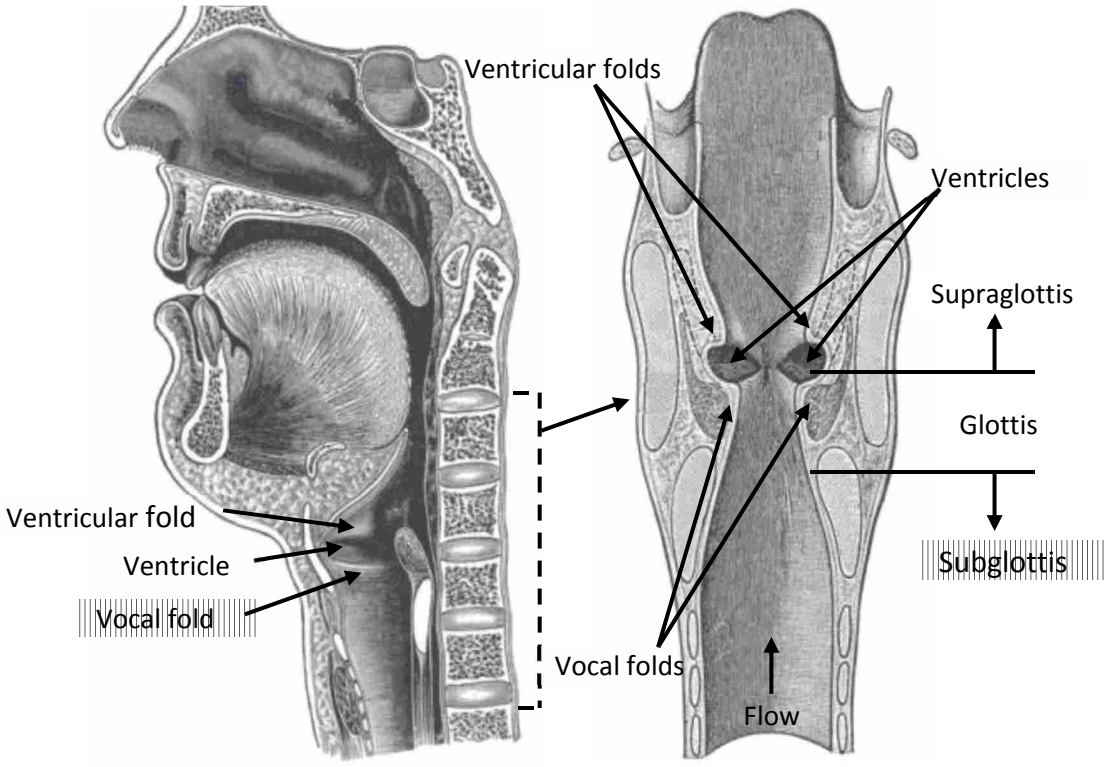

Figure 4-1. Geometry of the human larynx in sagittal (left) and coronal (right) planes (same as Figure 1-1, from Gray's *Anatomy of the Human Larynx*, images public domain, www.bartleby.com). Adapted from Smith (2011).

Studies using self-oscillating models noted vortices during glottal opening and skewing of the glottal jet (Drechsel and Thomson, 2008), as well as jet axis switching (Krebs et al., 2011). An investigation of the velocity field above excised canine larynges with no vocal tract revealed starting vortices, Kelvin-Helmholtz vortices, and entrainment vortices at various phases of the glottal cycle (Khosla et al., 2007). Triep and Brücker (2010) also noted Kelvin-Helmholtz vortices in a driven vocal fold model. A numerical study of intraglottal velocity and pressure fields using static vocal folds and a uniform vocal tract (Mihaescu et al., 2010) also noted vortical structures. The observed vortices formed on the divergent wall of the glottis, were intermittently shed, and increased in size and strength as they convected downstream due to entrained air from the supraglottal region. Driven vocal fold models with uniform vocal tracts both with (Triep et al., 2005) and without (Erath and Plesniak, 2010) ventricular folds noted the "Coanda effect" (the tendency of a fluid jet to be attracted to a nearby surface) during glottal opening and vortices formed above the vocal folds during glottal closing. Other driven vocal fold models (Kirmse et al., 2010; Triep and Brücker, 2010) also observed axis switching of the glottal jet. Thus far these flow structures have been observed in vocal fold models containing no supraglottis (free jet) or uniform vocal tracts. It is important to determine if such laryngeal flow structures observed in models with simplified supraglottal geometries are also observed in realistic geometries.

Several studies (Drechsel and Thomson, 2008; Triep et al., 2005; Triep and Brücker, 2010) have compared glottal jet flow structures for uniform vocal tracts with and without ventricular folds. Drechsel and Thomson (2008) found that the ventricular folds interfered with vortices formed during opening glottal phases, and documented the impact of ventricular folds on jet skewing in an asymmetric model. Triep et al. (2005) noted that the jet front was slightly

retarded and the radial spread of the glottal jet was more pronounced when ventricular folds were included in the vocal tract. A later study by Triep and Brücker (2010) found that the presence of ventricular folds reduced pressure loss and stabilized the jet during glottal closing. These studies suggest that supraglottal geometry impacts laryngeal flow. Further research is needed to determine the extent of that impact on laryngeal flow.

In a recent study (Xue et al., 2014) a computational model of a subject-specific human larynx model was created to study the effects of realistic geometry on vocal fold vibration and glottal flow. A model of the human larynx from computed tomography (CT) scan data was used. This study was the first detailed study to investigate glottal flow in a realistic supraglottis. The investigation observed anterior-posterior asymmetries in vocal fold vibration and glottal flow, and a lack of strong jet deflection that had been observed in previous studies. Results of this computational study need to be validated on a physical model, and further exploration is needed.

Until recently, the ability to study laryngeal airflow in a realistic physical model was hindered by lack of optical access to the complex interior. As described in Chapter 2, Farley and Thomson (2011) developed a method for studying flow structures within a static complex laryngeal geometry using particle image velocimetry (PIV), a common method for acquiring spatially-resolved flow field data. PIV data acquisition within complex geometries had previously been impossible due to refraction from complex inner surfaces that impede accurate data acquisition. In the method used by Farley and Thomson the refraction difficulty was overcome by creating a model with flat, smooth outer surfaces, and by matching the index of refraction of the working fluid with that of the surrounding material, making it possible to study laryngeal flow structures in models containing more realistic subglottal and supraglottal geometries.

A similar method is used in the work described in this chapter, adapted for use with a mechanically-driven vocal fold model. The purpose of this study is to investigate glottal flow structures in a dynamic laryngeal model with realistic vocal tract geometry and to determine whether flow features observed in previous studies with uniform vocal tracts still occur.

4.3 Methods

4.3.1 Silicone Models

The laryngeal (subglottis, glottis, and supraglottis) geometry used in this study was derived from computed tomography (CT) scans obtained from Dr. Hani Bakhshaee (Bakhshaee et al., 2013) at McGill University. A pharyngeal section was included in this study to model realistic flow resistance during phonation and will be considered part of the supraglottal section. The pharynx geometry was based on vocal tract area function data obtained by Dr. Brad Story at the University of Arizona (Story, 2008) for the vowel ɑ. Silicone models of the subglottis and supraglottis were created using a method similar to that used by Farley and Thomson (2011). Figure 4-2 shows the completed silicone models used in this study (refer to Section 3.2 for more details).

4.3.2 Experimental Setup

Figure 4-3 illustrates the experimental setup. The silicone models and driven vocal fold section were located within a closed flow loop. A pump was used to drive the fluid through the closed system. Downstream of the pump the flow passed through a flow meter, into a flow conditioning tank, and through the laryngeal test sections. The flow conditioning tank consisted of dispersion pipes, gravel, and a three-dimensional contraction that conditioned the flow entering the subglottis. Pressure taps were included in the subglottis and supraglottis, from which

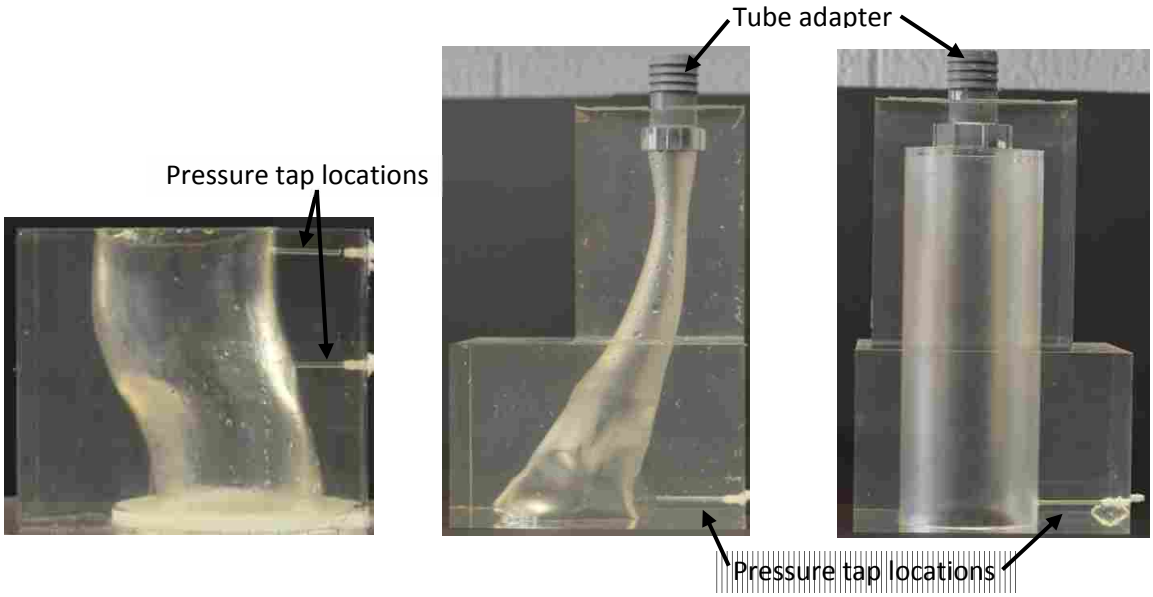

Figure 4-2. Subglottal (left), realistic supraglottal (center), and cylindrical supraglottal (right) silicone models.

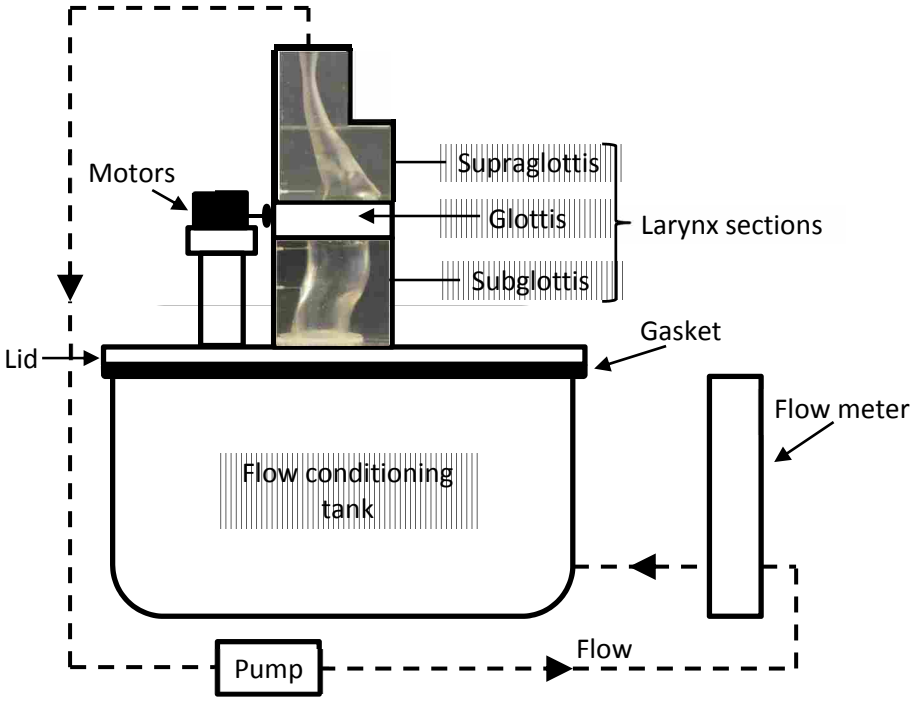

Figure 4-3. Schematic of the closed-loop experimental setup. Fluid was driven by a pump, through a flow meter, a flow conditioning tank, and upwards through the synthetic larynx (same as Figure 3-1).

Table 4-1. Flow rate and pressure for each experimental case.

Case	Flow rate (model)	Flow rate (life-sized)	Pressure (model)	Pressure (life-sized)
Cylindrical Geometry	189 ml/s	101 ml/s	3.70 kPa	0.28 kPa
Realistic – Matched Flow Rate	189 ml/s	101 ml/s	6.67 kPa	0.51 kPa
Realistic – Matched Pressure	142 ml/s	70 ml/s	3.70 kPa	0.28 kPa

transglottal pressure was recorded using a custom bidirectional gage pressure transducer (ID: MMDWB2.5BIV1P4C0T1A3CE, Omega Engineering, Inc.) with an accuracy of 4%. The working fluid consisted of 52% glycerol, 48% water by volume to match the index of refraction of the subglottal and supraglottal silicone models. The method of index matching is described in more detail in Section 3.5.

One data set was collected with the cylindrical supraglottal geometry and two data sets were collected with the realistic supraglottal geometry. Flow rate and pressure values for each set are given in Table 4-1. Pressure tap locations used to measure the transglottal pressure were located 1 cm above and 1 cm below the glottis (see Figure 4-2). For the cylindrical supraglottal model data set, the average transglottal pressure was set to 3.70 kPa and the average flow rate was 189 ml/s, corresponding to 0.28 kPa and 101 ml/s in air for a life-sized larynx. For the realistic supraglottal model data sets, the first set of realistic data was set to the same flow rate as in the cylindrical geometry, making the average transglottal pressure 6.67 kPa, corresponding to 0.51 kPa in air for a life-sized model. This data set will be referred to as the "realistic geometry – matched flow rate" set, or just "matched flow rate." The second realistic PIV data set was collected with an average transglottal pressure equal to the average transglottal pressure of the

cylindrical geometry and a flow rate of 142 ml/s, corresponding to 70 ml/s in air for a life-sized larynx. This data set will be referred to as the "realistic geometry – matched pressure" set, or just "matched pressure." The average transglottal pressure during phonation is 0.4 to 1.2 kPa, making the average transglottal pressures of the cylindrical and matched pressure cases slightly lower than those encountered during human phonation. The flow rate during phonation ranges from 70 to 200 ml/s (Baken and Orlikoff, 2000). The experimental flow rates in this study are in good agreement with those expected during human phonation (see Table 4-2). The mechanically-driven vocal folds rotated at 3 Hz, corresponding to 103 Hz in human phonation. Pressure, flow rate, and frequency were converted to life-sized values by assuming dynamically similar Reynolds and Strouhal numbers.

Reynolds and Strouhal numbers for the experimental models were similar with those of normal human speech. The order of magnitude of these important characteristics were calculated as follows for life-sized conditions in air:

$$\mathrm{Re} = u_{\mathrm{mean}} \cdot w_{\max}/\nu \approx O(10^3)$$

$$\mathrm{St} = f \cdot w_{max}/u_{\mathrm{mean}} \approx O(10^{-2})$$

where u_{mean} is the mean velocity through the glottis, $w_{\max}$ is the maximal glottal width, f is the fundamental vocal fold frequency of oscillation, and ν is the kinematic viscosity. Physiological parameters for human speech were derived by Pelorson et al. (1994), and were as follows: u_{mean} = 20-40 m/s, $w_{\max}$ = 1-3 mm, and f = 100-200 Hz. The life-size Reynolds number was 127.4 to 764.3, and the Strouhal number was 2.5×10^{-3} to 3×10^{-2}.

The Reynolds number for the model used in this study was calculated using the average flow rate measured upstream of the glottis:

$$\mathrm{Re} = Q \cdot w_{\max}/\nu \cdot A \approx O(10^3)$$

where Q was the average flow rate, and A was the cross-sectional area of the pipe downstream of the flow conditioning tank. Reynolds number for the model was 543.2 to 723.0, and the Strouhal number was 3.6×10^{-2} to 4.8×10^{-2}. For the remainder of the chapter all pressure, flow rate, and velocity values given are relative to the experimental model unless otherwise stated.

The flow was seeded with hollow glass spheres, approximately 5 to 25 μm diameter (110P8, Potters Industries, Inc.) PIV measurements were acquired in three sagittal and three coronal cross sections, as shown in Figure 4-4, using a double-pulsed 532 nm laser (New Wave Laser, Solo II-15 Nd:YAG, Fremont, CA) and a synchronized camera (LaVision Imager Intense, Goettingen, Germany). At each cross section phase-locked ensemble-averaged PIV data were collected at 20 phases per cycle, with phases occurring every 18°. For each phase 10 image pairs were recorded at 4.95 frames/second with a resolution of 1376×1024 pixels and a 250 μs inter-frame delay.

Table 4-2. Comparison of parameters for the model used in this study, the corresponding values for a life-sized model in air, and the average parameters of human phonation.

Parameter	Model	Life-size	Human
u_{mean}	-	-	20-40 m/s
w_{max}	8 mm	2 mm	1-3 mm
ν	7.34×10^{-6} m^2/s	-	15.7×10^{-6} m^2/s
Q	142-189 ml/s	70-101 ml/s	70-200 ml/s
f	3 Hz	103 Hz	100-200 Hz
ΔP	3.69-6.59 kPa	0.28-0.5 kPa	0.4-1.2 kPa
Re	$O(10^3)$	-	$O(10^3)$
St	$O(10^{-2})$	-	$O(10^{-2})$

The velocity fields for each phase were analyzed using an FFT-based cross-correlation algorithm to determine particle displacement and velocity vectors. Multiple passes with successively smaller interrogation regions were used, beginning with 64×64 pixel windows and a 50% overlap, and ending with 16×16 windows (also with a 50% overlap). Resulting velocity fields were ensemble-averaged.

The PIV images were calibrated using a raw PIV image from each plane of each experimental case. Two points of known location were selected at the supraglottal entrance in each image. For each plane, the distance between the two points was known and used to establish a scale.

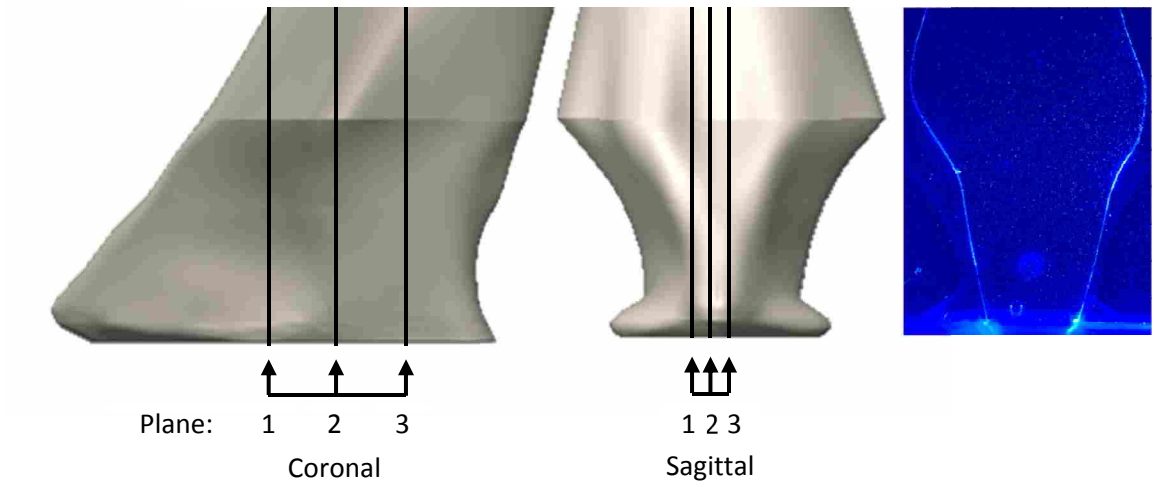

Figure 4-4. (Left) and (Middle): Arrows denoting approximate locations of sagittal and coronal image planes, respectively (not to scale). Distance between adjacent planes was approximately 6 mm in the coronal direction, and 3 mm in the sagittal direction. (Right): Raw PIV image, corresponding to plane 3 in the coronal direction.

4.4 Results and Discussion

PIV data were collected at phase increments of 18° during rotation. Phase 0° corresponds to the beginning of glottal opening. Figure 4-5 compares the waveform of the glottal area to the transglottal pressure waveform. The glottal area for each phase was calculated from images of the glottis (during which the supraglottis had been removed to allow better imaging of the glottis). As is shown, the glottis began to open at 0°, reached maximum glottal opening (maximum glottal area) at 90°, and closed at 180°.

4.4.1 Pressure Comparisons

Figure 4-5b is a comparison of the transglottal pressure waveforms for the three cases (cylindrical, realistic-matched flow rate, realistic-matched pressure). Information on pressure data calibration and uncertainty is given in Appendix C. All pressure data in this chapter are the calibrated pressures. Maximum transglottal pressures for the cylindrical and matched flow rate cases occurred during the opening phases of the glottis (at 42°), rather than during the closed phases, as expected. For the cylindrical case maximum transglottal pressure was 7.37 kPa, and for the matched flow rate case it was 11.83 kPa. Maximum transglottal pressure of 7.00 kPa for the matched pressure case occurred just before opening at 351°, and remained fairly constant (between 6.89 and 6.94) from 0° to 42°. Pressure values declined quickly after 42°. It is unclear why the peak pressures occurred while the glottis was open for the cylindrical and matched flow rate cases, but may be due to fluid inertia creating a lag in the peak transglottal pressures.

For all three cases minimum transglottal pressure occurred after the moment of maximum glottal opening. For the cylindrical case the minimum transglottal pressure was −0.90 kPa at 153°, for the matched flow rate case the minimum transglottal pressure was −1.85 kPa at 123°,

and for the matched pressure case it was −1.37 kPa at 111°. Triep and Brücker (2010) found a similar phenomenon, noting that the maximum volume rate occurred after the instant of maximum glottal opening.

For all three cases the transglottal pressure equaled zero at two phases. Both realistic cases had zero transglottal pressure at nearly the same phases, occurring just after maximum glottal opening (102° for the matched flow rate case, and 93° for the matched pressure case), and as the glottis closed (152° for the matched flow rate case, and 149° for the matched pressure case). The phase of zero transglottal pressure for the cylindrical case lagged both of the realistic cases, with zero transglottal pressure occurring at 129° (as the glottis closed), and 180° (just after the glottis closed).

4.4.2 PIV Data

Figures 4-6 through 4-8 show the PIV data for all three experimental cases. Figure 4-9 is a comparison of the midplane PIV data for all three cases. Note that the gray occlusion visible through the glottal opening in the "Glottal Image" column is the entrance to the subglottis, located 16.8 cm below the glottis.

4.4.2.1 Cylindrical Supraglottal Data

PIV data for the cylindrical geometry are shown in Figure 4-6. The average transglottal pressure was set to 3.70 kPa and the average flow rate was 189 ml/s. The highest velocities for each phase were seen along the midplane (plane 2) in both the sagittal and coronal planes. Development of the supraglottal jet was first seen at 36°, peaked at 72°, and then tapered off as the vocal folds began to close. The peak velocity was 2.13 m/s in the scaled up model, which

corresponds to 18.21 m/s life-sized. A small secondary spike in jet velocity was seen in the coronal and sagittal midplanes in 198° and 216°.

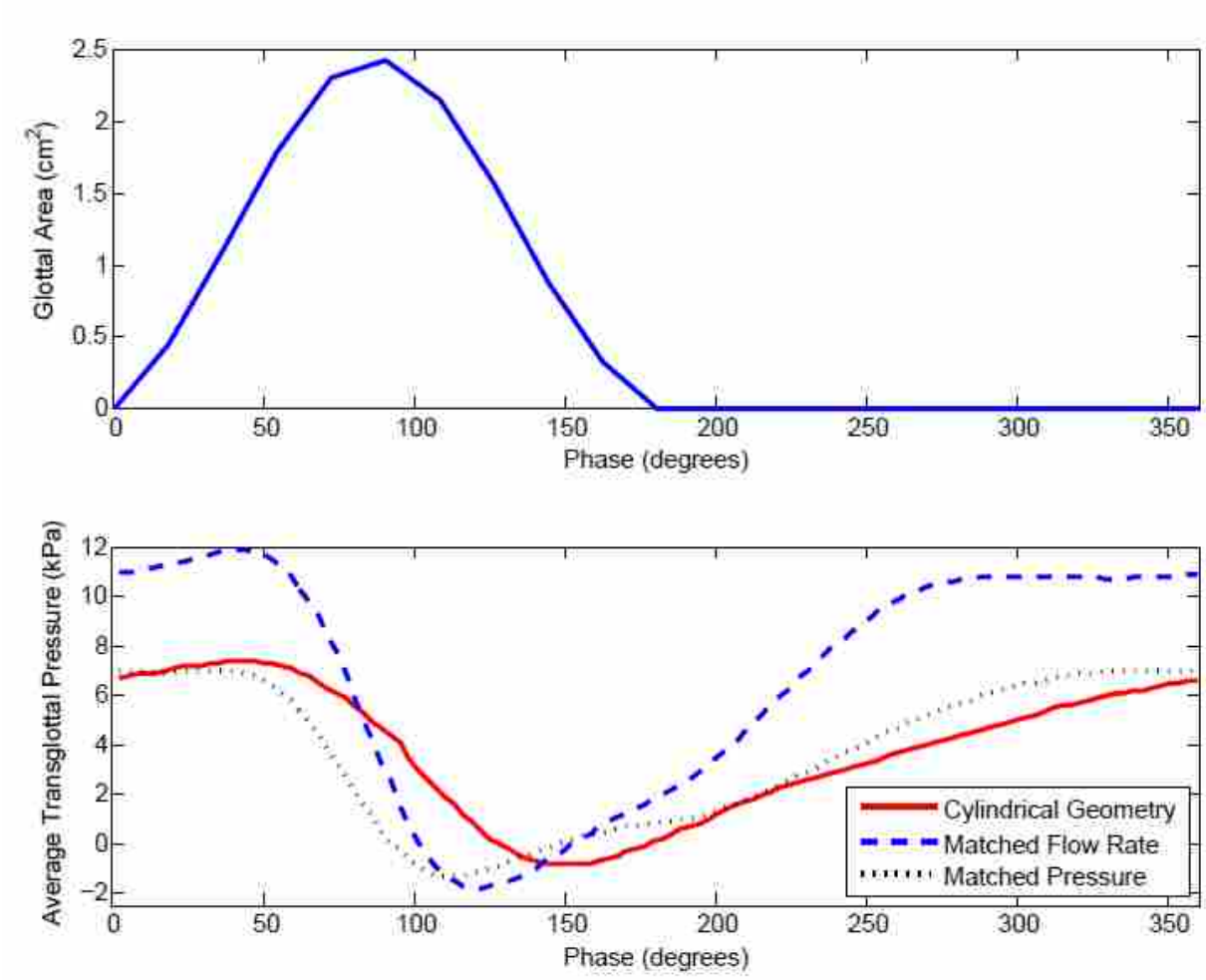

Figure 4-5. Glottal area (top) and average transglottal pressure (bottom) waveforms vs. phase.

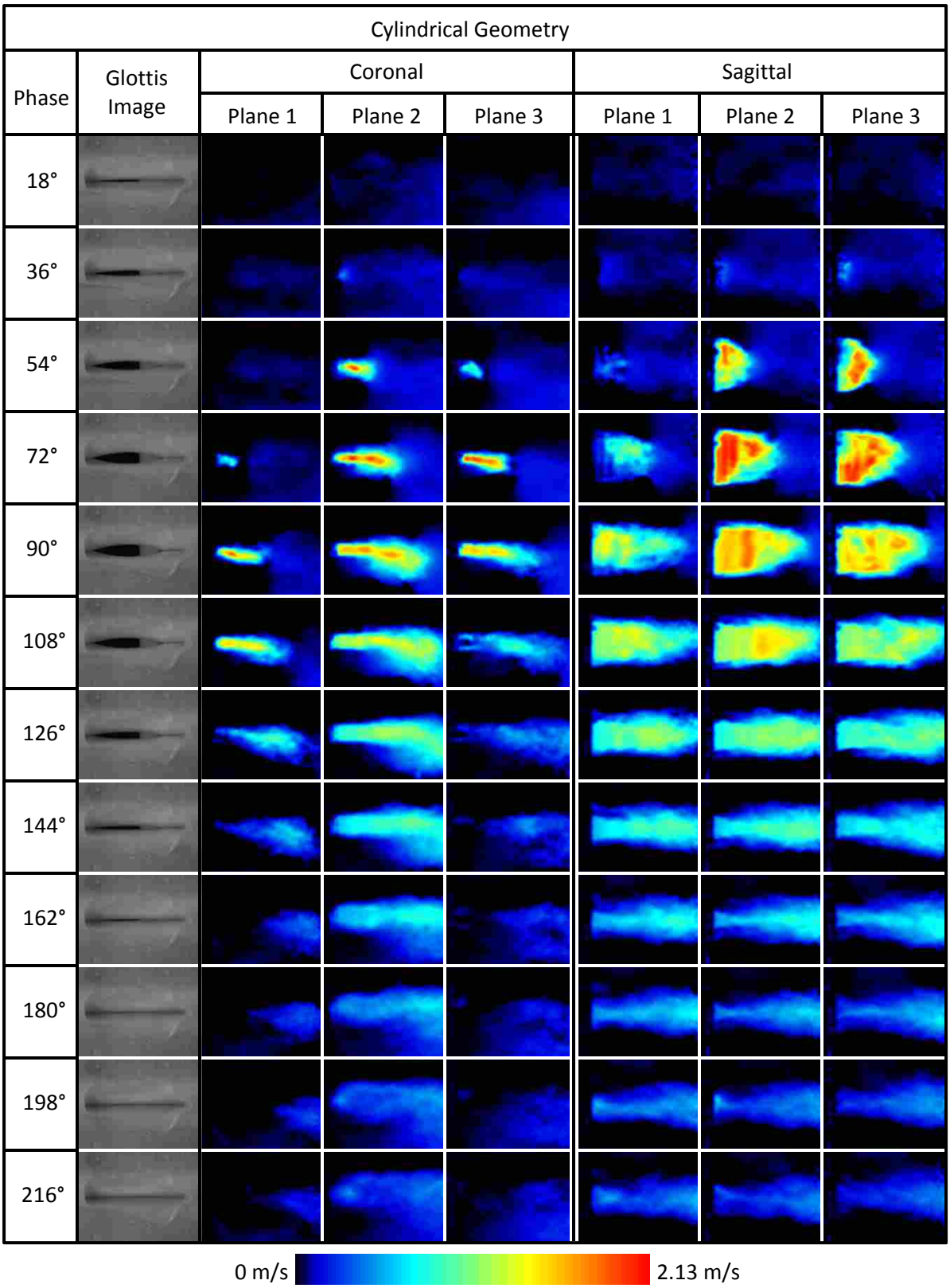

Figure 4-6. PIV data for cylindrical geometry in the (left) coronal planes, and (right) sagittal planes. Only certain phases are shown.

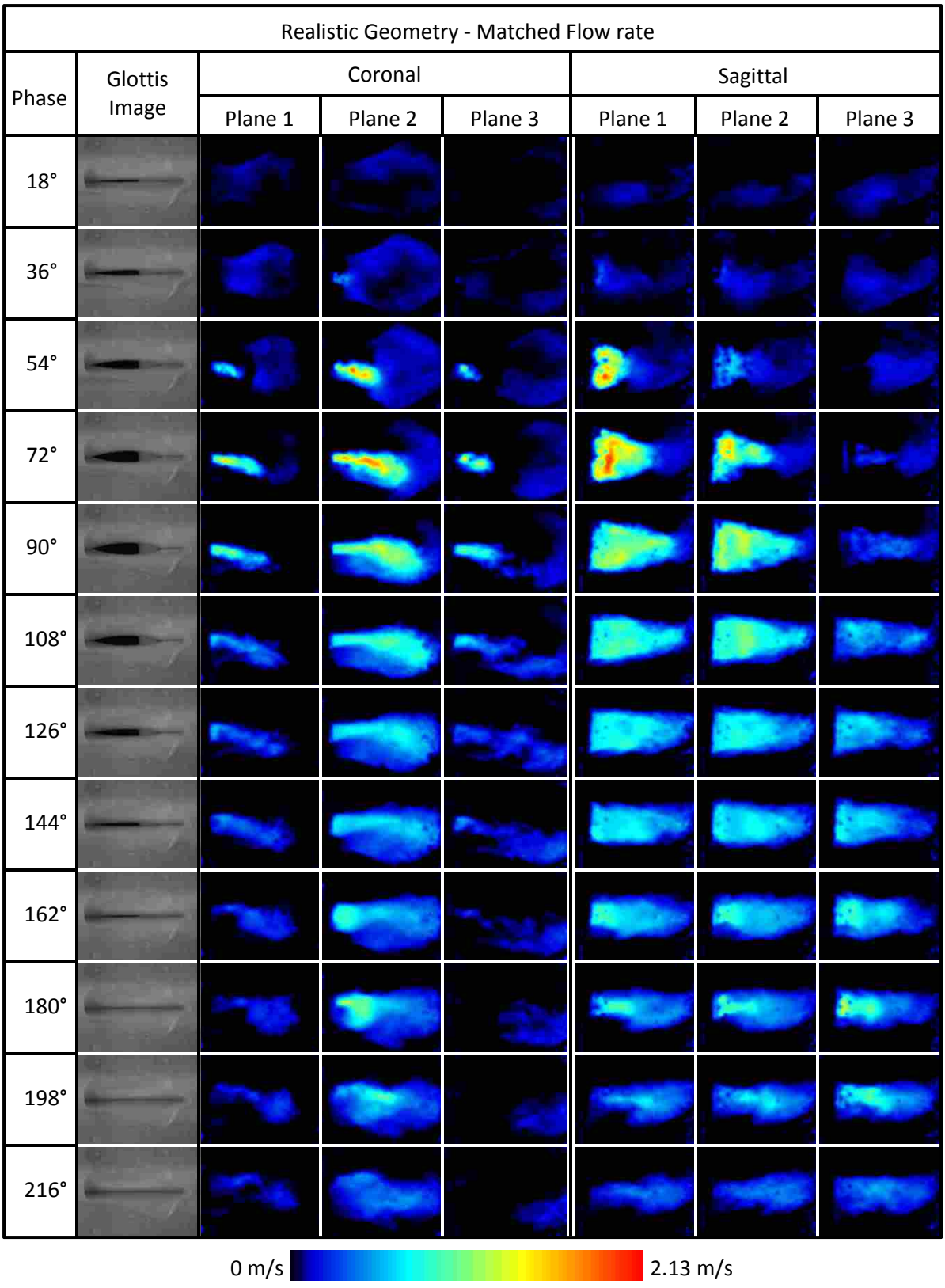

Figure 4-7. PIV data for realistic geometry - matched flow rate case in the (left) coronal and (right) sagittal planes.

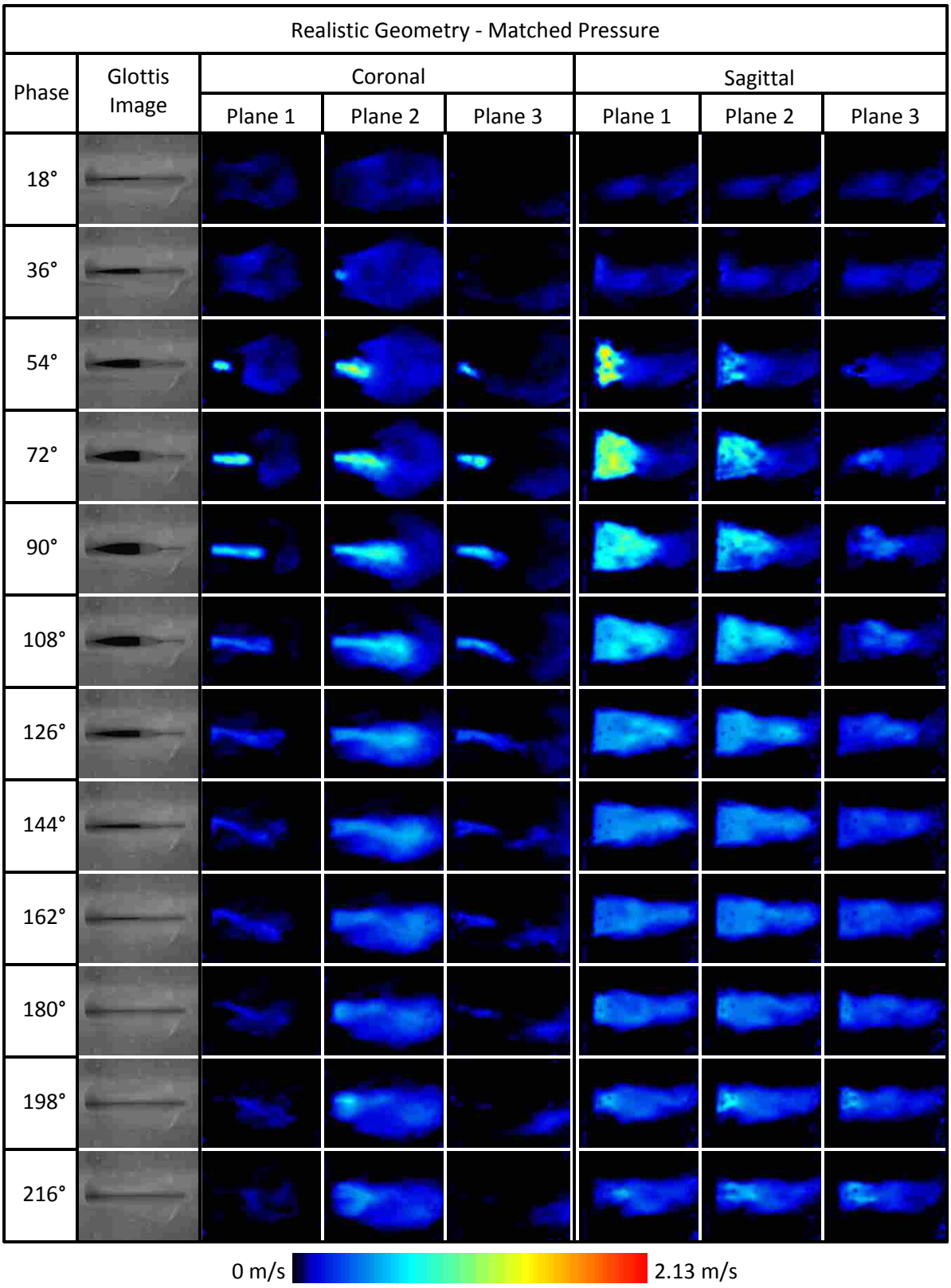

Figure 4-8. PIV data for realistic geometry - matched pressure case in the (left) coronal and (right) sagittal planes.

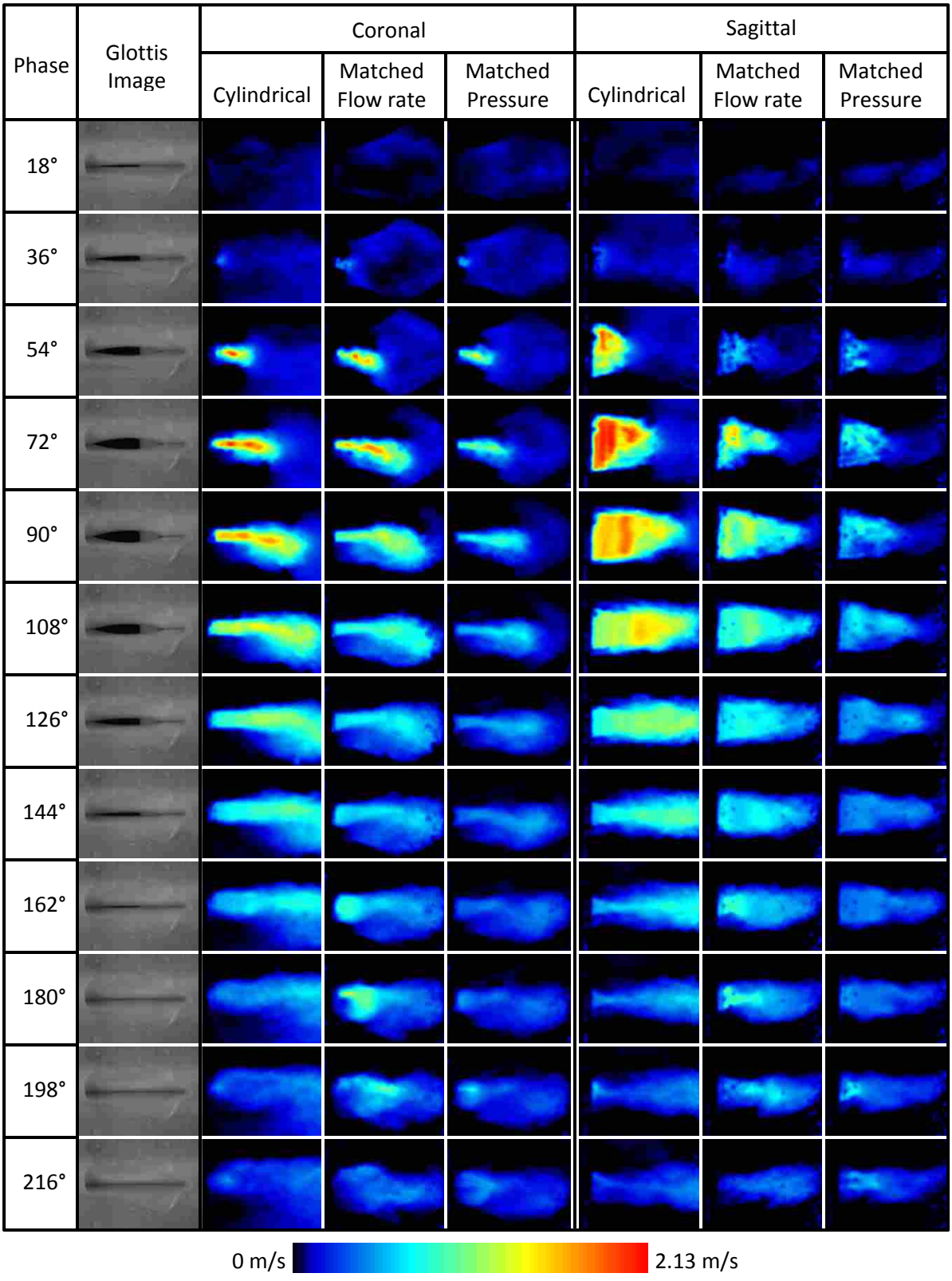

Figure 4-9. Comparison of PIV data for the midplane of each case in the coronal (left three PIV images) and sagittal (right three PIV images) planes.

4.4.2.2 Realistic Supraglottal Data (matched flow rate)

PIV data for the realistic supraglottal case with an average flow rate of 189 ml/s (equal to the cylindrical geometry) and an average transglottal pressure of 6.67 kPa are shown in Figure 4-7. For this case peak velocities also occurred at 72°. The maximum recorded velocity at 72° was 1.79 m/s, which was 84% of the maximum jet velocity recorded in the cylindrical geometry. In the coronal planes the supraglottal jet was strongest in the midplane, as was the case with the cylindrical geometry. The jet began to emerge at 36°, increased through 72°, and then decreased through 144°. At 162° through 198° there was a second small increase in velocity. This same secondary peak was also seen in the sagittal planes, especially in plane 3. In the sagittal planes peak velocities occurred in plane 1, rather than in plane 2 (midplane). This offset in the location of the peak velocities compared to the cylindrical geometry could be due to natural asymmetries in the supraglottal geometry. Figure 4-10 compares the profiles of the right and left supraglottal walls for the three coronal planes.

In the sagittal planes the supraglottal jet was slightly directed toward the right (bottom of the image) in 54° and 72°, suggesting occurrence of jet skewing during the opening glottal phases. Unlike other studies (Triep et al., 2005; Erath and Plesniak, 2010), little or no significant Coanda effect was observed in any of the cases. It is interesting to note in the coronal view in plane 1 that fluid motion began at 36°, before the jet began to emerge in this plane. Figure 4-11 highlights this event. At 18° there was no significant fluid motion. At 36° fluid motion appeared in the middle of the supraglottal opening, downstream of the ventricular folds. The supraglottal jet did not emerge until 54° in this plane. The presence of fluid motion at 36°, before the emergence of the jet in plane 1, suggests that the flow is highly three-dimensional. This same flow development occurred in the matched pressure case in the same phases. In the matched

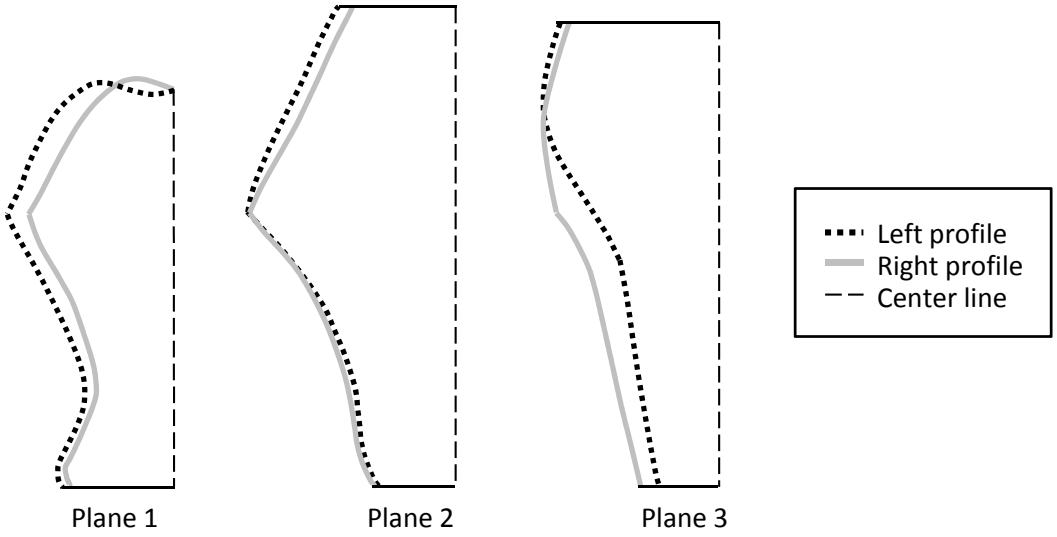

Figure 4-10. Comparison of the right and left profiles of the supraglottis in the three sagittal planes.

flow rate case the velocity increase between 18° and 36° was 3.79% of the maximum velocity in this plane. In the matched pressure case the velocity increase was 8.41%. In the cylindrical geometry the velocity essentially stayed the same (decreased by −0.02%). Thus this three-dimensional flow development only occurred in the realistic cases, suggesting that the realistic supraglottal geometry affects the three-dimensional geometry and spread of the jet.

4.4.2.3 Realistic Supraglottal Data (matched pressure)

PIV data for the realistic supraglottal case with an average transglottal pressure of 3.54 kPa (within 10% of that used in the cylindrical geometry) and an average flow rate of 142 ml/s are shown in Figure 4-8. For this case peak velocities occurred at 54°, one phase (18°) earlier than in the cylindrical and matched flow rate cases. The jet started to emerge at 36°, velocities peaked at 54°, and then the jet decreased through 162°. For this case a second spike in jet velocity was seen at 180° through 216°. In the coronal planes, peak velocities occurred in the

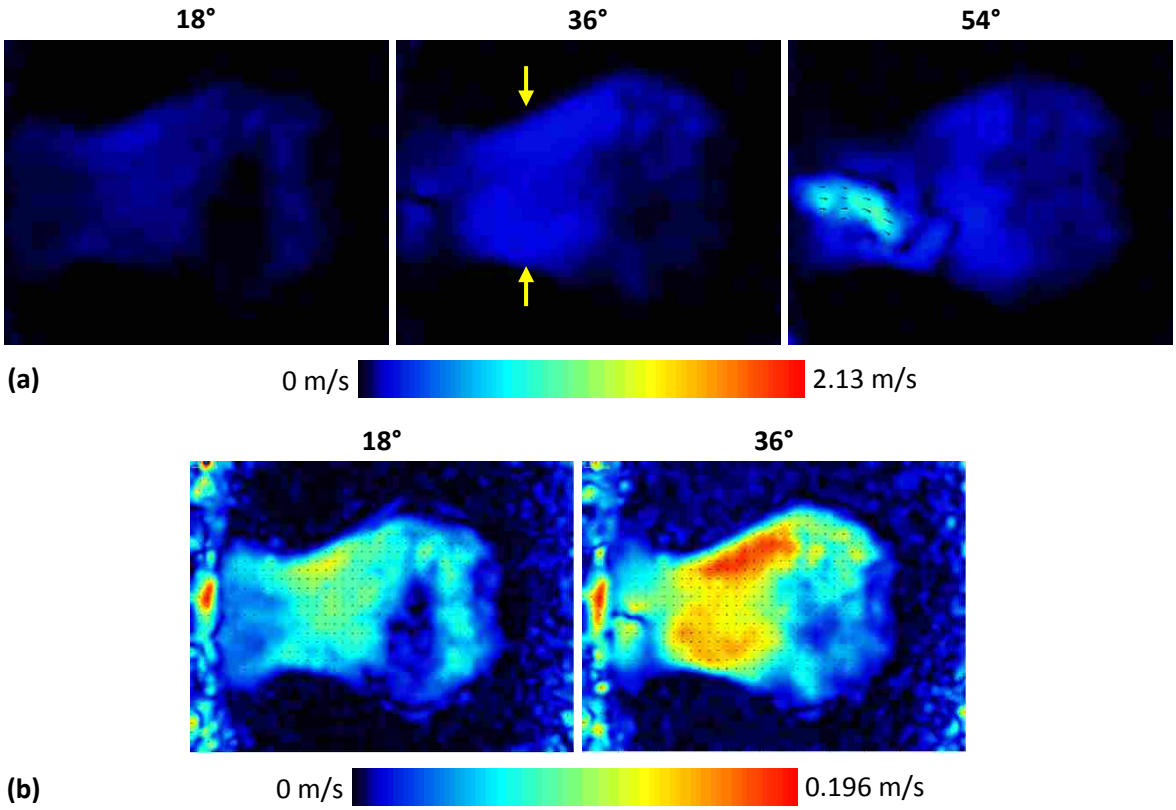

Figure 4-11. Matched flow rate case, coronal view, plane 1. (a) Fluid motion was seen at 36°, before the supraglottal jet emerged in this plane (54°). (b) 18° and 36° shown with a smaller velocity threshold to highlight the change in velocity between the two phases.

midplane, but in the sagittal planes peak velocities occurred in plane 1, similar to the matched flow rate case. A maximum velocity of 1.33 m/s was recorded at 54°, sagittal plane 1. This maximum velocity was only 63% of that of the maximum velocity recorded in the cylindrical geometry and 74% of the matched flow rate maximum velocity.

4.4.2.4 Comparisons for All Three Cases

Figure 4-9 compares the midplane PIV data for all three experimental cases. The jet shape in both the coronal and sagittal planes is similar for all three cases. The highest velocities occurred in the cylindrical geometry. The matched pressure case contained the lowest peak

velocities. As stated in Sections 4.4.2.2 and 4.4.2.3, the maximum velocity of the matched pressure geometry was 63% of the cylindrical geometry, and the maximum velocity of the matched flow rate geometry was 84% of that of the cylindrical geometry. Flow rate and pressure parameters for the cylindrical geometry were set to either the matched flow rate or matched pressure cases (refer to Table 4-1). Thus, while the experimental parameters were not significantly higher in the cylindrical geometry compared to the realistic cases, the jet velocity was notably higher. The difference between the supraglottal jet velocities of the realistic cases and those of the cylindrical geometries could be due to increased flow resistance in the realistic geometry. This would indicate that realistic flow resistance does quantitatively influence supraglottal flow and should be taken into account in experimental studies. Qualitatively the general shape of the velocity fields are similar in all cases.

A second spike in velocities occurred in both realistic cases, and to a lesser extent in the cylindrical geometry. This second spike in jet velocities appeared to be shifted backwards by 18° in the matched pressure case compared to the matched flow rate case, and backwards by 36° in the cylindrical case. It is possible that the secondary velocity peaks between the two realistic cases were less offset than they appeared because PIV data were only taken every 18°. It is not clear at this time what caused the secondary spike in velocity. It could possibly be due to elastic deformation of the glottal and/or supraglottal walls, rebounding of the glottal membranes, or to fluid momentum. Further investigation is needed to determine the cause.

The velocity vector field at 90° at the midplane of all three geometries is shown in Figure 4-12. The velocity fields for the cylindrical and matched flow rate cases were very similar. The shape of the velocity vector field in both the coronal and sagittal planes was very similar. The shape of the velocity field in the sagittal view of the matched pressure case was similar to the

velocity field shapes of the other two cases. The shape of the velocity field in the coronal view for this case was similar at the supraglottal entrance, but the jet did not develop in quite the same way as the cylindrical and matched flow rate cases. It is interesting to note that in all three cases in the coronal planes the jet drifted to the left (top of the image) during closing (see Figure 4-9, 90°-144°). In the realistic cases the jet appeared to attach to the left (top of the image) supraglottal wall. This drift was probably due to the realistic glottis and glottal exit not being completely symmetric. Drechsel and Thomson (2008) observed that in a self-oscillating model with offset ventricular folds the supraglottal jet skewed away from the near wall during opening, then straightened. However, after straightening the jet was then further skewed by near ventricular fold boundary. The behavior was attributed to additional fluid resistance caused by the near ventricular fold. A similar phenomenon could cause the more pronounced skewing of the jet in the realistic cases. Triep and Brücker (2010) also observed jet deflection during glottal open phases. In their study with ventricular folds the jet immediately attached to one of the ventricular folds upon glottal opening, and remained attached through maximum glottal opening. In this study the jet straightened toward the centerline before maximum glottal opening.

In contrast to the jet skewing observed in this study, Xue et al. (2014) observed no strong jet skewing in a realistic computational vocal tract model. No strong jet deflection was observed over the entire glottal cycle, except at the posterior end of the model during maximum glottal opening. At that point the jet was slightly deflected and attached to one of the ventricular folds. This behavior was similar to the behavior observed in the realistic cases during closing. However, jet deflection and wall attachment occurred near the center of the vocal tract, not just the posterior end. It is also interesting to note that Xue et al. observed a strong anterior-posterior asymmetry in glottal flow not observed in this study. This could be because the glottal gap in

their computational model was left-right symmetric, but had a strong asymmetry in glottal gap width in the anterior-posterior direction, whereas the glottal gap in this study was more symmetric in medial-lateral and anterior-posterior directions.

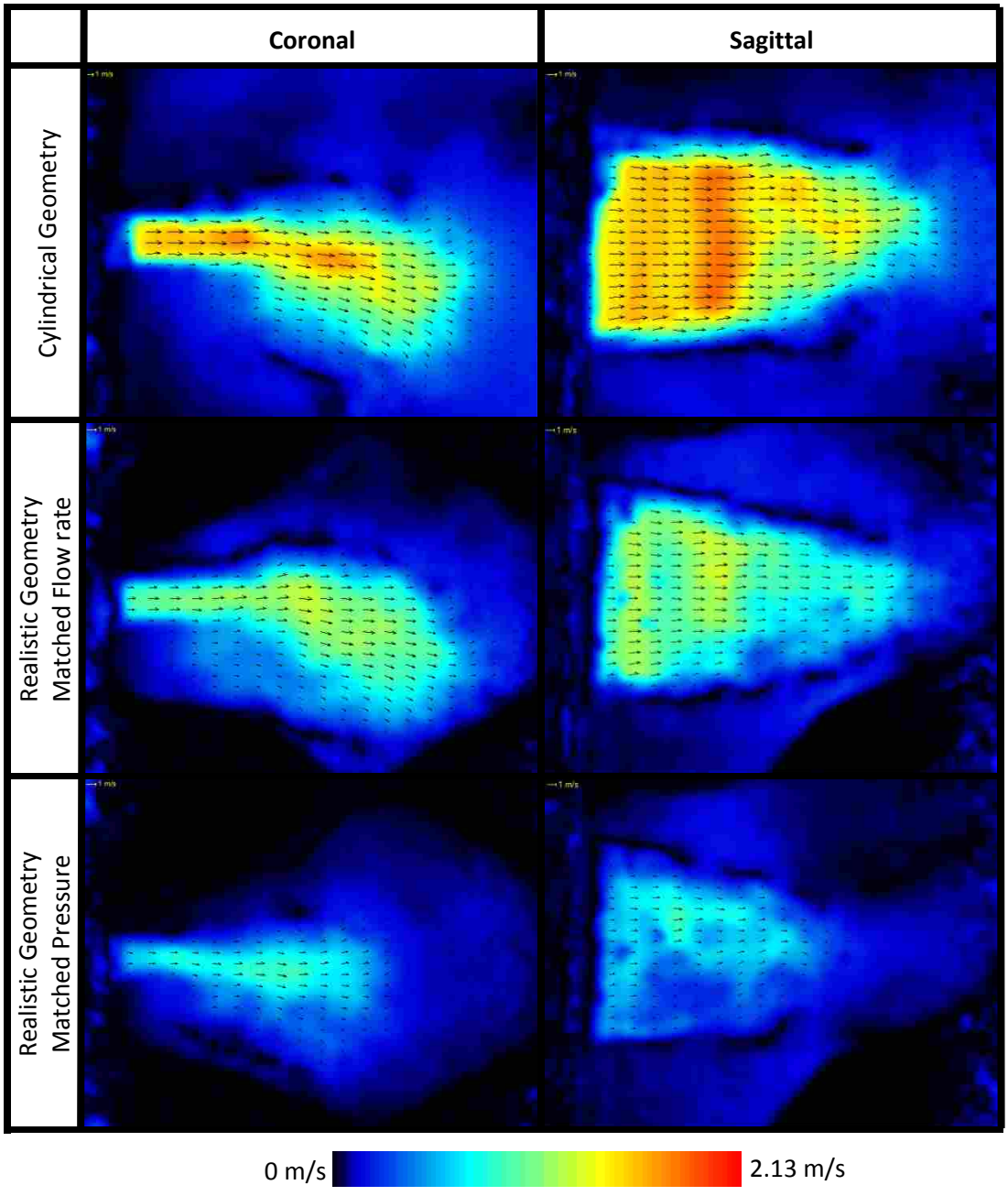

Figure 4-12. Comparison of the velocity vector fields for 90° of the midplane jet for all three experimental cases.

4.4.2.5 Vorticity

Vortical structures in the supraglottal jet developed during the opening phases of the glottis in all three experimental cases. Figure 4-13 compares vortices using velocity contours in the coronal view for the matched flow rate and cylindrical cases. Since the matched pressure vortices were similar to the matched flow rate vortices, they are not shown in detail. For the realistic – matched flow rate case vortices developed to the left and right (top and bottom of the image, respectively) of the supraglottal jet in 36°. Vortices developed somewhat later in the cylindrical geometry and were not seen until 54°. These vortices grew and traveled downstream as the jet continued to develop. Similar starting vortices were noted by Khosla et al. (2007) and Drechsel and Thomson (2008) during the early opening phases of the glottis. Figure 4-14 compares the starting vortices in the coronal view using vorticity contours. Note that starting vortices are nearly ideal vortices with the vorticity close to zero. These starting vortices are evident in the velocity contours during opening. However, in the vorticity contours the vorticity is the shear layer is much stronger than the strength of the starting vortices, making them less visible. The vorticity plots in Figure 4-14 also reveal vortex shedding during late opening phases of the glottis. Vortices also developed in the sagittal view in all three cases and were first seen in 54° (see Figure 4-15 and 4-16). The vortices in the cylindrical geometry were smaller and traveled downstream slower than those in the matched flow rate case.

Vortices also formed in the closing phases of the glottis in the realistic – matched flow rate and matched pressure cases. Vortical structures were similar in the matched flow rate and matched pressure cases, though the vortices were stronger in the matched flow rate case. Thus only vortices for the matched flow rate case are shown. Figure 4-17 shows the vortices formed in the coronal midplane. The vortex traveled slightly downstream between 162° and 180°.

Vortices formed to the right (bottom of the image) of the supraglottal jet. Vortices in the sagittal view formed earlier (144°) during closing than in the coronal view. Vortices formed on both sides of the supraglottal jet and traveled downstream as the vocal folds closed (see Figure 4-18). In the study reported by Triep et al. (2005), large recirculation zones downstream of the ventricular folds formed in the coronal planes during late closing. These large recirculation zones were not evident in this study, possibly due to the non-uniform vocal tract geometry. The narrowing of the vocal tract downstream of the ventricular folds may have limited the development of these large scale recirculation zones.

Vorticity plots revealed Kelvin-Helmholtz vortices during closing in both realistic and cylindrical cases. Kelvin-Helmholtz vortices, seen on both sides of the jet edge, were produced by strong shear stresses caused by the rapid decline of velocity magnitudes at the jet edge. Figure 4-19 shows the Kelvin-Helmholtz vortices as the glottis closed. Similar vortices during closing phases of the glottis were also observed by Kucinschi et al. (2006), Khosla et al. (2007), and Triep and Brücker (2010). Just before closing (162°) vortices formed on the both sides of the jet. Figure 4-20 shows that as the glottis closed (180°) these vortices grew in strength and convected downstream during subsequent closed phases. No such vortices were seen in the cylindrical case.

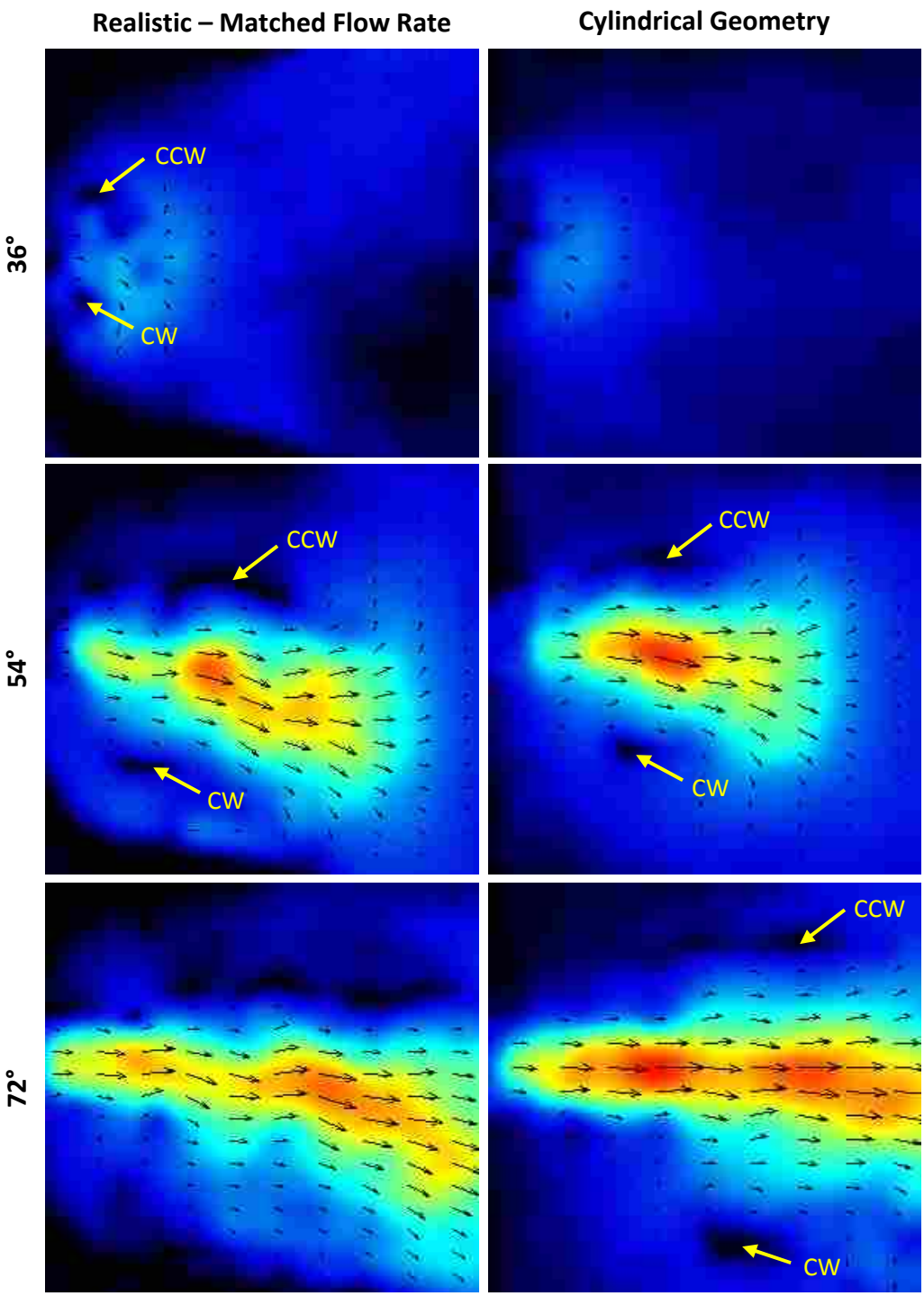

Figure 4-13. Coronal view (plane 2) of vortical structures that developed during the opening phases of the glottis. The velocity contours are shown here. Velocity contour scale corresponds to the color scale given in Figure 4-12.

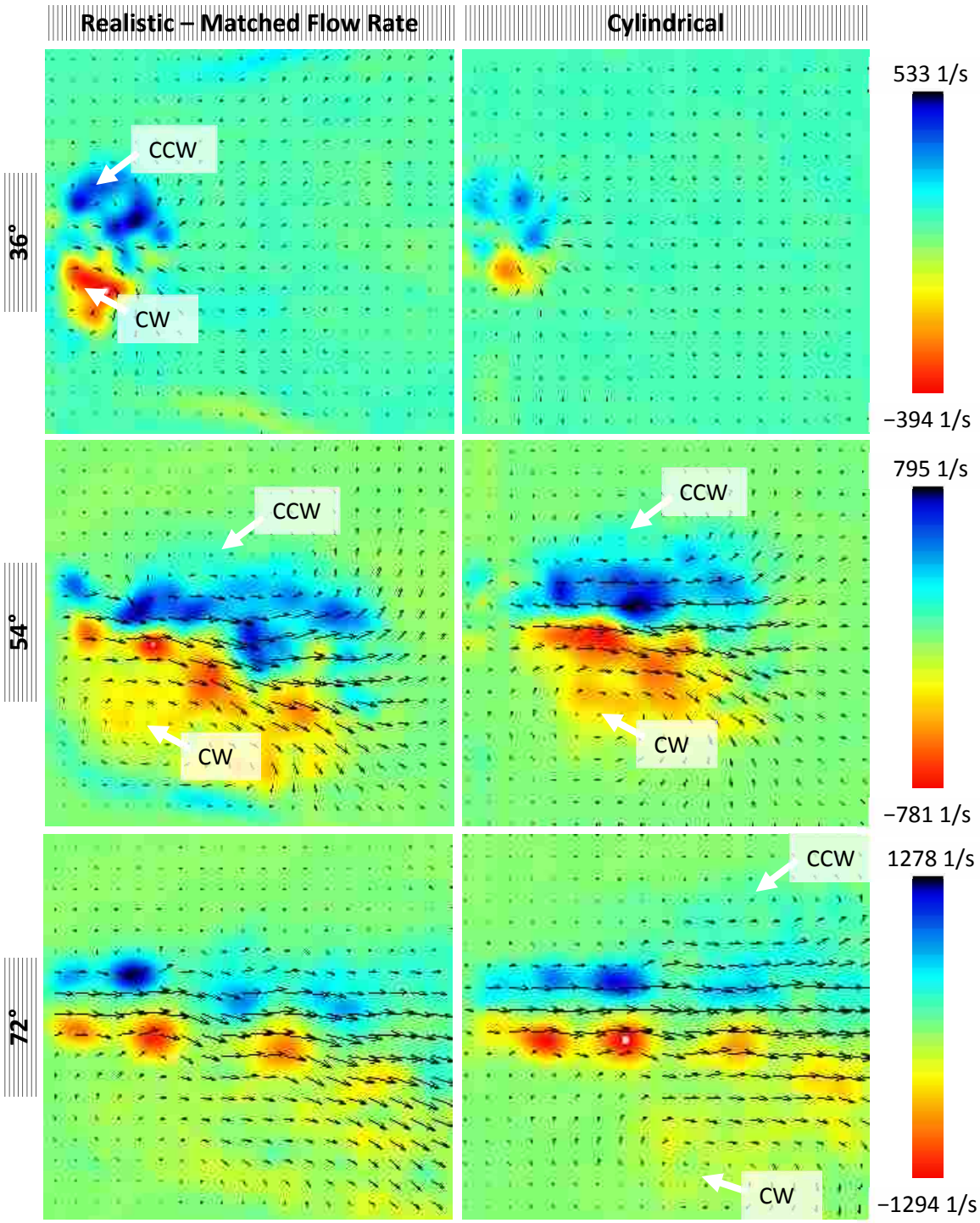

Figure 4-14. Coronal view (plane 2) of vorticity plots during the late opening phases of the glottis.

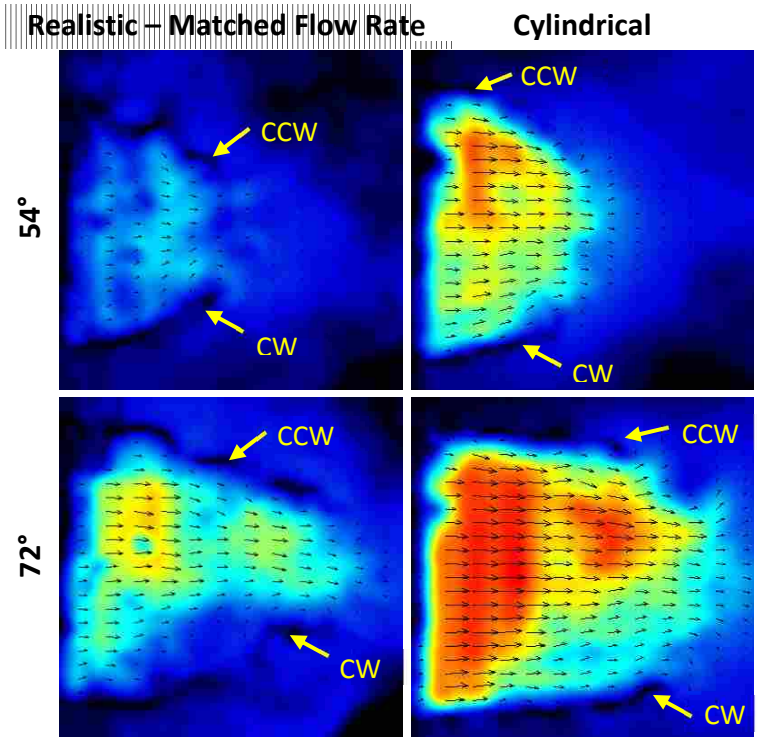

Figure 4-15. Sagittal view (plane 2) of vortical structures that developed during the opening phases of the glottis. Velocity contour scale corresponds to the color scale given in Figure 4-12.

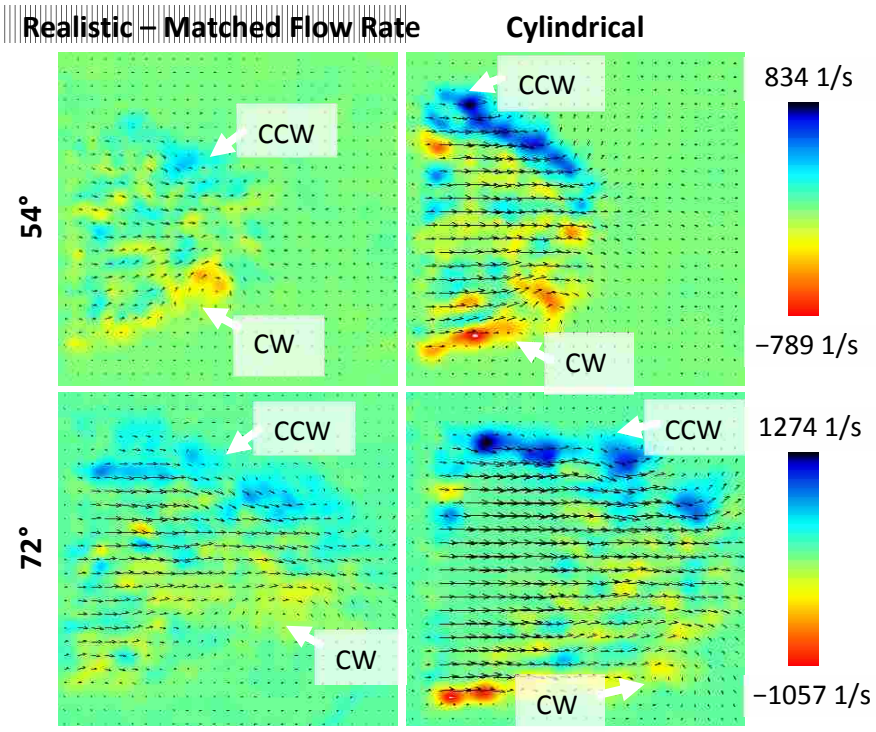

Figure 4-16. Sagittal view (plane 2) of vorticity plots during the late opening phases of the glottis.

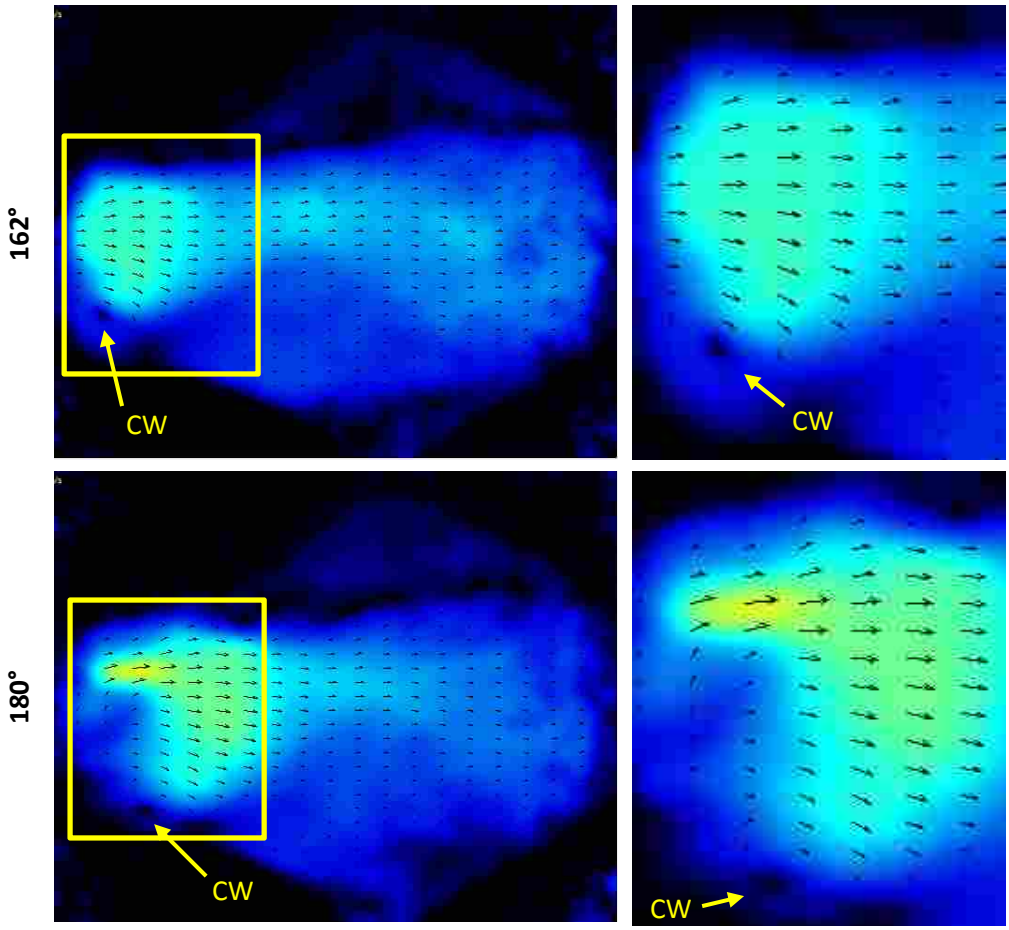

Figure 4-17. (Left) Coronal view of vortices formed during the closing phases of the glottis for the matched flow rate case. (Right) Enlargement of the boxed region in the images on the left. Velocity contour scale corresponds to the color scale given in Figure 4-12.

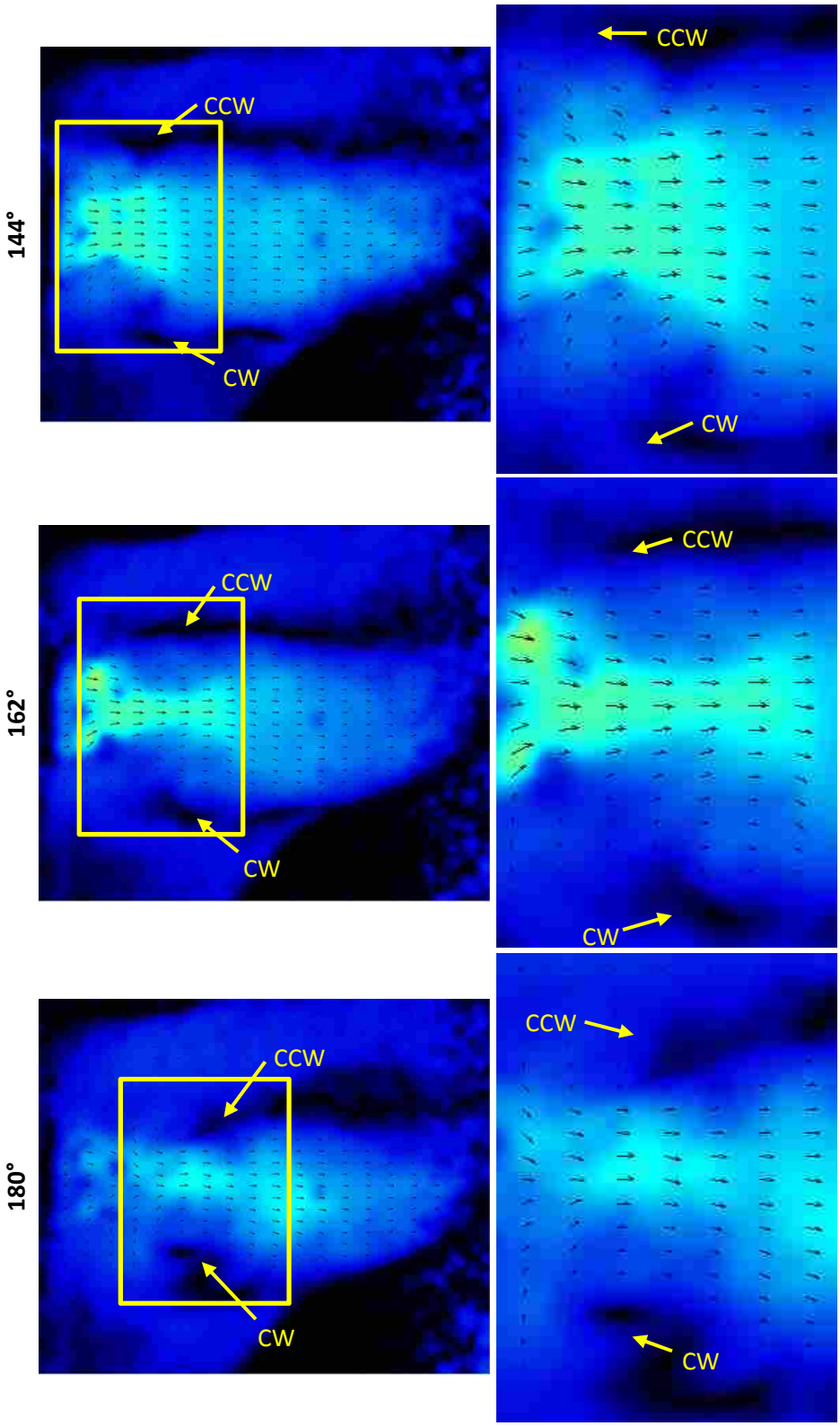

Figure 4-18. (Left) Sagittal view of vortices formed during the closing phases of the glottis for the matched flow rate case. (Right) Enlargement of the boxed region in the images on the left. Velocity contour scale corresponds to the color scale given in Figure 4-12.

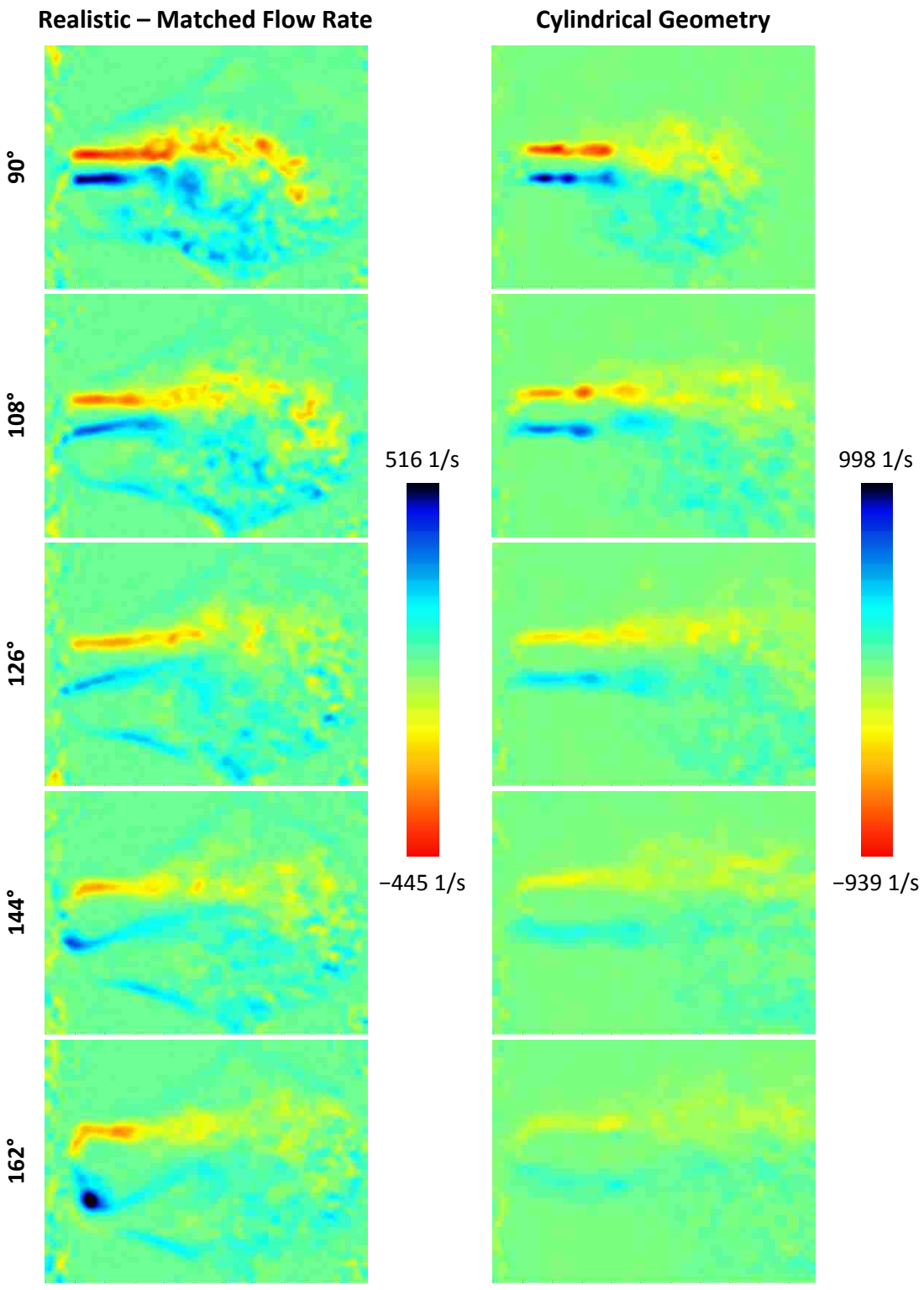

Figure 4-19. Coronal view of Kelvin-Helmholtz vortices formed during the closing phases of the glottis for the matched flow rate and cylindrical cases.

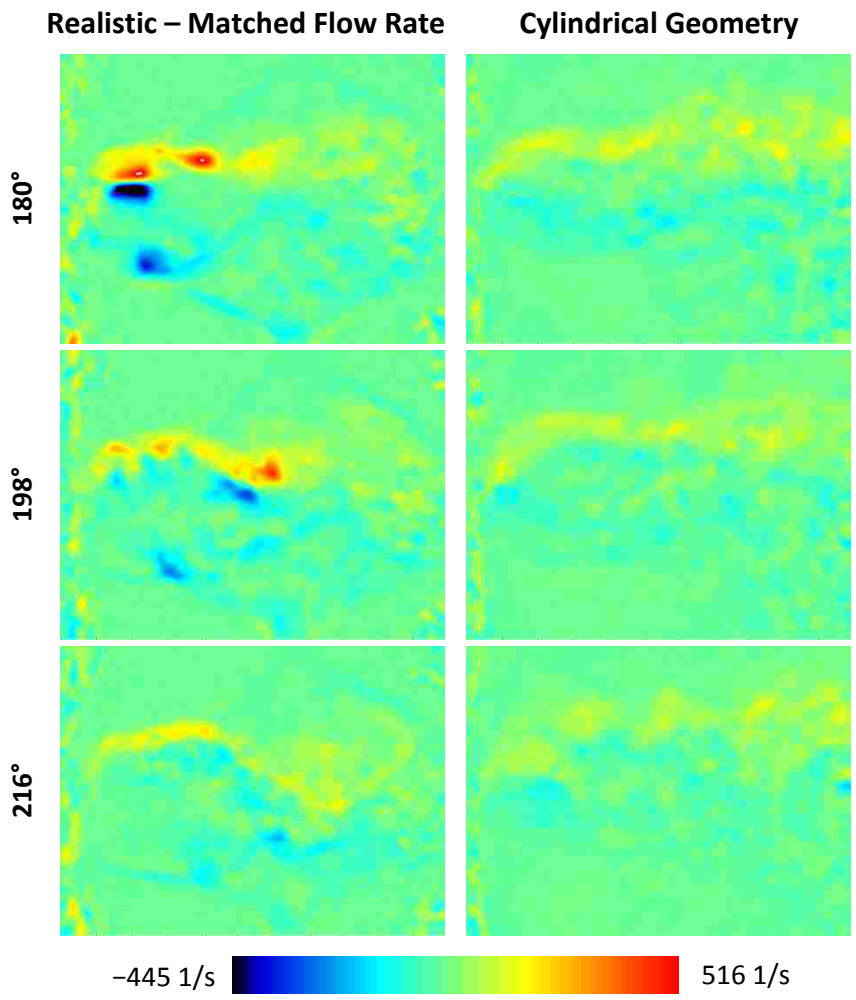

Figure 4-20. Coronal view of vortices convected downstream during the closing phases of the glottis for the matched flow rate and cylindrical cases.

4.4.2.6 Axis Switching

Axis switching occurred in all three cases. Figure 4-21 compares the sagittal and coronal jet shapes for all three cases for 90°. Outlines of the jet widths were made by thresholding the minimum velocity of the PIV data to 30% of the maximum velocity for each case and plane. The jet width decreased in the sagittal planes while it simultaneously increased in the coronal planes. Eventually the jet width in the sagittal planes surpassed the jet width in the coronal

planes. The occurrence of axis switching of the supraglottal jet is consistent with observations made by Krebs et al. (2011), Kirmse et al. (2010), and Triep and Brücker (2010) in uniform vocal tracts, and has now been shown to occur in a realistic vocal tract.

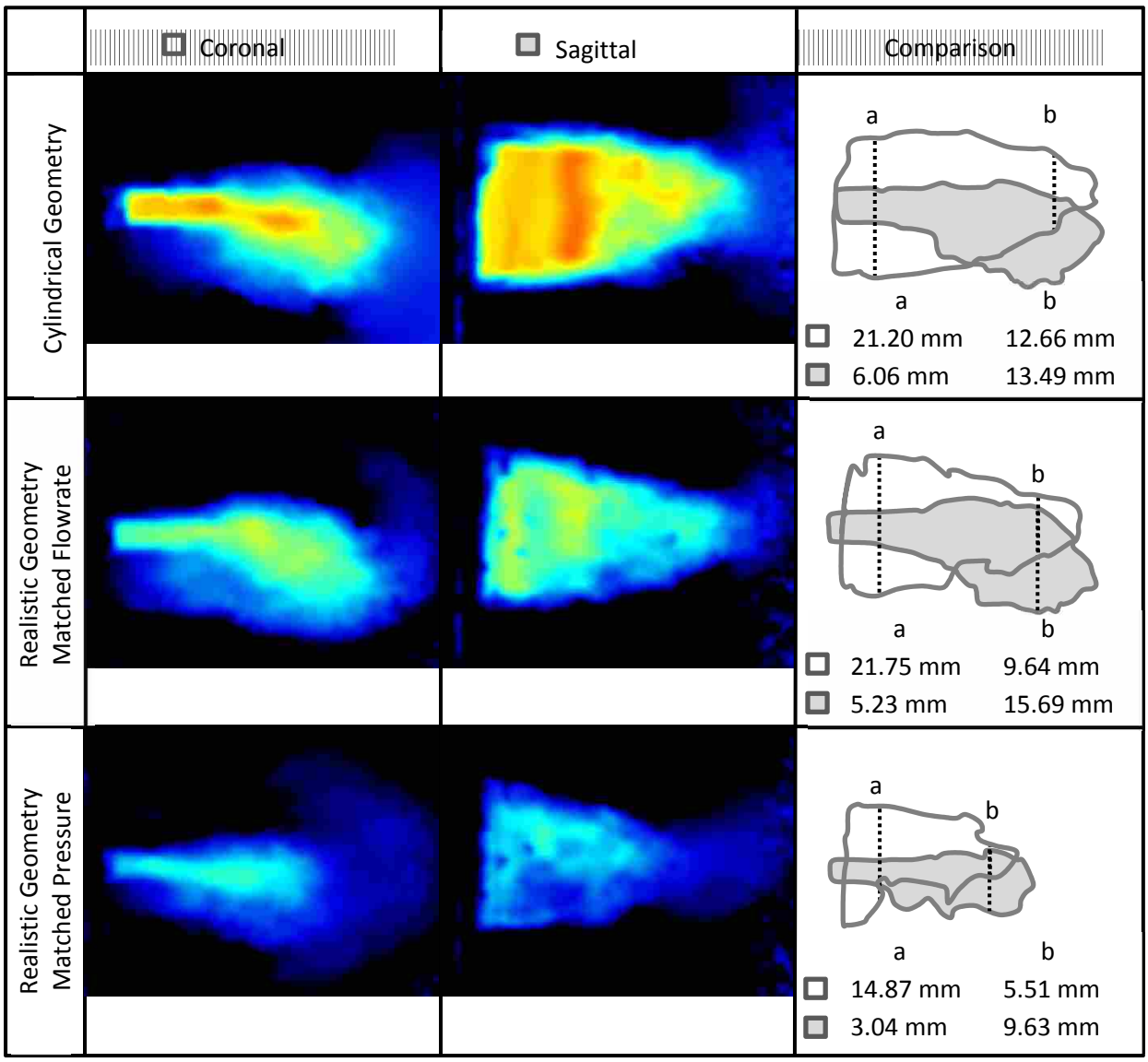

Figure 4-21. Comparison of midplane jet width for cylindrical, matched flow rate, and matched pressure cases for 90°. An outline of the sagittal view is shown in grey; the coronal view is shown in white. a and b denote locations of jet width comparison, with the measurements given below outlines for each case. Velocity contour scale corresponds to the color scale given in Figure 4-12.

4.5 Uncertainty Analysis of PIV Measurements

Velocity uncertainty was determined by the ability of the equipment to accurately measure particle movement, the degree to which the particles follow the motion of the flow, and the accuracy with which the software correlates particle groupings. PIV uncertainty was calculated according to the method set forth by Lazar et al. (2010) and performed by Naegle (2012). The MATLAB code used to calculate the uncertainty at each position of the flow field is given in Appendix A. Additional details on uncertainty calculations are given in Appendix B.

The error due to equipment uncertainty was estimated by:

$$w_u = \sqrt{u^2\left[\left(\frac{1}{L}w_l\right)^2 + \left(\frac{-l}{L^2}w_{L1}\right)^2 + \left(\frac{-l}{L^2}w_{L2}\right)^2\right] + \left(\frac{-u}{\Delta t}\frac{l}{L}\right)^2 [w_{t1} + w_{t2}]}, \quad (4.1)$$

where u was the velocity, l was the length of the calibration scale for each case and plane, L was the length (in pixels) of the calibration scale on the image, w_l was the uncertainty of the calibration scale length measurement, w_{L1} was the uncertainty of the image plane length, w_{L2} was the image distortion due to lens aberrations, Δt was the time step of the image pair, w_{t1} was the uncertainty of the laser pulse timing, and w_{t2} was the accuracy of the delay generator.

Uncertainty due to inertial effects determines how well the seeding particles followed the flow. Inertial uncertainty is also known as the slip velocity, and was calculated as follows:

$$u_{slip} = \frac{1}{18}\frac{\rho_p d_p^2}{\mu_f}\left(a_{px}u_{px} + a_{py}u_{py}\right), \quad (4.2)$$

where u_{slip} was the difference between the fluid and particle velocities, ρ_p was the particle density, d_p was the average particle diameter, μ_f was the fluid viscosity, a_{px} and a_{py} were the accelerations of the particle in the *x*- and *y*-directions, and u_{px} and u_{py} were the particle velocities in the *x*- and *y*-directions.

Process uncertainty refers to the accuracy with which the software was able to correlate particle groupings. Process uncertainty was estimated by calculating the error that would occur if the correlation procedure incorrectly matched the particle groupings. With a final window size of 16×16, the correlation can be off up to 16 pixels. However, post-processing algorithms removed vectors if its difference to the average of the neighboring vectors was more than twice the root-mean-square value of its neighbors, thus reducing the effects of poor correlation. This post-processing method caused the process uncertainty to scale with the velocity gradients in the fluid rather than the local velocity in the fluid. The process uncertainty for each point in the flow field was calculated as follows:

$$w_p = \sqrt{\left(u_x - 2u_{x(rms)}\right)^2 + \left(u_y - 2u_{y(rms)}\right)^2}, \tag{4.3}$$

The total uncertainty for each location in the velocity measurements was calculated by combining the individual sources of uncertainty as follows:

$$w_{total} = \sqrt{w_u^2 + u_{slip}^2 + w_p^2}, \tag{4.4}$$

For the open phases containing the glottal jet, the regions of highest uncertainty correlated with the regions of highest velocity. For the phases not containing the glottal jet, uncertainty still mostly correlated with velocity with high uncertainty regions also occurring in regions with few seeding particles. Uncertainty values in phases not containing a jet were significantly lower than phases containing the jet. A total maximum uncertainty of ±0.0469 m/s occurred in coronal plane 3 of the cylindrical case and corresponded to 2.4% of the local velocity value. All other uncertainty values were lower than this value, and maximum total uncertainty values are given in Table 4-3.

Table 4-3. Maximum total uncertainty (w_{total}) and percent uncertainty of local velocity values for each case.

		Cylindrical		Matched Flow Rate		Matched Pressure	
	Plane	w_{total} (m/s)	% Uncertainty	w_{total} (m/s)	% Uncertainty	w_{total} (m/s)	% Uncertainty
Coronal	1	0.0309	1.66	0.0177	1.14	0.0117	1.12
	2	0.0303	1.53	0.0235	1.30	0.0191	1.41
	3	0.0469	2.40	0.0165	1.14	0.0188	1.86
Sagittal	1	0.0179	1.23	0.0221	1.14	0.0166	1.13
	2	0.024	1.14	0.0182	1.18	0.0121	1.27
	3	0.0242	1.20	0.0148	1.13	0.0098	2.42

4.6 Conclusions

The modular construction of the model used in this study allowed for data collection in both realistic and cylindrical vocal tracts. PIV and transglottal pressure data were collected in a realistic vocal tract with mechanically-driven vocal folds. Comparisons were made to PIV and transglottal pressure data collected in a uniform (cylindrical) vocal tract. The objective of this

study was to characterize laryngeal flow structures in a realistic vocal tract, and to determine the effect of realistic supraglottal geometry on glottal flow. The experiments revealed the following:

(a) Maximum transglottal pressure occurred during the opening phases of the glottis for all three cases. It is unclear why this happened, but may have been due to fluid inertia. The minimum transglottal pressure occurred after the maximum glottal opening.

(b) The highest supraglottal jet velocities were observed in the cylindrical geometry. Higher flow resistance in the realistic supraglottal vocal tract may have caused lower velocities in the realistic cases.

(c) A secondary spike in velocity occurred in both realistic cases, and to a lesser extent in the cylindrical case during and after glottal closure. It is not clear what caused this, but possible causes are elastic deformation of the glottal and/or supraglottal walls, rebounding of the glottal membranes, or fluid momentum. Further investigation is needed with more phases to better resolve the phenomena.

(d) Jet deflection occurred in all three experimental cases, but was more pronounced in the realistic cases. The jet deflected to one side during glottal opening, straightened, and deflected to the other side during closing, similar to other studies with uniform vocal tracts.

(e) Starting vortices, Kelvin-Helmholtz vortices, and closing vortices were observed similar to what has been seen in other voice research studies. Starting vortices formed in earlier glottal opening phases in the realistic cases compared to the cylindrical case and were stronger. In the realistic cases vortices formed just before glottal closing, but not in the cylindrical case, suggesting that realistic supraglottal geometry influences vortex development.

(f) Jet axis switching was evident in both realistic and cylindrical cases, consistent with other studies. This suggests that axis switching is a real phenomenon that occurs during voice production.

The results from this study hold for the given conditions in this model. It is concluded that realistic supraglottal geometry does affect supraglottal flow and should be included in future studies. Future investigations are needed to further characterize the role realistic flow resistance plays in vocal fold vibration and voice production.

5 CONCLUSIONS

The research described in this thesis has been conducted to further the understanding of voice production by characterizing laryngeal flow in realistic vocal tract geometries. This was accomplished by developing a method to collect particle image velocimetry (PIV) data within complex realistic geometries, creating realistic synthetic laryngeal models that were mechanically-driven, creating a uniform supraglottal geometry for comparison, and using PIV to investigate the flow features within a realistic vocal tract for an increased understanding of the flow features present during voice production.

5.1 Acquisition of Detailed Glottal Flow Measurements in Geometrically Realistic Models

5.1.1 Conclusions

A method for acquiring detailed glottal flow measurements using PIV in a geometrically realistic model of the laryngeal airway was developed and demonstrated. The method included using computed tomography (CT) scan data to create a synthetic static laryngeal model produced from clear silicone. A mixture of glycerol and water was used as the working fluid to match the index of refraction of the silicone, and allowed for the acquisition of whole-field velocity data in complex model geometries. Velocity fields in sagittal and frontal planes were shown, and vortical structures in the ventricles were noted. The flow was clearly three-dimensional.

5.1.2 Future Work

The method described in Chapter 2 is anticipated to find use in subsequent studies characterizing the three-dimensional velocity field, including vortical patterns and turbulence levels, found in the human larynx. The model used in this study was static and was not able to yield information about the effect of vibrating vocal folds on the flow field. Further insight could be gained by instead using a driven model. The development and use of a similar model with dynamically-driven vocal folds is the subject of Chapters 3 and 4. Future studies could use three-dimensional PIV to further characterize the three-dimensional flow.

5.2 Driven Vocal Fold Model Design

5.2.1 Conclusions

A realistic synthetic model of the vocal tract was constructed to study three-dimensional laryngeal airflow. Subglottal, glottal, and supraglottal geometries were obtained from CT scan data. Pharyngeal geometry was based on previously published area function data. A cylindrical supraglottal geometry was also created. Pressure tap locations were included in the subglottal and supraglottal sections for transglottal pressure measurements. The model was primarily made of clear silicone and scaled to four times human size. The vocal folds were mechanically-driven. The working fluid consisted of a glycerol-water mixture whose index of refraction matched that of the silicone, allowing PIV data collection.

5.2.2 Future Work

This model was created for two-dimensional PIV data collection in the coronal and sagittal directions, with three-dimensional SAPIV data collection possible. Future models could

alter the design of the supraglottal (pharyngeal) outlet to also allow for transverse two-dimensional data collection.

The model was created with the potential to be used for a variety of laryngeal studies. The glottal cams can be removed and replaced with different geometries and different open quotients. The laryngeal geometry is modular so that different subglottal or supraglottal geometries could be investigated. The vocal folds can be driven at different frequencies, both in phase and out of phase, allowing different voice frequencies and pathologies to be studied.

5.3 Characterization of the Supraglottal Jet in a Complex Larynx Model

5.3.1 Conclusions

PIV and transglottal pressure data were collected in realistic and cylindrical vocal tracts with mechanically-driven vocal folds. The objective of this study was to characterize laryngeal flow structures in a realistic vocal tract and to determine the effect realistic supraglottal geometry has on glottal flow. Observed flow structures included axis switching, jet deflection, starting vortices, Kelvin-Helmholtz vortices, and closing vortices consistent with previous research. The experiment revealed lower jet velocities found in the realistic supraglottis than in the cylindrical supraglottis, as well as highly three-dimensional flow in the realistic vocal tract. The results of this study suggest that realistic supraglottal geometry does affect supraglottal flow and should be included in future studies.

5.3.2 Future Work

This study was conducted using a given set of flow rates and transglottal pressures. It would be interesting to study a greater range of flow rates and transglottal pressures and

document associated flow changes. Gauge pressure, rather than differential pressure, could be measured in the subglottis and supraglottis to correlate changes in supraglottal pressure during glottal phases, and to compare velocities in the supraglottal jet with supraglottal pressure. Cam shape could be varied to compare the glottal jet emanating from different glottal openings. Likewise the open quotient of the glottis could be varied. Many people suffer from vocal fold paralysis in which one vocal fold is partially or completely paralyzed. The glottal jet could be studied when only one vocal fold is in motion, or when one vocal fold rotation is out of phase with respect to the other.

Because the model is modular, future work could also include studies on the effects of subglottal geometry on the supraglottal jet. One study could compare the supraglottal jet produced from a uniform subglottis and from a realistic subglottis. Another study could compare the effects of subglottis geometries with varying degrees of subglottic stenosis on the supraglottal jet. A subglottis with a 90% subglottic obstruction has already been manufactured for future study (see Section 3.2.2).

REFERENCES

Alipour, F. and Scherer, R. C. (2002). "Pressure and velocity profiles in a static mechanical hemilarynx model," J. Acoust. Soc. Am. 112:2996-3003.

Alipour, F. and Scherer, R. C. (2006). "Characterizing glottal jet turbulence," J. Acoust. Soc. Am. 119:1063-1073.

Alipour, F., Scherer, R. C., and Knowles, J. (2006). "Velocity distributions in glottal models," J. Voice 10:50-58.

Baken, R. J. and Orlikoff, R. F. *Clinical Measurement of Speech and Voice*, 2nd edn, (Singular Publishing, 2000).

Bakhshaee, H., Moro, C., Kost, K., Mongeau, L. (2013). "Three-dimensional reconstruction of human vocal folds and standard laryngeal cartilages using computed tomography scan data," J. of Voice 27:769-777.

Becker, S., Kniesburges, S., Muller, S., Delgado, A., Link, G., Kaltenbacher, M., and Dollinger, M. (2009). "Flow-structure-acoustic interaction in a human voice model," J. Acoust. Soc. Am. 125:1351-1361.

Blair, G. P. and Cahoon, M. (2006). "Special Investigation: Design of an Intake Bellmouth," Race Engine Technology, Published Sept. 2006, pg. 35-41.

Brücker, C., Triep, M., and Kob, M. (2004). "Study of the vortex dynamics in a mechanical model of the vocal folds using particle-image velocimetry," In *Proceedings of the International Conference on Voice Physiology and Biomechanics* (Marseille, France, 2004), pg. 11-17.

Cheng, N. S. (2008). "Formula for the viscosity of a glycerol-water mixture," Ind. Eng. Chem. Res. 47:3285-3288.

Döllinger, M. and Berry, D. (2006). "Visualization and quantification of the medial surface dynamics of an excised human vocal fold during phonation," J. of Voice 20:401-413.

Doory, D., Taylor, D. J., Franke, P., and Schroter, R. C. (2008). "Experimental investigation of nasal airflow," J. Eng. in Med. 222:439-453.

Drechsel, J. S. and Thomson, S. L. (2008). "Influence of supraglottal structures on the glottal jet exiting a two-layer synthetic, self-oscillating vocal fold model," J. Acoust. Soc. Am. 123:4434-4445.

Erath, B., and Plesniak, M. (2010). "An investigation of asymmetric flow features in a scaled-up driven model of the human vocal folds," Exp. Fluids 49:131-146.

Farley, J., and Thomson, S. L. (2011). "Acquisition of detailed laryngeal flow measurements in geometrically realistic models," J. Acoust. Soc. Am. 103:EL82-EL86.

Grisel, J., Khosla, S., Murugappan, S., Lakhamraju, R., Aubry, J., Gutmark, E., and Huntress, G. (2010). "How does the absence or presence of subglottal medialization affect glottal airflow?" Ann. Oto. Rhinol. Laryn. 119:559-566.

Hofmans, G. C. J., Groot, G., Ranucci, M., Graziani, G., and Hirschberg, A. (2003). "Unsteady flow through *in-vitro* models of the glottis," J. Acoust. Soc. Am. 113:1658-1675.

Hopkins, L. M., Kelly, J. T., Wexler, A. S., and Prasad, A. K. (2000). "Particle image velocimetry measurements in complex geometries," Exp. Fluids 29:91-95.

Khosla, S., Murugappan, S., Gutmark, E., and Scherer, R. (2007). "Vortical flow during phonation in an excised canine larynx model," Ann. Oto. Rhinol. Laryn. 116:217-228.

Kim, J., Yoon, J., Kim, C., Nam, T., Shim, D., and Shin, H. (2006). "Particle image velocimetry measurements for the study of nasal airflow," Acta Oto-Laryngol. 126:282-287.

Kim, S. K. and Chung, S. K. (2004). "An investigation on airflow in disordered nasal cavity and its corrected models by tomographic PIV," Meas. Sci. Technol. 15:1090-1096.

Kirmse, C., Triep, M., Brucker, C., Dollinger, M., and Stingl, M. (2010). "Experimental flow study of modeled regular and irregular glottal closure types," Logop. Phoniatr. Voco. 35:45-50.

Kob, M., Krämer, S., Prévot, A., Triep, M., and Brücker, C. (2005). "Acoustic measurement of periodic noise generation in a hydrodynamical vocal fold model," In *Proceedings Forum Acusticum* (Budapest, Hungary, 2005), pg. 2731-2736.

Krebs, F., Silva, F., Sciamarella, D., and Artana, G. (2011). "A three-dimensional study of the glottal jet," Exp. Fluids 52(5):1133-1147. Doi:10.1007/s00348-011-1247-3. '

Kucinschi, B. R., Scherer, R. C., Dewitt, K. J., Ng, T. M. (2006). "An experimental analysis of the pressures and flows within a driven mechanical model of phonation," J. Acoust. Soc. Am. 119:3011-3021.

Lazar, E., DeBlauw, B., Glumac, N., Dutton, C., and Elliott, G. (2010). "A practical approach to PIV uncertainty analysis," 27th AIAA Aerodynamic Measurement Technology and Ground Testing Conference, July 2010.

Mihaescu, M., Khosla, S., Murugappan, S., and Gutmark, E. (2010). "Unsteady laryngeal airflow simulations of the intra-glottal vortical structures," J. Acoust. Soc. Am. 127:435-444.

Naegle, N. S. (2012). "Force optimization and flow field characterization from a flapping wing mechanism," Department of Mechanical Engineering, Brigham Young University, Provo, Masters Thesis, 2012.

NIDCD. (2010, June). *National Institute on Deafness and Other Communication Disorders*. Retrieved October 10, 2013, from http://www.nidcd.nih.gov/.

Oren, L., Khosla, S., Murugappan, S., King, R., and Gutmark, E. (2009). "Role of subglottal shape in turbulence reduction," Ann. Oto. Rhinol. Laryn. 118:232-240.

Pelorson, X., Hirschberg, A., Hassel, R., and Wijnands, A. (1994). "Theoretical and experimental study of quasisteady-flow separation within the glottis during phonation. Application to a modified two-mass model," J. Acoust. Soc. Am. 96:3416-3431.

Quantum Silicones (2012). Technical Data Sheet. Retrevied October 23, 2013 from http://www.quantumsilicones.com/.

Scherer, R. C., Shinwari, D., De Witt, K. J., Zhang, C., Kucinschi, B. R., and Afjeh, A. A. (2001). "Intraglottal pressure profiles for a symmetric and oblique glottis with a divergence angle of 10 degrees," J. Acoust. Soc. Am. 109:1616-1630.

Smith, S. (2011). "Influence of subglottic geometry on computational and synthetic vocal fold model vibration," Department of Mechanical Engineering, Brigham Young University, Provo, Masters Thesis, 2011.

Story, B. H. (2008). "Comparison of magnetic resonance imaging-based vocal tract area functions obtained from the same speaker in 1994 and 2002," J. Acoust. Soc. Am., 123: 327-335.

Suh, J. and Frankel, S. H. (2008). "Comparing turbulence models for flow through a rigid glottal model," J. Acoust. Soc. Am. 123:1237-1240.

Triep, M., Brucker, Ch., and Schroder, W. (2005). "High-speed PIV measurements of the flow downstream of a dynamic mechanical model of the human vocal folds," Exp. Fluids 39:232-245.

Triep, M., and Brücker, C. (2010). "Three-dimensional nature of the glottal jet," J. Acoust. Soc. Am. 127:1537-1547.

Xue, Q., Zheng, X., Mittal, R., and Bielamowicz, S. (2014). "Subject-specific computational modeling of human phonation," J. Acoust. Soc. Am. 135:1445-1456.

Zheng, X., Bielamowicz, S., Luo, H., and Mittal, R. (2009). "A computational study of the effect of false folds on glottal flow and vocal fold vibration during phonation," Ann. Biomed. Eng. 37:625-642.

APPENDIX A. PIV UNCERTAINTY – MATLAB CODE

A.1 EquipmentUncertainty.m

```
function [ wu,wv ] = EquipmentUncertainty( u,v )
%EquipmentUncertainty calculates the uncertainty due to the PIV equipment
%at each point in a PIV velocity field.

dt = 250*10^-6;

% Calibration error
l = 12*10^-3;     % meter
wl = .5*10^-3;  % meter
L1 = 300.65;        % pixel
wL1 = 1;         % pixel
L2 = 139.19;        % pixel
wL2 = .69595;     % pixel

% Timing error
t1 = 250*10^-6;    % second
wt1 = 1*10^-9;  % second
t2 = 250*10^-6;    % second
wt2 = 50*10^-9; % Second

% Calculate the rquipment uncertainty at each point in the flow field
for i = 1:length(u(:,1))
    for j = 1:length(u(1,:))
        wu(i,j) = sqrt( (u(i,j)*95.3676*1000)^2*((wl/L1)^2+(-l*wL1/L1^2)^2...
            + (-l*wL2/L1^2)^2) + (-u(i,j)*l/(dt*L1))^2*(wt1^2+wt2^2))/32;
        wv(i,j) = sqrt( (v(i,j)*95.3676*1000)^2*((wl/L1)^2+(-l*wL1/L1^2)^2...
            + (-l*wL2/L1^2)^2) + (-v(i,j)*l/(dt*L1))^2*(wt1^2+wt2^2))/32;
    end
end

end
```

A.2 InertialUncertainty.m

```
function [wu, wv] = InertialUncertainty(u,v)
%InertialUncertainty Calculates the slip velocity based on velocity field
%PIV measurements.
% u_f - u_p = 1/18*rho_p*d_p^2/mu_f*([delu_p/delt]x + [delu_p/delt]y)
% u represents a velocity component for the particle and fluid in
% the either the streamwise or transverse direction, and could also be the
% velocity magnitude.

% Preallocate vectors
slipU = zeros(size(u,1),size(u,2));
slipV = zeros(size(v,1),size(v,2));

% Experimental Constants
rho_p = 1110; % [kg/m^3]
d_p = 11e-6; % [m]
mu_f = 8.439e-3; % [Pa*s]
delT = 250e-6; % [s]
delX = 16/19.32/1000; % [m] spacing between interrogation windows in x
delY = 16/19.32/1000; % [m] spacing between interrogation windows in y

% Calculate the Inertial Uncertainty (slip velocity)
for i=2:size(u,1)-1
   for j=2:size(u,2)-1
      slipU(i,j) = 1/18*rho_p*d_p^2/mu_f*((u(i+1,j)-u(i-1,j))*u(i,j)/2/delX
            + (u(i,j+1)-u(i,j-1))*v(i,j)/2/delY);
      slipV(i,j) = 1/18*rho_p*d_p^2/mu_f*((v(i+1,j)-v(i-1,j))*u(i,j)/2/delX
            + (v(i,j+1)-v(i,j-1))*v(i,j)/2/delY);
   end
end

% Convert back to m/s
wu = slipU/32;
wv = slipV/32;

end
```

A.3 ProcessUncertainty.m

```
function [ wuProcess, wvProcess ] = ProcessUncertainty( uvel,vvel )
% ProcessUncertainty.m calculates the process uncertainty at each point
% in a PIV velocity field.

% Calculate rms value of neighbors for all points
wuProcess = zeros(172,130);
wvProcess = zeros(172,130);

for i = 2:171
    for j = 2:129
        u_rms(i,j) = sqrt((uvel(i+1,j+1)^2 + uvel(i+1,j)^2 + uvel(i+1,j-1)^2
            + uvel(i,j+1)^2 + uvel(i,j-1)^2 + uvel(i-1,j+1)^2 + uvel(i-1,j)^2
            + uvel(i-1,j+1)^2)/8);
        u_ave(i,j) = (uvel(i+1,j+1) + uvel(i+1,j) + uvel(i+1,j-1) +
            uvel(i,j+1) + uvel(i,j-1) + uvel(i-1,j+1) + uvel(i-1,j) + uvel(i-
            1,j+1))/8;
        v_rms(i,j) = sqrt((vvel(i+1,j+1)^2 + vvel(i+1,j)^2 + vvel(i+1,j-1)^2
            + vvel(i,j+1)^2 + vvel(i,j-1)^2 + vvel(i-1,j+1)^2 + vvel(i-1,j)^2
            + vvel(i-1,j+1)^2)/8);
        v_ave(i,j) = (vvel(i+1,j+1) + vvel(i+1,j) + vvel(i+1,j-1) +
            vvel(i,j+1) + vvel(i,j-1) + vvel(i-1,j+1) + vvel(i-1,j) + vvel(i-
            1,j+1))/8;

        wuProcess(i,j) = abs(u_ave(i,j) - 2*u_rms(i,j))/100;
        wvProcess(i,j) = abs(v_ave(i,j) - 2*v_rms(i,j))/100;
    end
end

end
```

A.4 TotalUncertainty.m

```
clc;
clear all;
close all;

% TotalUncertainty.m calculates the total PIV uncertainty at each point
% in a PIV velocity field.

% % Read in .VC7 files and save as .mat files for easier loading

% % Add the file path to the DaVis functions
% addpath 'C:\Program Files\MATLAB\R2011b\toolbox\matlab\lavision\';
%
% % This is the file path minus the foler
% path = 'C:\Documents and Settings\vfmrg\My Documents\Jayrin
Seegmiller\Avg_V\';
% folder='RS\RSP\P3\B';
% file_end = '_Avg V.VC7';

% for i = 1:12
%     % Read in velocity files
%     A(i) = readimx([path folder num2str(i) file_end]);
%
%     % Extract velocity
%     [xpixel, ypixel, uvel(:,:,i), vvel(:,:,i)] = showimx(A(i));
% end


% % Once the files are saved as .mat files, use the following code:

load IS_P2.mat % To process other cases and planes load the corresponding
                  .mat file.

% Here we are processing 12 phases, 0° to 216°
for i = 1:12

    % Get the process uncertainty
    [wuProcess(:,:,i), wvProcess(:,:,i)] =
      ProcessUncertainty(uvel(:,:,i),vvel(:,:,i));

    % Get the equipment uncertainty
    [wuEquip(:,:,i), wvEquip(:,:,i)] =
      EquipmentUncertainty(uvel(:,:,i),vvel(:,:,i));
```

```
    % Get the intertial uncertainty
    [wuInertial(:,:,i), wvInertial(:,:,i)] =
      InertialUncertainty(uvel(:,:,i),vvel(:,:,i));

    % Combine into absolute uncertainties
    wEquip(:,:,i) = sqrt(wuEquip(:,:,i).^2 + wvEquip(:,:,i).^2);
    wInertial(:,:,i) = sqrt(wuInertial(:,:,i).^2 + wvInertial(:,:,i).^2);
    wProcess(:,:,i) = sqrt(wuProcess(:,:,i).^2 + wvProcess(:,:,i).^2);

    % Calculate the max uncertainty for each uncertainty type
    JEquip(i) = max(max(wEquip(:,:,i)));
    JInertial(i) = max(max(wInertial(:,:,i)));
    JProcess(i) = max(max(wProcess(:,:,i)));

    % Get the total uncertainty in each direction
    TotalUncert(:,:,i) = sqrt(wEquip(:,:,i).^2 + wInertial(:,:,i).^2 +
      wProcess(:,:,i).^2);

    % Calculate the max uncertainty for the Total Uncertainty
    JTotal(i) = max(max(TotalUncert(:,:,i)));

    % Calculate absolute velocity
    vel(:,:,i) = sqrt(uvel(:,:,i).^2 + vvel(:,:,i).^2);

    % Calculate max velocity for each phase
    vmax(i) = max(max(vel(:,:,i)));

    % Plot velocity and total unertainty
    figure
    pcolor(xpixel,ypixel,vel(:,:,i))
    xlabel('X Location (mm)','fontsize',12)
    ylabel('Y Location (mm)','fontsize',12)
    shading interp
    axis equal
    h = colorbar('location','EastOutside');
    xlabel(h,'Veocity (m/s)','fontsize',12);

    figure
    pcolor(xpixel,ypixel,TotalUncert(:,:,i))
    xlabel('X Location (mm)','fontsize',12)
    ylabel('Y Location (mm)','fontsize',12)
    shading interp
    axis equal
    h = colorbar('location','EastOutside');
    ylabel(h,'Total Uncertainty (m/s)','fontsize',12);
end
```

APPENDIX B. PIV UNCERTAINTY ANALYSIS

Velocity uncertainty was determined by the ability of the equipment to accurately measure particle movement, the degree to which the particles follow the motion of the flow, and the accuracy with which the software correlates particle groupings. PIV uncertainty was calculated according to the method set forth by Lazar et al. (2010) and performed by Naegle (2012). The MATLAB code used to calculate the uncertainty at each position of the flow field is given in Appendix A.

B.1 Equipment Uncertainty

The error due to equipment uncertainty was estimated by (Lazar et al., 2010):

$$w_u = \sqrt{u^2\left[\left(\frac{1}{L}w_l\right)^2 + \left(\frac{-l}{L^2}w_{L1}\right)^2 + \left(\frac{-l}{L^2}w_{L2}\right)^2\right] + \left(\frac{-u}{\Delta t}\frac{l}{L}\right)^2 [w_{t1} + w_{t2}]}, \quad \text{(B.1)}$$

where u was the velocity, l was the length of the calibration scale for each case and plane, L was the length (in pixels) of the calibration scale on the image, w_l was the uncertainty of the calibration scale length measurement, w_{L1} was the uncertainty of the image plane length, w_{L2} was the image distortion due to lens aberrations, Δt was the time step of the image pair, w_{t1} was the uncertainty of the laser pulse timing, and w_{t2} was the accuracy of the delay generator. The parameters for equipment uncertainty are summarized in Tables B-1 and B-2.

Table B-1. Summary of equipment uncertainty parameters.

Parameter	Value	Description
l	See Table B-2	Length of the calibration scale
L	See Table B-2	Length (in pixels) of the calibration scale on the image
w_{L1}	1 pixel	Uncertainty of the image plane length
w_{L2}	0.696 pixel	Image distortion due to lens aberrations
Δt	250 μs	Time step of the image pair
w_{t1}	1 ns	Laser pulse timing uncertainty
w_{t2}	50 ns	Delay generator accuracy

Table B-2. Length of calibration scale parameters.

	Plane	Cylindrical Geometry		Realistic Geometry	
		l (mm)	L (pixel)	l (mm)	L (pixel)
Coronal	1	6	139.19	30.63	699.28
	2	6	145.80	22.89	505.98
	3	3	68.48	19.81	396.66
Sagittal	1	12	291.61	12	278.30
	2	12	300.65	12	271.77
	3	12	305.22	12	271.77

B.2 Inertial Uncertainty

Uncertainty due to inertial effects determines how well the seeding particles followed the flow. Inertial uncertainty is also known as the slip velocity, and was calculated as follows (Lazar et al., 2010):

$$u_{slip} = \frac{1}{18}\frac{\rho_p d_p^2}{\mu_f}\left(a_{px}u_{px} + a_{py}u_{py}\right), \tag{4.2}$$

where u_{slip} was the difference between the fluid and particle velocities, ρ_p was the particle density (1110 kg/m^3), d_p was the average particle diameter (11 μm), μ_f was the fluid viscosity (0.008493 Pa·s), a_{px} and a_{py} were the accelerations of the particle in the *x*- and *y*-directions, and u_{px} and u_{py} were the particle velocities in the *x*- and *y*-directions.

B.3 Process Uncertainty

Process uncertainty refers to the accuracy with which the software correlates particle groupings. Process uncertainty was estimated by calculating the error that would occur if the correlation procedure was unable to match the particle groupings. With a final window size of 16×16, the correlation can be off up to 16 pixels. However, post-processing algorithms removed vectors if its difference to the average of the neighboring vectors was more than twice the root-mean-square value of its neighbors, thus reducing the effects of poor correlation. This post-processing method caused the process uncertainty to scale with the velocity gradients in the fluid rather than the local velocity in the fluid. The process uncertainty for each point in the flow field was calculated as follows:

$$w_p = \sqrt{\left(u_x - 2u_{x(rms)}\right)^2 + \left(u_y - 2u_{y(rms)}\right)^2}, \tag{4.3}$$

B.4 Total Uncertainty

The total uncertainty for each location in the velocity measurements was calculated by combining the individual sources of uncertainty as follows (Lazar et al., 2010):

$$w_{total} = \sqrt{w_u^2 + u_{slip}^2 + w_p^2}, \tag{4.4}$$

For the open phases containing the glottal jet, the regions of highest uncertainty correlated with the regions of highest velocity. For the phases not containing the glottal jet, uncertainty still mostly correlated with velocity with high uncertainty regions also occurring in regions with few seeding particles. Uncertainty values in phases not containing a jet were significantly lower than phases containing the jet. A total maximum uncertainty of ± 0.469 m/s occurred in coronal plane 3 of the cylindrical case and corresponded to 2.4 percent of the local velocity value. All other uncertainty values were lower than this value, and maximum total uncertainty values are given in Table B-3. Figure B-1 compares the PIV velocity and uncertainty data for the 54° in the sagittal midplane for all three cases.

Table B-3. Maximum total uncertainty (w_{total}) and percent uncertainty of local velocity values for each case.

		Cylindrical		Matched Flow Rate		Matched Pressure	
	Plane	w_{total} (m/s)	% Uncertainty	w_{total} (m/s)	% Uncertainty	w_{total} (m/s)	% Uncertainty
Coronal	1	0.0309	1.66	0.0177	1.14	0.0117	1.12
	2	0.0303	1.53	0.0235	1.30	0.0191	1.41
	3	0.0469	2.40	0.0165	1.14	0.0188	1.86
Sagittal	1	0.0179	1.23	0.0221	1.14	0.0166	1.13
	2	0.024	1.14	0.0182	1.18	0.0121	1.27
	3	0.0242	1.20	0.0148	1.13	0.0098	2.42

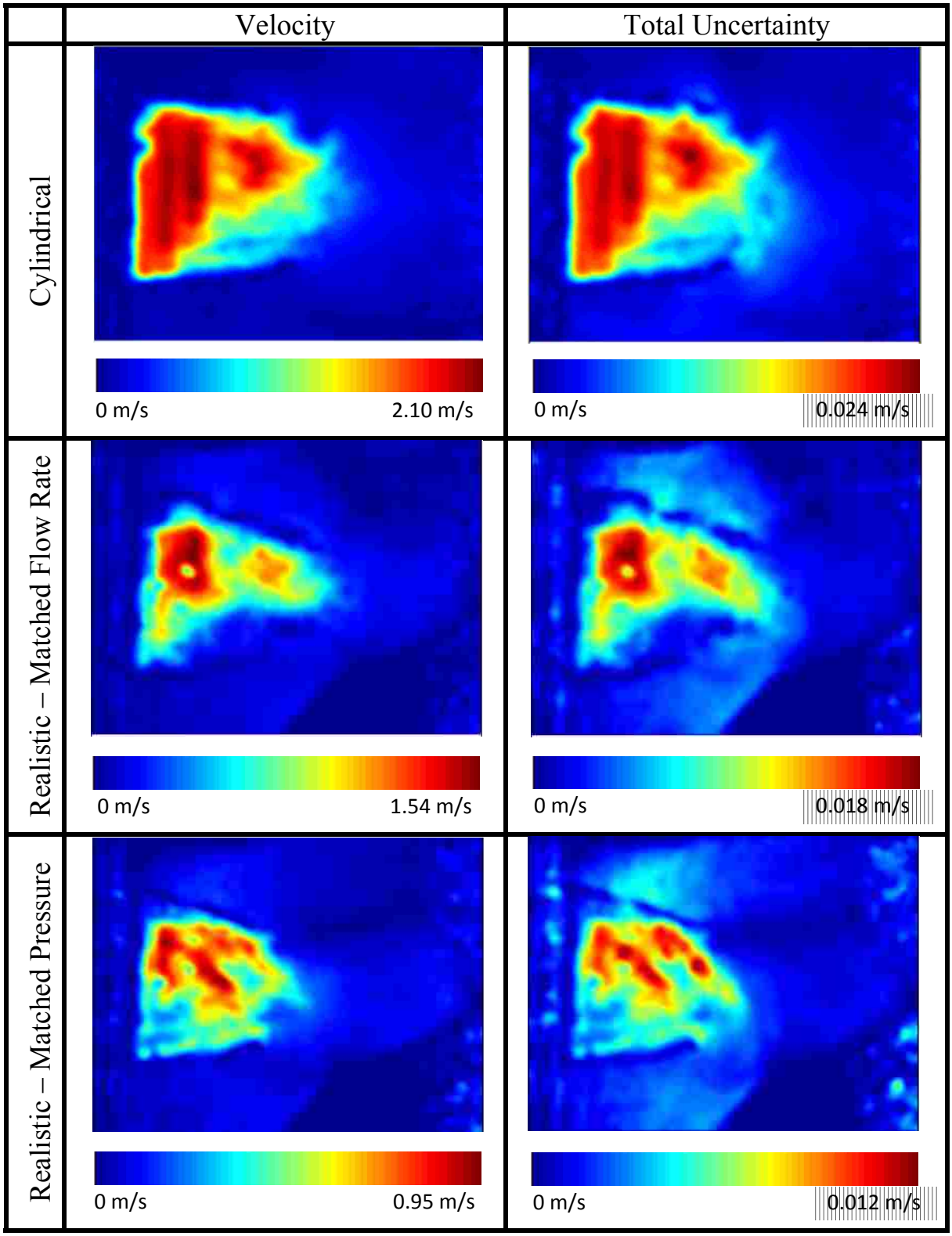

Figure B-1. Velocity and uncertainty data for 54° of the mid-sagittal plane for all three cases.

APPENDIX C. PRESSURE UNCERTAINTY

The uncertainty in the pressure data was produced from instrument uncertainty in the pressure transducer (MMDWB2.5BIV1P4C0T1A3CE, Omega Engineering, Inc.) used in this study. The instrument uncertainty was estimated by calculating the calibration error. A manometer was constructed to perform the calibration. The pressure transducer was oriented vertically, as it was during the experiment, and PVC tubes were connected to both sides. Pressure data was recorded first while the manometer was empty. Then both sides of the manometer were filled with the working fluid. The tube connected to the lower pressure port was filled with a small amount of fluid until the fluid level reached a known height. Fluid was then added to the tube connected to the upper port. Ten data points were collected with the upper port tube filled to ten different heights ranging from 6.53 cm to 63.68 cm. The measured heights were converted to pressures using the equation for hydrostatic pressure:

$$P = \rho g h \tag{B.1}$$

where ρ was the density of the glycerol-water mixture (1150.4 kg/m^3), g was the acceleration due to gravity, and h was the height of the fluid column. The collected calibration data is given in Table C-1. The percent error for each data point was plotted and a second-order polynomial was fit to the data (see Figure C-1).

Table C-1. Pressure transducer calibration data.

Measured *h* (m)	Calculated *P* (Pa)	Transducer *P* (Pa)	Difference	% Error
0.065	735.939	768.030	-32.091	-4.361
0.154	1738.190	1779.453	-41.263	-2.374
0.205	2310.906	2345.749	-34.844	-1.508
0.259	2919.415	2930.126	-10.710	-0.367
0.332	3742.693	3746.048	-3.354	-0.090
0.408	4601.766	4516.967	84.799	1.843
0.459	5174.481	5102.037	72.444	1.400
0.535	6033.554	5946.333	87.221	1.446
0.586	6606.269	6489.662	116.607	1.765
0.637	7178.984	7031.081	147.904	2.060

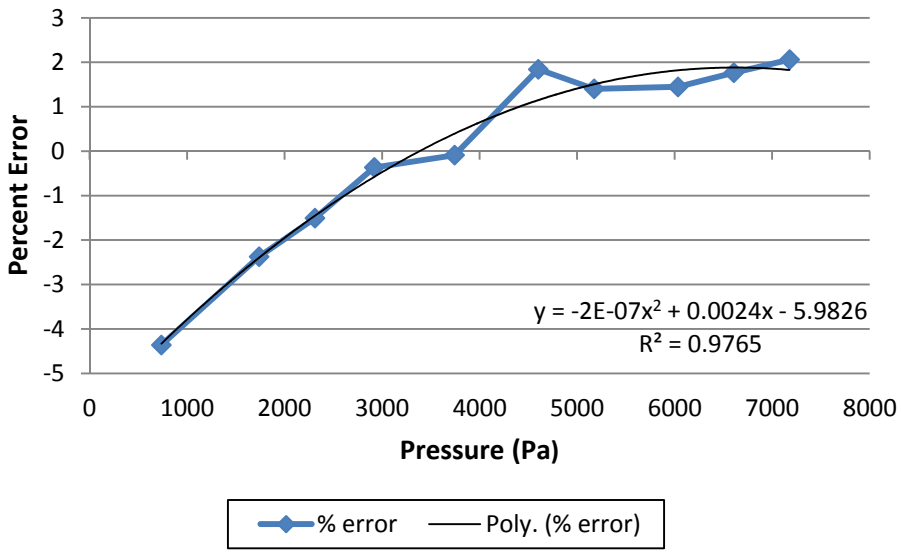

Figure C-1. Percent error of the pressure calibration data.

The calibration uncertainty, u_C, was calculated by finding the standard error of fit, S_{yx}, as follows:

$$S_{yz} = \sqrt{\frac{1}{\nu}\sum_{i=1}^{N}(y_i - y_{ci})^2} \tag{B.2}$$

$$\nu = N - (m+1) \tag{B.3}$$

$$u_C = \pm t_{\nu,95} S_{yx} \tag{B.4}$$

where y_i was the calculated percent error, y_{ci} was the curve fit prediction of the percent error, N was the number of data points, m was the order of the curve fit, and $t_{\nu,95}$ was the t estimator (2.365).

The total instrument uncertainty was a combination of the calibration uncertainty and the uncertainty in the pressure calculated from the fluid heights. The pressure uncertainty was calculated using a root sum of squares:

$$u_P \approx \pm\sqrt{\left(\frac{\partial P}{\partial \rho}u_\rho\right)^2 + \left(\frac{\partial P}{\partial h}u_h\right)^2 + \left(\frac{\partial P}{\partial g}u_g\right)^2} \tag{B.5}$$

$$\frac{\partial P}{\partial \rho} = gh, \frac{\partial P}{\partial h} = \rho g, \frac{\partial P}{\partial g} = \rho h \tag{B.6}$$

$$u_\rho = \pm\ 0.7 \text{ Pa}, u_h = \pm\ 6.35 \text{ cm}, u_g = negligible \tag{B.7}$$

$$u_I = \pm\sqrt{(u_P)^2 + (u_C)^2} \tag{B.8}$$

Figure C-2 shows the total instrument uncertainty derived from the calibration. It was found that the instrument uncertainty was highest in the lowest pressure range (9.85% for P = 735.94 Pa), and then decreased as the pressure increased. This corresponds to the instrument

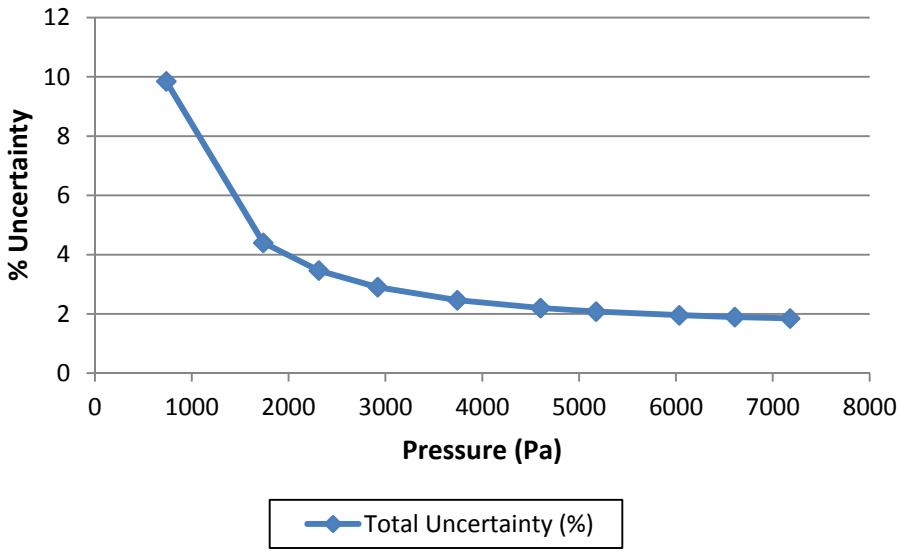

Figure C-2. Total instrument uncertainty for the pressure calibration range.

error decreases as the pressures approach the middle of the range of the pressure transducer (0-17200 Pa).

The calibration was applied to the acquired pressure data. For pressures below the calibration range the curve fit of the percent error between the calculated and the measured (transducer) pressures was extrapolated and the calibration was applied. This caused the calibrated pressures to deviate more from the original pressure data near the pressure minimum. For pressures above the calibration range (this applied only to the matched flow rate case), the average of the percent error of the last five calibration points was used. Figures C-3, C-4, and C-5 compare the pressure data for each case before and after calibration.

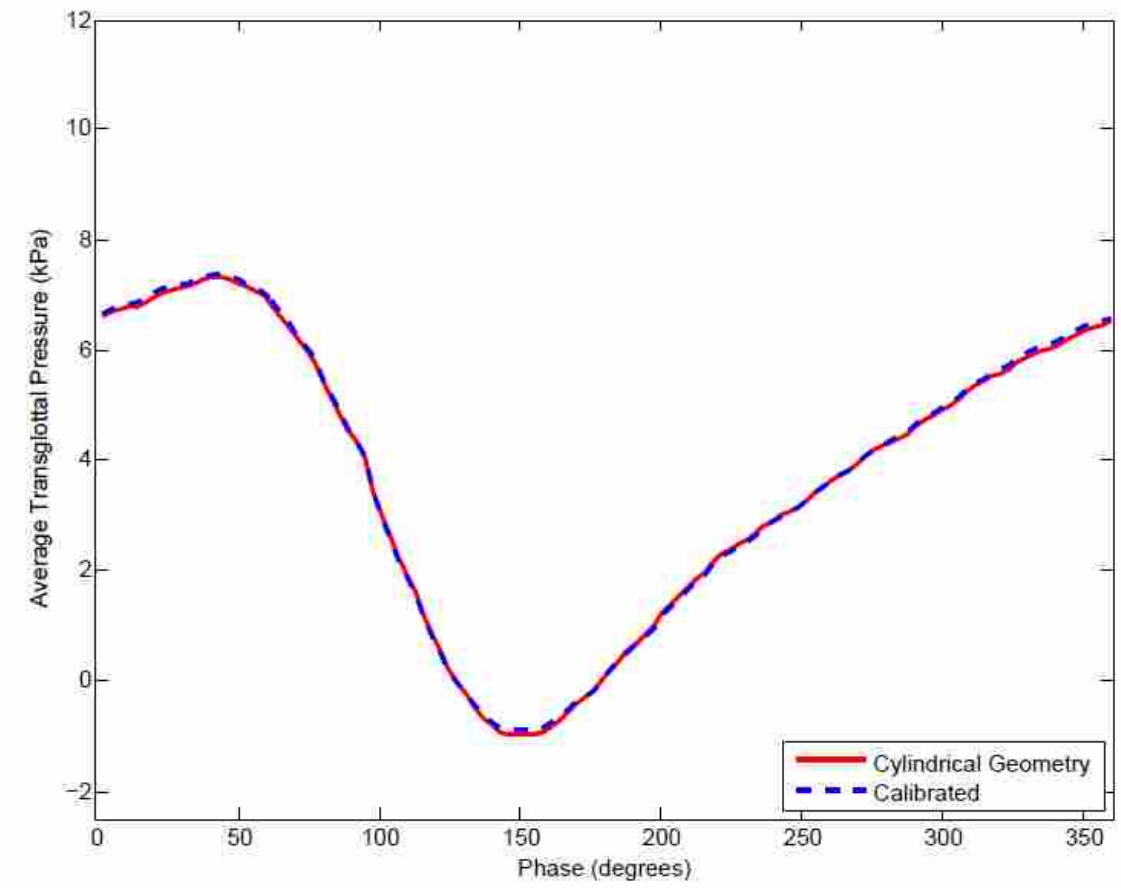

Figure C-3. Comparison of original and calibrated pressure data for the cylindrical case.

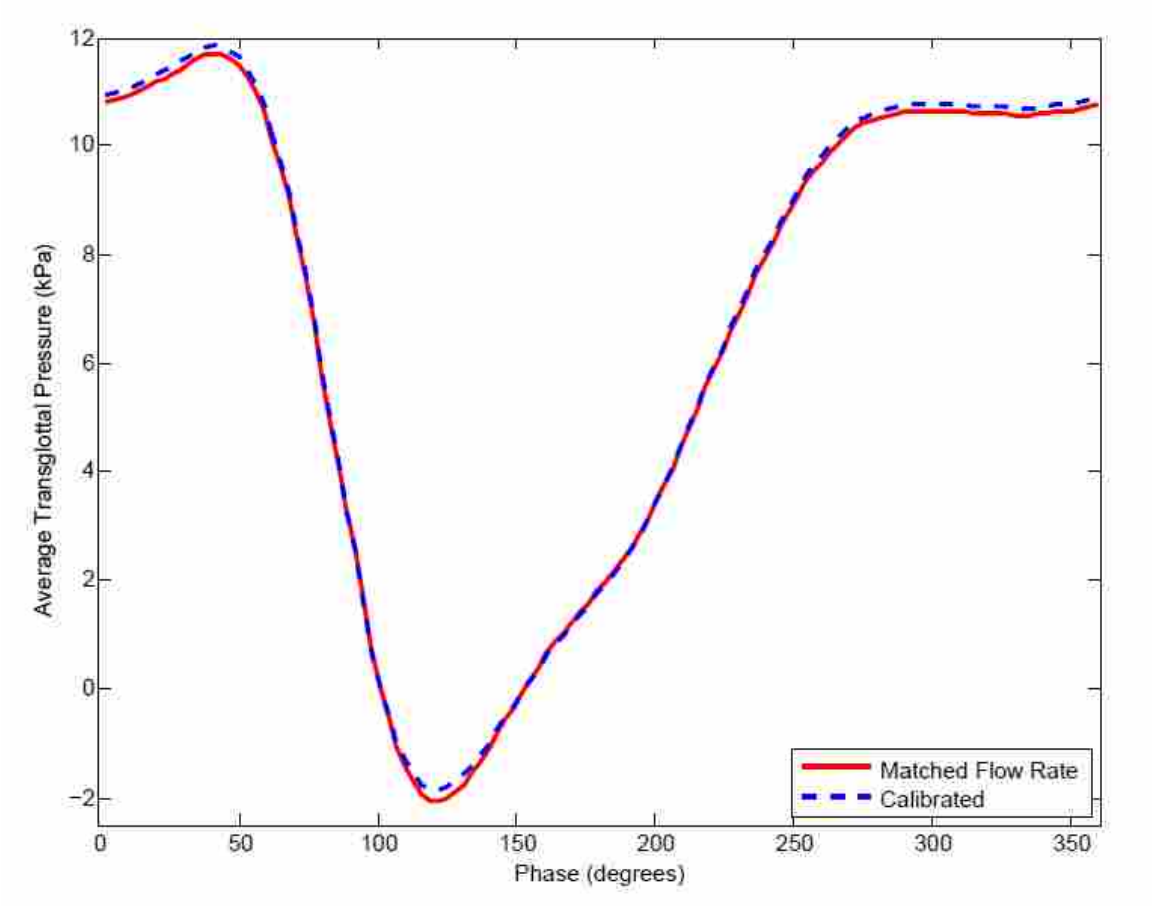

Figure C-4. Comparison of original and calibrated pressure data for the matched flow rate case.

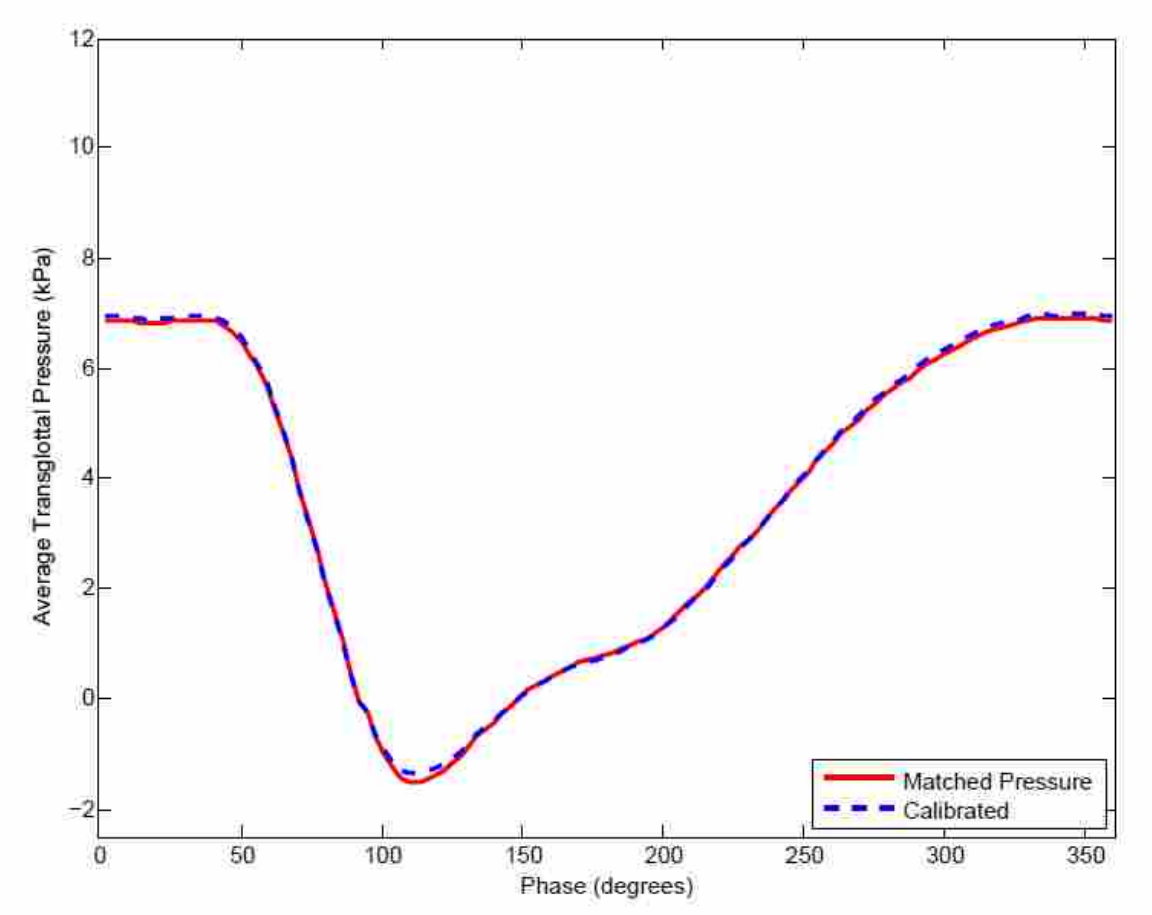

Figure C-5. Comparison of original and calibrated pressure data for the matched pressure case.